THESIS FOR THE DEGREE OF DOCTOR OF PHILOSOPHY

Metallic materials for solid oxide fuel cells and electrolysers

Mitigating high temperature corrosion

MAREDDY JAYANTH REDDY

Department of Chemistry and Chemical Engineering
CHALMERS UNIVERSITY OF TECHNOLOGY

Gothenburg, Sweden 2023

Metallic materials for solid oxide fuel cells and electrolysers
Mitigating high temperature corrosion
MAREDDY JAYANTH REDDY
ISBN 978-91-7905-832-6

Doktorsavhandlingar vid Chalmers tekniska högskola
Ny serie nr. 5298
ISSN 0346-718X

Department of Chemistry and Chemical Engineering
Division of Energy and Materials
Chalmers University of Technology
SE-412 96 Gothenburg
Sweden
Telephone: +46 (0)31-772 1000

Cover:
SEM micrographs in the cross-section of the uncoated and Ce/Co coated AISI 409, AISI 441 and Crofer 22 APU exposed to 800°C.

Chalmers digitaltryck
Gothenburg, Sweden 2023

Metallic materials for solid oxide fuel cells and electrolysers

MAREDDY JAYANTH REDDY
Department of Chemistry and Chemical Engineering
Chalmers University of Technology

Abstract

Solid oxide cells (SOCs) are high-temperature energy conversion devices that have great potential due to their high efficiency, low operating costs, and flexibility. SOCs can produce electricity from a variety of fuels as solid oxide fuel cells (SOFCs), and they can convert electricity to fuels as solid oxide electrolyser cells (SOECs). However, the wide-spread commercialisation of this technology is hindered by high system cost, lack of durability, and poor performance stability during long-term operation. Owing to the high-temperature operation and aggressive environment of SOCs, metallic materials used for interconnects and balance of plant (BOP) components are subject to corrosion. Interconnects are typically made of ferritic stainless steel (FSS), which forms a protective chromia scale at high temperatures. The degradation mechanisms, such as Cr (VI) evaporation and chromia scale growth, lead to electrode poisoning and increased electrical resistance, which degrade cell performance.

The primary objective of this thesis is to develop alternative materials and understand the degradative mechanisms so as to effectively reduce the costs and improve the performances of metallic materials in SOC systems. The Cr evaporation, oxide scale growth, the microstructural evolution of the oxide scale, and the area-specific resistances are investigated for the selected materials. The majority of the thesis is focused on Ce/Co coatings. Ce/Co-coated, low-cost, commercial FSS (AISI 441, AISI 430, and AISI 444) are compared to tailor-made Crofer 22 APU in air-side atmospheres. Ce/Co-coated steels are further investigated under dual-atmosphere conditions. The Ce/Co coating is compared to various coatings from research laboratories and universities world-wide. Furthermore, the underlying causes for the improvement in the oxidation resistances of FSS that occur in the presence of the reactive element Ce (in the Ce/Co coating) are investigated, and a new mechanism is proposed. Finally, a model to predict the lifetimes of the coated steels is proposed. Moreover, a new coating system, the Ce/FeNi coating, is proposed as an alternative to the Ce/Co coating. The Ce/FeNi coating is found to be more effective than Ce/Co coating in reducing chromia scale growth.

While research on metallic materials for SOC has centred on the interconnects, the metallic materials used in BOP components, which can be a significant source of volatile chromium species, have been largely neglected. Five metallic materials (AISI 441, AISI 444, A197/Kanthal® EF101, alloy 800H, and alloy 600) are examined for potential usage in BOP components. The oxidation and Cr evaporation behaviours of these materials are discussed and correlated to the observed microstructures.

Keywords: SOFC, Interconnect, Balance of Plant, High-temperature corrosion, Chromium evaporation, MCO coating, PVD

List of publications

This thesis is based on the work contained in the following papers:

Paper I Reddy, M. J., Svensson, J. E. and Froitzheim, J. "Reevaluating the Cr Evaporation Characteristics of Ce/Co Coatings for Interconnect Applications" *ECS Transactions.* **103**, 1899–1905 (2021)

Paper II Reddy, M. J., Chausson, T., Svensson, J. E. and Froitzheim, J. "11-23% Cr steels for solid oxide fuel cell interconnect applications at 800 °C – How the coating determines oxidation kinetics", *International Journal of Hydrogen Energy* **48** (34) (2023)

Paper III Reddy, M. J., Visibile, A., Svensson, J. E. and Froitzheim, J. "Investigation of coated FeCr steels for application as solid oxide fuel cell interconnects under dual-atmosphere conditions", *International Journal of Hydrogen Energy* **In Press, Corrected Proof** (2023)

Paper IV Reddy, M. J., Kamecki, B., Talic, B., Zanchi, E., Smeacetto, F., Hardy, J. S., Choi, J. P., Mazur, Ł., Vaßen, R., Basu, S. N., Brylewski, T., Svensson, J.-E., and Froitzheim, J. "Experimental review on the performances of protective coatings for interconnects in solid oxide fuel cells", *Journal of Power Sources* **568** (2023)

Paper V Reddy, M. J., Krogsgaard T., Froitzheim, J. and Svensson, J. E. "Re-visiting the behaviour of reactive elements in the Ce/Co coatings of ferritic stainless steels", *Manuscript*

Paper VI Reddy, M. J., Goebel, C., Valot, A., Svensson, J. E., Frandsen, H. L., and Froitzheim, J. "Comparison of $(Mn, Co)_3O_4$ vs $(Fe, Ni)_3O_4$ spinel coatings for stainless steel interconnects in solid oxide electrolysis", *Manuscript*

Paper VII Reddy, M. J., Svensson, J. E. and Froitzheim, J. "Evaluating candidate materials for balance of plant components in SOFC: Oxidation and Cr evaporation properties" in *Corrosion Science* **190** (2021)

Statement of author's contribution

I am the main author of all the appended papers. I performed most of the experimental planning, work and writing for all the papers. A more-detailed description of my contributions to the articles is given below.

For **Paper II**, Thibaut Chausson assisted with the chromium evaporation and oxidation studies for some of the materials within the scope of an internship under my supervision. For **Paper III**, Alberto Visibile helped me with the dual-atmosphere exposures. For **Paper IV**, several co-authors from different universities/labs provided the samples for the investigation. For **Paper V**, Throbjörn Krogsgaard conducted a part of the experimental

work within the scope of a master's degree thesis under my supervision. For **Paper VI**, Anabelle Valot helped me with the chromium evaporation and oxidation studies for some of the materials within the scope of an internship under my supervision. Claudia Goebel undertook a part of the experimental work at The Technical University of Denmark and wrote certain sections of the paper. For **Paper VII**, I did most of the experimental work. Florian Le Briquer performed the exposures for Alloys 800H and A197, within the scope of an internship under my supervision.

Acknowledgements

Throughout the work leading to this thesis, I have received much support and help. I want to take this opportunity to acknowledge everyone.

First of all, I would like to express my sincere gratitude to my supervisors, Prof. Jan Froitzheim and Prof. Jan-Erik Svensson, for giving me the opportunity to carry out my PhD studies in the SOFC group at Chalmers. Thank you for your expert guidance, helpful advice, and constant encouragement throughout my research journey. Their invaluable expertise helped me formulate the research topic and approach, and their constructive feedback along the way was extremely helpful.

Furthermore, I would also like to thank my examiner, Prof. Lars-Gunnar Johansson, and director of studies, Prof. Itai Panas, Lars Evenäs for their support, insightful discussions during my research. I am grateful to them for providing an open space for communication.

Countless people have been tremendously engaging, patient and friendly, contributing to a supportive working environment. I would like to thank my colleagues (current and former) in the Fuel Cell Group (FCG): Alberto Visibile, Matthieu Tomas, Claudia Göbel, Luca Gagliani, Camilla Cossu, Kereem Ozgur Gunduz, Anton Chyrkin and Hannes Falk-Windisch. Thank you for creating a safe and friendly work environment and for initiating many intriguing discussions and collaborations. My heartfelt gratitude goes to Esraa Hamdy, Christine Geers, Lolli and Tommy Sand for their valuable inputs and for helping me with my experiments. Special thanks go to my interns and master thesis students, Florian Le Briquer, Thibaut Chausson, Thorbjørn Krogsgaard, Isak Almyren, Anabelle Valot, and Hlib Kavatsiuk for taking part in my work and assisting in the production of valuable results.

I would like to express my gratitude to everyone at the High Temperature Corrosion Centre (HTC) and the Energy and Materials Division for their help, support, and for making me feel welcome. Special thanks to our administrators, Sandra and Christina, for their assistance with administrative tasks. I am also grateful to HTC, Fuel Cells and Hydrogen 2 Joint Undertaking, and Metalliska Material for their financial support. This work was partly carried out at the Chalmers Materials Analysis Laboratory, CMAL. I would also like to acknowledge our industrial partners, Alleima, Sunfire, Outokumpu, Aperam, and Ceres power, for providing us with interesting research questions and engaging discussions. A big thank you to Mikael Stenström for supporting my requests for various coatings.

Finally, a heartfelt thanks to my family, mom, dad, sister and grandparents for their unwavering love, support and encouragement. Lastly but most importantly, I thank my wife Sheetal, who has been my constant companion and source of strength throughout my journey. Her love, support, and encouragement have been invaluable to me. I am grateful for her unwavering belief in me and for always being there to cheer me on, no matter how difficult the journey has been.

to my grandfather

Contents

List of Acronyms

ASR	–	Area Specific Resistance
APS	–	Atmospheric Plasma Spraying
BIB	–	Broad ion beam
BOP	–	Balance of Plant
BSE	–	Back-scattered Electron
CGO	–	Gadolinia Doped Ceria
CHP	–	combined Heat and Power
EPD	–	Electrophoretic Deposition
EDX	–	Energy Dispersive X-ray Spectroscopy
EU	–	Europen Union
FSS	–	Ferritic Stainless Steel
MCO	–	Manganese Cobalt oxide
MCF	–	Manganese Cobalt Iron oxide
PEMFC	–	Proton-exchange membrane fuel cell
PVD	–	Physical Vapor Deposition
RE	–	Reactive Element
REE	–	Reactive Element Effect
SE	–	Secondary Electron
SEM	–	Scanning Electron Microscopy
SOC	–	Solid Oxide Cell
SOEC	–	Solid Oxide Electrolysis Cell
SOFC	–	Solid Oxide Fuel Cell
TEC	–	Thermal Expansion Coefficient
XRD	–	X-ray Diffraction

1 Introduction

1.1 Background

Global warming represents a serious threat to our planet and its people. It has the potential to significantly impact our environment, economy, and society. In the 2020s, the effects of climate change have become even more apparent, culminating in a climate emergency. The concentrations of greenhouse gases in the atmosphere are setting new yearly records, with levels now at their highest ever in human history [1]. This is leading to an increased frequency and intensity of extreme weather events. Heat waves are widespread, leading to the destruction of millions of hectares of forest. At the same time, the intensity of tropical storms has increased, leading to the destruction of ecosystems and damage to infrastructure. An immediate course correction is required to avoid reaching the climate tipping point, which is the point of no return where changes in the climate system become self-perpetuating and have serious implications for humanity [2].

The use of non-renewable fossil fuels such as coal, oil, and gas as primary energy sources is the major contributor to climate change. Global fossil CO_2 emissions, including cement carbonation, exceeded 35 Gt-CO_2 in 2022 [3]. While reducing these emissions is crucial, there is a growing demand for energy due to population growth and rising living standards. The emergence of new technologies and consumer trends has also contributed to the increased demand. Sustainable primary energy sources that do not emit carbon and that can be scaled rapidly are essential to avoid a climate catastrophe. Thus, renewable energy sources such as wind and solar are being developed at a rapid pace. Since 2010, the primary energy provided by wind and solar power has increased seven-fold [4]. Investing in renewable sources has further helped to stimulate the economy, providing jobs while creating long-term economic growth. However, the intermittency of energy production from wind and solar sources presents a significant challenge. Energy consumption patterns differ significantly based on factors such as time, geography, and weather. Long-term energy storage solutions are essential to meet peak-hour demands and during low production periods to ensure wide-scale deployment of renewable energy sources in the transition towards decarbonised energy systems. Energy storage can bridge the intermittency of renewable sources, enabling grid stability and a reliable power supply. Although batteries are highly efficient for energy storage, they are only effective and economical in the short term, to meet peak demands and grid balancing [5].

One promising long-term energy storage form is chemical storage, whereby energy generated using renewable sources can be transformed into chemical energy and then stored. For example, electricity generated by wind and solar sources can be used to produce hydrogen via electrolysis, which can then be stored and converted back to electricity when required. Hydrogen is a versatile energy carrier that can be used to decarbonise hard-to-abate sectors, such as steel, cement, and building material production plants, which are responsible for 30% of annual CO_2 emissions [6]. In addition, it can

be used as a feedstock for renewable chemicals, fertiliser production, and as fuel for the transportation sector.

More than 99% of the hydrogen produced today originates from fossil fuels and is primarily used for petroleum refining, and chemical and fertiliser production [7]. Fuel cells and electrolysers are considered promising technologies for enabling a hydrogen ecosystem, which is regarded as a major component of the solution to climate change. Fuel cells are electrochemical devices that convert the chemical energy of a fuel directly into electricity. They are highly efficient, reliable for use with low emissions, and silent in operation, making them attractive for distributed power generation, transportation, and backup power. Electrolysers work in the opposite way to fuel cells, using electricity to split water to generate a fuel (e.g. H_2) and oxygen. Green hydrogen produced by electrolysers is the critical element for decarbonisation and will significantly impact numerous industries. The possibilities to combine hydrogen with renewables are shown in Figure 1.1.

Different types of fuel cells are available, each with their advantages and disadvantages. The most widely used fuel cell is the Proton-exchange membrane fuel cell (PEMFC). These fuel cells use hydrogen as fuel and operate at temperatures in the range of 80°C-130°C, making them ideal for applications in the automotive sector, backup power systems, and stationary power generation. The major drawbacks are a lack of fuel flexibility, sensitivity to impurities in the fuel, and the requirement for expensive Pt catalysts to enhance the reaction rates [8]. In contrast, Solid Oxide Fuel Cell (SOFC)s operates on the same principle but at much higher temperatures (600°-900°C). Thus, SOFCs do not require a catalyst and have higher fuel flexibility. Therefore, they can operate with hydrocarbons, use the existing infrastructure, and support a smoother transition from fossil-based to renewable energy systems. System efficiencies as high as 90% can be achieved using SOFC-based Combined Heat and Power (CHP) systems [9], making them ideally suitable for distributed power generation. SOFCs can be operated in reverse mode, to generate fuel from electricity as Solid Oxide Electrolysis Cell (SOEC). Furthermore, waste heat can be utilised to lower the electrical input in SOEC, thereby reducing the cost of hydrogen production. However, SOFC/SOECs have longer start-up times. Moreover, the high operating temperatures result in higher material costs and faster degradation, which are significant obstacles to the widespread commercialisation of the Solid Oxide Cell (SOC) technology. The present work addresses the challenges of using metallic materials in SOC system, which contributes significantly to their costs and lifetime.

In SOCs, metallic materials are mainly used in the interconnects and Balance of Plant (BOP) components. Interconnects connect electrically the individual cells to form a fuel cell stack. Ceramic interconnects have been replaced with metallic ones to reduce costs and improve performance. Ferritic Stainless Steel (FSS) is used because they represent a compromise between cost and the required material properties. Nevertheless, the contribution of the interconnect to the overall stack cost remains significant [10, 11]. At the high operating temperatures of SOCs (600°-900°C), FSS undergo high-temperature oxidation, which increases the electrical resistance across the cell. Moreover, the chromia scale reacts with the SOFC cathode atmosphere to form volatile Cr species, which poison

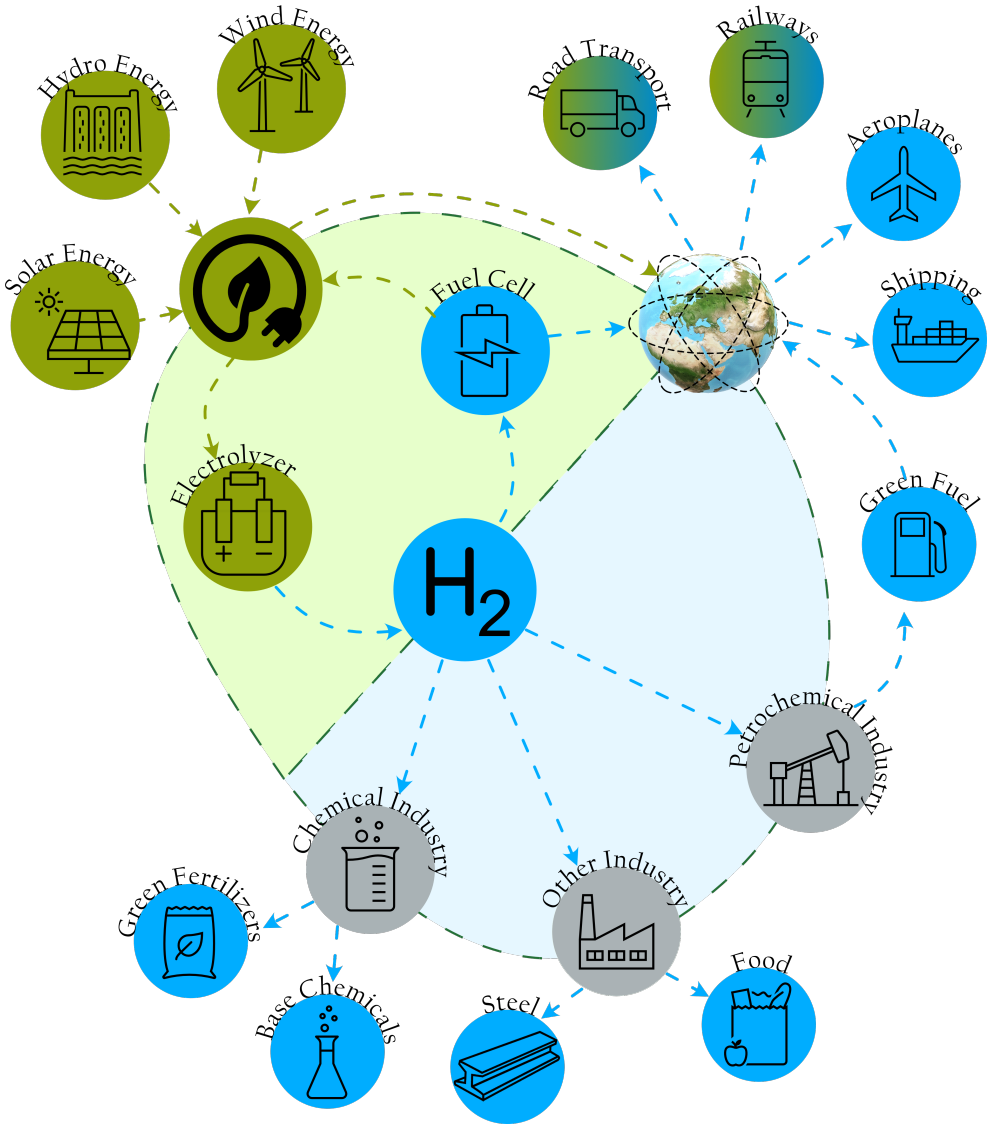

Figure 1.1: Possibilities for integrating hydrogen with renewable energy systems for a low-carbon future.

the cathode and degrade cell performance. To overcome these issues, tailor-made alloys have been developed for interconnect applications. However, these alloys are expensive and increase the overall cost of the system. One way to mitigate corrosion on the FSS is to apply protective coatings. From the economic point-of-view, combining low-cost steel with a protective coating is a promising approach. Therefore, it is essential to investigate the performances of low-cost steels and compare them with tailor-made alloys.

In addition to interconnects, metallic materials are also used in other parts of the SOC system that are exposed to high temperatures. The BOP components, comprising of a cathode preheater, a heat recuperating system, tubing, a fuel processor, and assembly components, are auxiliary components that support the functioning of an SOC system. Metallic materials used outside the fuel cell stack can be a source of volatile Cr (VI) species. Owing to their complex geometries, using coatings to prevent Cr evaporation on interconnects is challenging to implement for BOP components. Since the BOP components can account for up to 75% of the total system cost [11], it is vital to find suitable, cost-effective materials for use in the BOP.

1.2 Aim of the thesis

The commercialisation of SOC systems has been limited by critical factors, such as material costs and service lifetime. Although cheaper materials are required to lower the costs, they must perform similarly or better than the state-of-the-art materials. The aim of this thesis is to address the degradation mechanisms in metallic materials used in solid oxide fuel cells. The research is focused on improving the understanding of the mechanisms behind the high-temperature degradation of the interconnect and BOP materials. This has led to the development of effective mitigation strategies and the identification of low-cost alternative materials.

1.2.1 Steels and coatings for the interconnects

Tailor-made steels with protective coatings are the current state-of-the-art materials for interconnects. Protective coatings are essential to reduce Cr evaporation and reduce the growth of the chromia scale, thereby improving the performance of the SOC stack. The effectiveness of Ce/Co coatings in mitigating Cr evaporation under SOFC conditions is investigated in Paper I. Moreover, there is an impetus to find low-cost commercial steels that can perform as well as the tailor-made steels. Low-cost steels, such as AISI 441, AISI 444, and AISI 430, can become interesting candidates when coated. The coated low-cost steels are compared to the coated tailor-made steels and uncoated steels in terms of Cr evaporation behaviours, oxidation kinetics, and area-specific resistance in Paper II. The behaviours of both uncoated and coated steels are further studied under dual-atmosphere conditions in Paper III.

One of the main issues associated with using low-cost steels as a substitute for tailor-made steels is the low Cr reservoir. To ensure long-term operation without breakaway corrosion due to Cr depletion, low-cost steels must be thicker in order to provide the same amount of Cr. However, this goes against the market demand for smaller, lighter, and cheaper SOC systems. Laboratory or field tests cannot fully evaluate the life spans of interconnect materials because of their expected very long lifetimes. To address this problem, a model has been developed for predicting the lifetime of the coated interconnect steels.

The most common coatings proposed for interconnects are spinel oxides. These coatings are applied in several ways, such as electrophoretic deposition, PVD, atmospheric plasma spray (APS), sol-gel coating, and screen printing. The thicknesses of these coatings varies significantly, ranging from 0.6 μm to 100 μm, as do their chemical compositions. Since 2007, more than 500 research papers have been published with the keywords "interconnect" and "coating". However, rarely have different coatings been compared under similar conditions. In Paper IV, coatings developed by eight research labs and universities around the world are compared under identical conditions, to provide a baseline reference for future studies.

The oxidation resistance of high-temperature materials can be improved by reactive elements, such as Ce, La, and Y. This is commonly known as the reactive element effect (REE). Although depositing a 10 nm Ce coating substantially improves oxidation resistance, the mechanism behind this behaviour is unclear. Therefore, it is essential to understand the mechanism of the REE to develop a more fundamental and rational approach to the development and application of coatings. In Paper V, a new mechanism is proposed to explain the REE in a specific coating system.

Most of the coatings discussed in the literature were developed for interconnects in SOFCs. However, the conditions at the air electrode differ between SOFCs and SOECs. Since the water vapour content of the SOEC is very low, Cr evaporation is not a significant concern. Furthermore, most state-of-the-art coatings are based on Co, which the EU defines as a critical raw material. In Paper VI, a new Co-free coating tailored for SOEC applications is discussed.

1.2.2 Material selection for the Balance of Plant

The BOP materials do not have the same material constraints as the interconnect materials. Therefore, a wide range of materials is available for use in BOP applications. In paper VII, alloys from different material groups are selected and investigated in air. The evaluation focuses on the Cr evaporation and oxidation properties of these materials at different temperatures.

2 Fuel Cells and Electrolysers

Fuel cells and electrolysers have a long history that spans over two centuries. British scientists Sir Anthony Carlisle and William Nicholson first described water electrolysis in 1800. In 1839, Sir William Grove and Christian Friedrich Schönbein independently discovered reverse electrolysis [12]. The scientists used the 'gas battery' to prove that an electrochemical reaction between hydrogen and oxygen could produce an electric current. Another essential contribution to fuel cells came in the early 20^{th} Century from Wilhelm Ostwald, who provided much of the theoretical understanding of the fuel cell operation [13].

Fuel cells and electrolysers are electrochemical devices that convert chemical energy into electrical energy and vice versa. The basic principle behind the working of fuel cells and electrolysers is the same: split the electrochemical reaction into two half-reactions while limiting the electrical transfer of electrons, creating a potential difference. In fuel cells, the chemical reaction is spontaneous, thus producing electric current. In contrast, the chemical reaction in the electrolysers is non-spontaneous; therefore, an electric current is used to drive the reaction in the opposite direction, producing the fuel and the oxidant. Fuel cells and electrolysers have high efficiencies and have similar fundamental principles and materials.

2.1 Fuel cells

The functioning of a fuel cell is similar to that of a battery. In both cases, a chemical redox reaction is locally separated into oxidation and reduction reactions. However, the main difference is that the battery releases the stored energy, whereas the fuel cell generates energy from the fuel. The basic overall reaction for fuel cells operating with hydrogen is the hydrogen combustion reaction shown in Equation (2.1):

$$H_2 + \frac{1}{2}\,O_2 \rightarrow\ H_2O(g) + energy; \Delta G^o = -237.09\ kJmol^{-1} \tag{2.1}$$

$$Anode : H_2 + O^{2-} \rightarrow\ H_2O + 2e^- \tag{2.2}$$

$$Cathode : \frac{1}{2}\,O_2 + 2e^- \rightarrow\ O^{2-} \tag{2.3}$$

The hydrogen combustion reaction [Equation (2.1)] can be separated into two electrochemical half-reactions: oxidation [Equation (2.2)] and reduction [Equation (2.3)]. An electrolyte separates the fuel and air, and the oxidation and reduction half-reactions occur at the anode and cathode electrodes, respectively. The electrolyte facilitates the electrochemical reaction by conducting specific ions at a high rate while limiting electron transfer. Electrons are forced to flow through an external circuit that connects the electrodes to complete the reaction; this flow of electrons is harnessed as electric current.

In contrast to combustion engines, fuel cells directly convert the chemical energy in the fuel into electrical energy, eliminating the inefficient intermediate stages of the combustion process. The traditional combustion process converts chemical energy to heat, then to mechanical energy, and finally to electricity in a series of complex and inefficient steps, which limit its overall efficiency [14]. While conventional combustion power plants have an efficiency of about 30% [14], fuel cells can achieve an electrical efficiency of up to 65% [12]. Fuel cells operate silently, reducing noise pollution, and have low levels of wear and tear, so they have lower maintenance requirements and higher system reliability. In addition, they produce extremely low emissions, and particulates such as NO_x and SO_x are absent due to the absence of combustion. Despite these advantages, the fuel cell technology has had limited implementation due to its high cost, which is linked to low production volumes. Furthermore, fuel cells are susceptible to environmental poisons because of their complex electrochemical processes and interfaces.
There are five main types of fuel cells, differentiated according to the type of electrolyte or operating temperature [13]:

1. Alkaline fuel cell (AFC)
2. Polymer electrolyte membrane fuel cell (PEMFC)
3. Phosphoric acid fuel cell (PAFC)
4. Molten carbonate fuel cell (MCFC)
5. Solid-oxide fuel cell (SOFC)

Despite their differences in relation to electrolytes and mobile ions, all fuel cells operate on the same electrochemical principle. They also differ with respect to operating temperature range (from 60°-1000°C), fuel tolerance, performance characteristics, and materials used. The ionic charge carriers are: in PEMFC and PAFC, protons (H^+); in SOFC, oxygen ions (O^{2-}); in AFC, hydroxide ions (OH^-); and in MCFC, carbonate ions (CO_3^{2-}). Detailed information about the fuels, operating temperatures, and mobile ions are provided in Figure 2.1.

The most commonly used fuel cell is the PEMFC, which operates at a relatively low temperature of about 80°C. It uses CO-free H_2 as the fuel and a Pt catalyst to accelerate the electrochemical reaction [13]. In contrast, the SOFC operates at high temperatures and eliminates the need for an expensive catalyst, while producing high-quality waste heat. In addition, they can use hydrocarbons as fuel. However, the operation of SOFCs at high temperatures leads to longer start-up times compared to the PEMFC [15]. In addition, the high operating temperatures have detrimental impacts on the durability of the materials.

The SOFC uses an oxide ion-conducting ceramic electrolyte in combination with mixed conducting electrodes. To ensure the mobility of the oxygen ions, the SOFC operates at high temperatures, which allows for fuel flexibility. Figure 2.2a illustrates the working

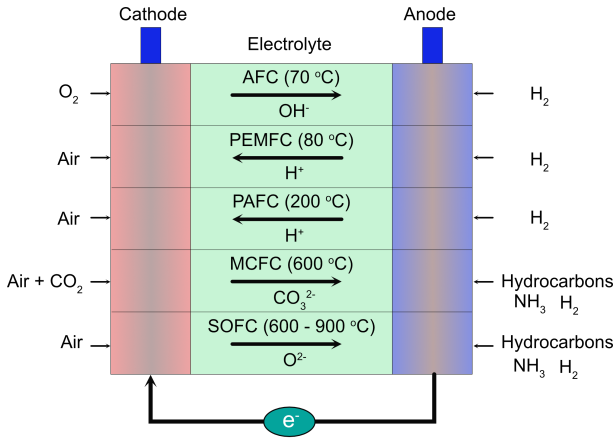

Figure 2.1: Different fuel cell families. Adapted from [13]

principle of a single SOFC cell composed of three components: an anode, a cathode, and an electrolyte. At the cathode, oxygen gas reacts to form oxide ions according to Reaction 2.3. The oxide ions migrate through the electrolyte and react with the fuel (H_2) at the anode, according to Reaction 2.2. The electrons released from the reaction at the anode flow through an external circuit.

SOFCs have high electrical efficiencies at all capacities, making them suitable for small-scale applications such as powering homes, medium-scale applications such as airports, and large-scale power generation plants. In addition, they can use hydrocarbons as fuels, leverage existing infrastructure, and facilitate a smoother transition from fossil-based to renewable energy systems. Another advantage of the SOFCs is that they can be used in reverse mode as SOEC, to produce fuel from surplus electricity.

2.2 Electrolysis Cells

Electrolysers operate in the opposite way to fuel cells, using electrical current to drive a non-spontaneous chemical reaction [17]. Similar to fuel cells, electrolysis cells consist of an electrolyte and two electrodes. An external direct current power source is connected to the two electrodes, driving a non-spontaneous chemical reaction. The basic overall reaction for electrolysis cells is the water electrolysis reaction shown in Equation (2.4). The electrical current splits the water molecule and generates hydrogen and oxygen at the cathode and anode, respectively.

$$H_2O(g) + energy \rightarrow\ H_2(g) + \frac{1}{2}\,O_2(g); \tag{2.4}$$

$$Anode : O^{2-} \rightarrow\ \frac{1}{2}\,O_2 + 2e^- \tag{2.5}$$

$$Cathode : H_2O + 2e^- \rightarrow\ H_2 + O^{2-} \tag{2.6}$$

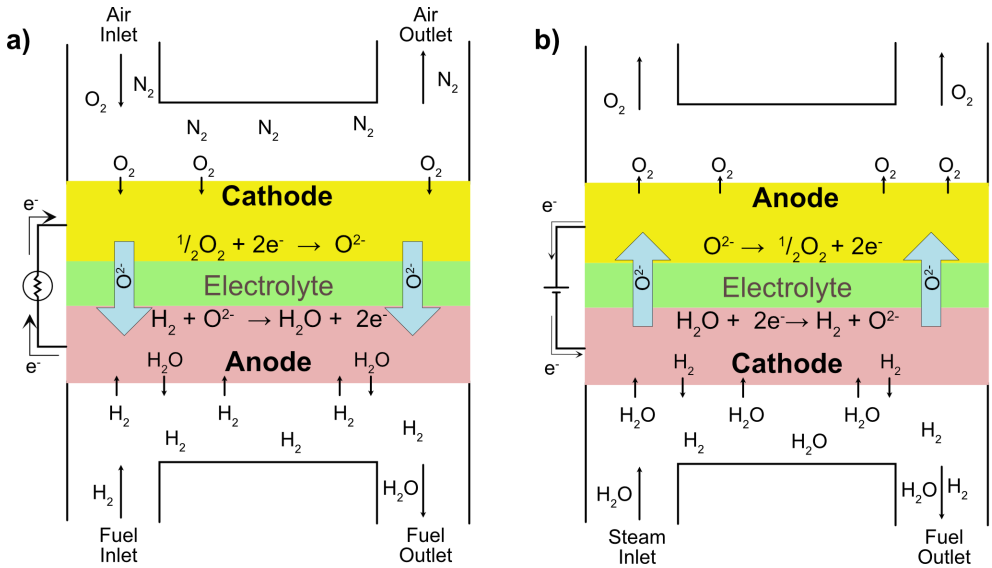

Figure 2.2: Operating principle of (a) solid oxide fuel cell and (b) solid oxide electrolyser cell. Adapted from [16]

The water electrolysis reaction can be separated into two electrochemical half-reactions: oxidation [Equation (2.5)] and reduction [Equation (2.6)]. During this process, electrons from the external source reduce water, producing hydrogen and oxygen ions. The oxygen ions are transported through the electrolyte from the cathode to the anode, where they form oxygen.

More than 99% of the global production of hydrogen is from fossil fuels through thermochemical processes, such as steam reforming, auto-thermal reforming (ATR), partial oxidation (POX), pyrolysis, and gasification, all of which emit CO_2 [7]. Environmentally friendly and carbon-neutral hydrogen can be produced by the electrochemical splitting of water using renewable energy sources. The green hydrogen produced can be used in various processes, as shown in Figure 1.1. Besides this, electrolysis has a wide variety of applications, e.g., synthesis of materials and chemicals, extraction of metals, recycling, and energy storage [17].

There are four main types of electrolysis cells used for hydrogen production, based on the electrolyte used [17]:

1. Alkaline water electrolysers (AWE)
2. Alkaline anionic exchange membrane Water electrolysers (AAEMWE)
3. Proton exchange Membrane Water electrolysers (PEMWE)
4. Solid oxide electrolysis cells (SOEC)

AWE and AAEMWE use hydroxide ions (OH^-) as the ionic carrier but differ regarding the electrolyte used. AWE uses a non-ion-selective separator, while AAEMWE uses an anion-exchange membrane. On the other hand, PEMWE uses protons (H^+), and SOEC uses oxide ions (O^{2-}) as the ionic carriers. The electrolysis cells vary with respect to operating temperatures, electrolytes, performance characteristics, and materials used. The most commonly used electrolyser is AWE, which operates in the temperature range of 70°-90°C. Depending on the scale of production, electricity can account for up to 75% of the cost of producing hydrogen [17]. For an electrolysis reaction, the theoretical potential, or Nernst potential, is a function of temperature. Although the total enthalpy of Reaction 2.4 increases with temperature, the increase is small compared to the drop in the required electrical energy [18]. Therefore, operating electrolysis at higher temperatures requires a lower applied voltage for the electrolysis reaction.

SOEC operates at high temperatures and is based on an oxide ion-conducting ceramic electrolyte, similar to the SOFC. Figure 2.2b illustrates the working principle of the SOEC for water electrolysis. SOECs, when coupled with renewable energy sources, represent a promising way to produce hydrogen in the Hydrogen Economy. High-temperature electrolysis offers specific advantages over low-temperature electrolysis, including [18]:

1. The low theoretical decomposition voltage and higher electro-catalytic activity make electrolysis efficient at high temperatures.

2. Cheap thermal energy from various sources can be utilised to lower the electricity costs, thereby reducing the hydrogen production costs.

3. SOECs can be used to synthesise syngas (H_2 + CO) or can be thermally integrated into a wide range of chemical synthesis processes.

2.3 Solid oxide cell materials

SOCs can operate in a fuel cell or electrolyser mode. An SOC comprises an anode, cathode, and electrolyte. The designations of the cathode and anode change depending on the operation mode (SOFC or SOEC). Correspondingly, the electrodes are referred to as the 'air electrode' and 'fuel electrode' to avoid confusion. By stacking individual cells in series, a higher power density can be achieved. Interconnects are used to connect electrically and separate physically the individual cells. Figure 2.3 depicts the SOC stack. Despite its many advantages, the commercialisation of SOFC and SOEC is hindered by high costs and high degradation rates, including chemical interactions with other materials, high-temperature corrosion, and mechanical failure [16]. For large-scale commercialisation of SOC, low-cost materials and manufacturing methods that can tolerate 80,000 hours of operation are necessary. The following sections will discuss the material requirements and the state-of-the-art materials for different components of the SOC.

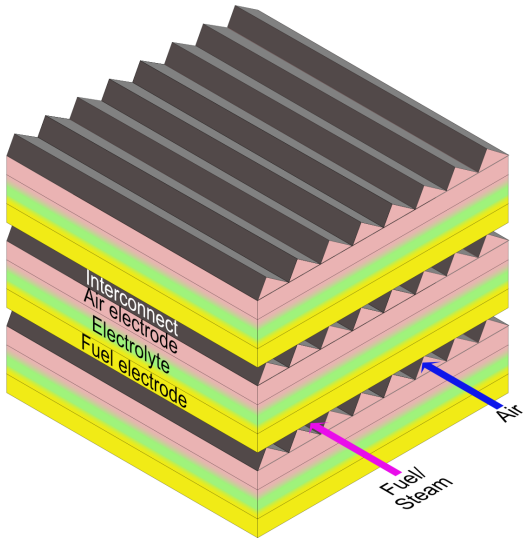

Figure 2.3: Illustration of a solid oxide cell. Adapted from [16]

2.3.1 Electrolyte

In SOC, the electrolyte material must meet several requirements, such as good ionic conductivity, low electrical conductivity, lack of permeability to gases, and stability in fuel and oxygen atmospheres [19]. Moreover, the material must have sufficient mechanical strength, as well as thermal and chemical stabilities [20]. The most commonly used electrolyte is yttria-stabilised zirconia (YSZ), which is zirconia (ZrO_2) doped with yttria (Y_2O_3) [19, 21]. YSZ provides a good balance of ionic properties, mechanical strength, conductivity and cost. Another popular electrolyte choice is cerium oxide (CeO_2) doped with about 20% gadolinium oxide (Gd_2O_3) (CGO) [22]. CGO has higher ionic conductivity than YSZ, allowing for lower operating temperatures. At temperatures below 800°C, the conductivity of CGO is two orders of magnitude higher than that of YSZ. However, CGO has the disadvantage of higher electronic conductivity at lower oxygen partial pressures (fuel side), leading to higher leakage currents and decreased power output [23].

2.3.2 Electrode materials

In contrast to electrolytes, electrode materials must be porous to create a large surface area, so as to maximise the contact area with reactant gases. The electrochemical reactions in the SOC occur at the electrodes. Thus, the electrodes must possess catalytic properties to enhance the reaction rate and reduce polarisation losses. Moreover, they should have good conductivity for both ions and electrons. High ionic and electronic conductivities can be achieved through composites containing materials with high ionic and electronic conductivity. A common practice is to create a gradient of electrode and electrolyte materials [23]. This also reduces the thermal stresses resulting from the differences in Thermal Expansion Coefficient (TEC) of the electrodes and electrolyte.

Fuel electrode
The state-of-the-art material for the fuel electrode is a porous cermet that consists of nickel and electrolyte material [23, 24]. The fuel electrode must be stable at the operating temperature over a wide range of pO_2. During operation, the pO_2 levels vary throughout the cell due to increased H_2O at the outlet in the fuel cell mode [25] and decreased H_2O at the outlet in the electrolyser mode. The composite of Ni + YSZ/CGO ensures good adhesion and has a TEC similar to those of other components. SOFC stacks are designed to use carbon-containing gases as fuels; using Ni in the electrode enhances the catalytic activity for the water-gas shift and reforming reactions. Coarsening of the Ni particles in the fuel electrode over time results in performance degradation [26].

Air electrode
The state-of-the-art materials for the air electrode are highly conductive perovskites based on strontium-doped lanthanum magnetite (LSM) [23]. Since noble metals are too expensive, oxides with high electronic conductivity are used as air electrode. The air electrode must remain stable at the operating temperature at high pO_2 pressures. The SOFC air electrode must have high catalytic activity towards the oxygen reduction reaction. The major limitation of LSM is its poor oxygen ion conductivity, resulting in a smaller triple-phase-boundary (TPB) area. This can be improved by the addition of YSZ [27]. LSM has low oxide ion conductivity at temperatures below 800°C [23]. Alternative materials, such as strontium and iron-doped lanthanum cobaltite ($La_{1-x}Sr_xCo_{1-y}Fe_yO_3$; LSCF) have higher electronic conductivities, making them promising alternatives for intermediate temperature SOFC [19].

2.3.3 Interconnects

To achieve higher voltages, multiple cells are electrically connected in series with the help of interconnects so as to form a fuel cell stack (Figure 2.3). The interconnects distribute the electrical current to the cells and separate the atmosphere at the air electrode of one cell from the fuel electrode of the next cell. The basic requirements for the interconnect materials are similar to those for the electrolyte. However, while the electrolyte is a good ionic conductor and a poor electronic conductor, the interconnect must be a good electron conductor and a poor ionic conductor. The main requirements for the interconnects [23, 28] are:

- Stability at the operating temperature with air and fuel environments on either side, with operation for at least 80,000 hours [29]
- Similar TEC to those of the other cell components
- Good electrical conductivity and low ionic conductivity throughout the stack lifetime.
- Chemical compatibility with other cell components.
- Impermeable to gases
- Sufficient mechanical strength.
- Ease of manufacturing and low cost.

Ceramic interconnects
Traditionally, perovskite-type ceramics based on rare earth chromites, such as CaO- or SrO-doped $LaCrO_3$, have been used to manufacture interconnects for use at operating temperatures > 1000°C [23]. While ceramic materials offer high stability in fuel and air on either side and are similar in TEC to the other cell components, they are expensive, difficult to fabricate, and possess low mechanical strength. In addition, the electrical and thermal conductivities of p-type semiconductors are much lower than those of metals [30]. As a result, perovskite-type ceramics are rarely used as interconnects in fuel cell stacks.

Metallic interconnects
Improvements in materials and manufacturing technologies have allowed the operating temperature of SOCs to be lowered to the range of 600°-900°C. This has made it possible to use metallic materials as interconnects, which have several advantages over ceramic materials. Metallic materials have higher mechanical strength, superior thermal and electrical conductivities; are easier to manufacture and are less expensive. However, they are unstable at high temperatures. Among the possible candidates, alloys that form an oxide scale of chromia have been extensively studied for use as interconnects because they exhibit good oxidation resistance at high temperatures and good electrical conductivity of the oxide scale. One of the main challenges encountered when using metallic materials as interconnects is their susceptibility to high-temperature corrosion, as discussed in detail in Section 4.1.

2.3.4 Balance of Plant

The SOC system is composed not only of the SOC stack, which consists of repeated units of the anode, cathode, electrolyte, and interconnects, but also of various auxiliary equipment known as the balance of plant (BOP). The BOP includes the cell frame, cathode pre-heater, heat exchangers, thermal management equipment, piping, pumps, fuel processors, exhaust burner, control systems, start-up heater, and power conditioner, all of which support the operation of the SOC stack [11]. The cathodic pre-heater pre-heats the reactant gases, which protects the ceramic stacks from thermal stresses induced by rapid temperature changes. Heat exchangers recover high-quality thermal energy from the exhaust gas, while the exhaust burner burns off any remaining fuel in the exhaust. It is worth noting that the BOP in the SOFC system can account for up to 75% of the total system manufacturing cost [11].

BOP components experience harsh operating conditions. Therefore, some of them are manufactured using ceramics [31]. However, with the decrease in operating temperature, the focus has shifted to metallic materials. Metallic materials have greater strength, lower cost, and can be more easily fabricated than ceramics. They also reduce the material consumption and the weight of the SOFC system, making them attractive for mobile applications. However, the metallic materials used in the BOP are subject to high-temperature corrosion, as discussed in Section 4.2. Despite their significant associated costs, research on BOP materials is very limited.

3 Corrosion of Steels

Corrosion is a gradual degradation of a material (usually metallic materials) by reaction with the environment. When exposed to conditions under which they are not thermodynamically stable, metallic materials convert to more stable forms such as oxides, hydroxides, or sulphides. Oxidation is a particular form of corrosion in which metals and alloys react with oxygen to form oxides, which is the focus of this work. The reaction between the metal (M) and the oxygen gas (O_2) is shown in Equation (3.1):

$$aM + \frac{b}{2}O_2 \rightarrow M_aO_b \tag{3.1}$$

With the exception of some noble metals, all metals are thermodynamically unstable and form oxides when exposed to an oxygen-containing atmosphere at ambient temperature. The reaction rates for oxide scale growth are low at ambient temperatures under dry conditions, so most metals do not appear to be affected by oxidation. However, the reaction rates are higher at higher temperatures, which means that oxide scale growth is problematic for metallic materials used at high temperatures. The oxidation behaviour of the metal is influenced by thermodynamics and kinetics, which are discussed in the following sections.

3.1 Thermodynamics

Thermodynamics predicts the ability of a metal to form an oxide at a given temperature and under certain atmospheric conditions. The Gibbs free energy of a system, calculated using Equation (3.2), helps determine the stability of the metal or oxide at a constant temperature and pressure.

$$G = H - TS \tag{3.2}$$

where G is the Gibbs free energy, H is enthalpy, S is entropy, and T is the absolute temperature. The driving force for Reaction (3.1) is related to the change in the Gibbs free energy associated with the conversion of metal to oxide. If the change in the Gibbs free energy (ΔG) is

- $\Delta G > 0$, Reaction (3.1) is thermodynamically impossible.
- $\Delta G = 0$, Reaction (3.1) is in equilibrium.
- $\Delta G < 0$, Reaction (3.1) is spontaneous.

The change in Gibbs free energy ΔG for Reaction (3.1) is shown in Equation (3.3):

$$\Delta G = \Delta G^o + RTln\frac{a_{M_aO_b}(s)}{a^a_{M(s)}a^{\frac{b}{2}}_{O_2(g)}} \tag{3.3}$$

where ΔG^o is the standard free energy change for the formation of M_aO_b, a_x is the activity of the products and reactants, R is the ideal gas constant, and T is the absolute temperature. The activity of pure solids is 1, while the activity of gases is approximated to the partial pressure, $a_{O_2} = p_{O_2}$. At equilibrium $\Delta G = 0$, Equation (3.3) can be represented as Equation (3.4):

$$\Delta G^o = RTln(p_{O_2}^{\frac{b}{2}}) \tag{3.4}$$

Equation 3.4 can be used to evaluate the stabilities of metals and oxides at a given temperature and pO_2. The oxygen pressure at which the oxide is in equilibrium with the metal is called the dissociation pressure. For oxidation to occur, the pO_2 in the atmosphere needs to be higher than the dissociation pressure. The Ellingham diagram, shown in Figure 3.1, plots the standard free energies of oxide formation as a function of temperature for various metals. The nomographic scale on the right provides information about the pO_2 required for oxidation to occur at a given temperature.

The Ellingham diagram can be used to compare the stabilities of different metals and oxides over a wide range of temperatures. The lower the line on the Ellingham diagram, the higher the stability of the oxide, and vice versa. Thermodynamics can only predict the existence of a phase at a given temperature and partial pressure under equilibrium conditions. However, the oxidation of metals depends mainly on the kinetics, which will be discussed in the following section.

3.2 Kinetics

Oxidation kinetics describes the evolution of the oxide scale over time. It is a critical factor in predicting the lifespans of high-temperature components. The oxidation rate is influenced by factors such as temperature, pO_2, pre-treatment of the metal, and the elapsed time of oxidation [33]. The most commonly used method to study the oxidation kinetics is to monitor the changes in mass over time. As the metal absorbs oxygen from the atmosphere and forms an oxide, its mass increases. However, this method does not accurately represent the oxidation kinetics in cases of oxide spallation or oxide evaporation. Other methods to study oxidation kinetics include microscopy, chemical analysis of oxidised specimens, etc. [33].

The commonly encountered oxide growth mechanisms are linear, logarithmic, and parabolic (Figure 3.2). Oxidation often follows a combination of different rate equations. This may be because oxidation occurs through two simultaneous mechanisms or because the rate-determining mechanism changes due to changes in the nature of the oxide scale.

Linear rate equation Linear oxidation is described by Equation (3.5):

$$\Delta m = kt + C \tag{3.5}$$

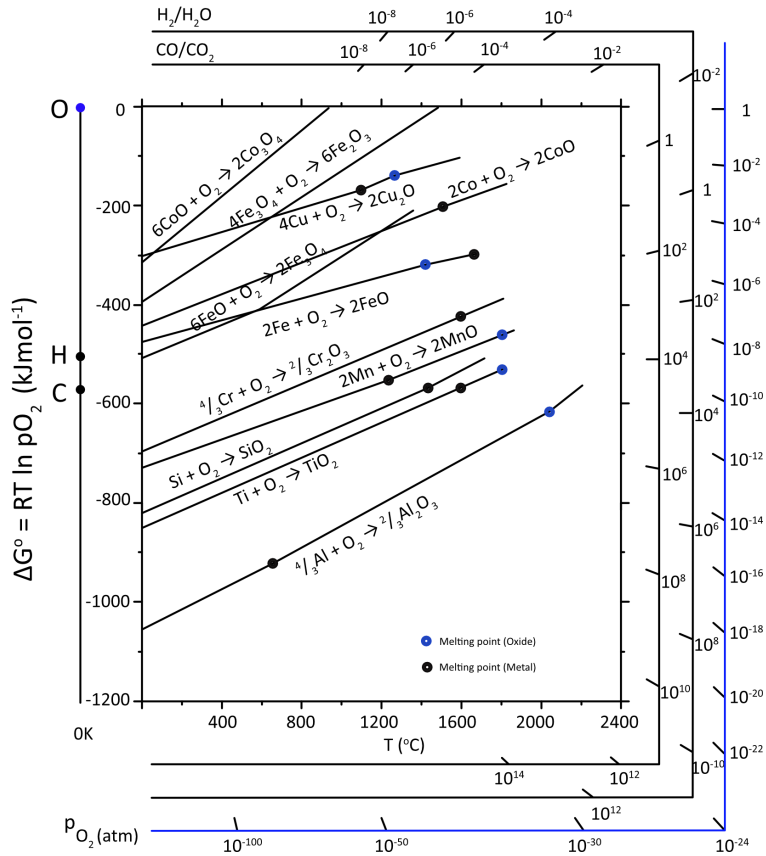

Figure 3.1: Ellingham diagram adapted from [32]. Standard free energy of formation for selected oxides vs temperature

where Δm is the mass change, k is the linear rate constant, and C is the integration constant. In linear oxidation, the oxidation rate is constant and is independent of the amount of metal or gas consumed. This means that the oxide scale is not protective. It is observed when the surface or phase boundary process is the rate-determining step [33].

Logarithmic rate equation Logarithmic oxidation is described by Equation (3.6):

$$\Delta m = k_{log} log(t + t_o) + C \tag{3.6}$$

where Δm is the mass change, k_{log} is the logarithmic rate constant, t is the exposure time, and C is the integration constant. The reaction proceeds rapidly initially, followed by negligible rates. Many metals follow logarithmic oxidation in the temperature range of 300°-400°C and when the oxide scale is very thin [33]. Several theories for the rate-determining step, such as chemisorption and transport of electrons and ions due to the electric field, have been proposed but the general consensus is elusive [34].

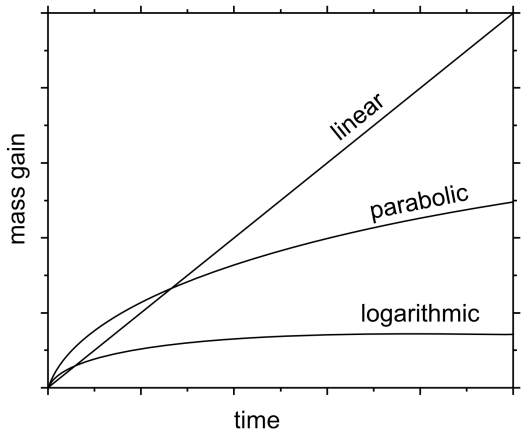

Figure 3.2: The changes in mass over time for three common oxide growth mechanisms. Adapted from [33].

Parabolic rate equation Parabolic oxidation is described by Equation (3.7):

$$\Delta m^2 = k_p t + A \tag{3.7}$$

where Δm is the mass change, k_p is the parabolic rate constant, t is the exposure time, and A is the integration constant. Many metals follow parabolic oxidation at high temperatures. This can be explained based on a theory developed by Wagner in 1933. The main assumptions for this theory are that the oxide scale is dense and well-adherent, the rate-determining step is the diffusion of ions through the oxide scale, the interfaces (such as metal-oxide and oxide-gas) are in thermodynamic equilibrium, and the oxygen solubility in the metal is negligible [35]. Since the rate-determining step is the diffusion of ions, the oxidation rates of metals following the parabolic rate law decrease as the thickness of the oxide scale increases.

Breakaway oxidation
Alloys developed for high-temperature applications rely on the formation of a dense, well-adherent, slow-growing, protective Cr or Al oxide scale on the surface of the alloy. The formation of the protective oxide layer results in a gradual reduction of the alloy's oxide scale-forming element, which is often Cr or Al. This reduction may ultimately cause the protective oxide scale to fail after extended periods of use. When the slow-growing protective oxide layer cannot be sustained due to the oxide scale-forming element (Cr or Al) falling below a critical level, this results in the oxidation of the base material. This phenomenon is called 'breakaway oxidation. Breakdown of the protective oxide leads to rapid oxidation through the formation of non-protective oxide scales, which follow the linear rate law. This can occur due to (a) mechanically induced chemical failure, e.g., when the oxide scale breaks or cracks due to growth stresses or thermal cycling; or (b) intrinsic chemical failure, where the element forming the protective layer falls below a certain threshold and can no longer form a protective oxide [33].

3.3 Scale formation and growth

The formation of the initial oxide scale on a metal is a three-stage process, as illustrated in Figure 3.3. In the first stage, oxygen from the environment is adsorbed onto the metal surface. After charge transfer, the O^{2-} and M^{n+} ions are formed, creating an ionic bond between the ions. Subsequently, the metal oxide nucleates at the metal-gas interface and grows laterally to form a continuous scale. Both steps depend on surface orientation, crystal defects on the surface, surface preparation, and impurities in the metal and gas. Since the metal oxide separates the metal from the gas, the growth of the oxide scale in the third step occurs via solid-state diffusion of the metal ions and/or oxygen ions through the oxide scale. Depending on the predominant diffusion process, the oxide scales can be classified as inward-growing, or outward-growing oxide scales [33].

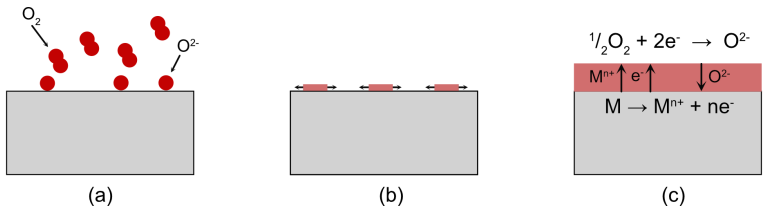

Figure 3.3: Schematic illustration of oxide growth in three steps (a) adsorption (b) oxide nucleation, and (c) oxide scale growth. Adapted from [33]

If the diffusion of ions is the rate-determining step in an oxidation reaction, then the rate of oxidation decreases as the oxide scale becomes thicker. Such oxide scales, which are dense and have low ion diffusivity, are called protective oxides [36]. However, if the oxide scale is porous, then gas transport through the oxide scale is easier, resulting in a higher oxidation rate; this is called a non-protective oxide scale [36].

3.4 Oxide evaporation

Some oxides, such as Cr_2O_3, WO_3, and MoO_3 react with the environment to form volatile metal oxide species [36, 37]. The evaporation of the protective scale leads to accelerated consumption of the protective oxide-forming element in the alloy. Chromia-forming alloys are used extensively for high-temperature applications. However, Cr evaporation limits the applicability of chromia forming alloys at high temperatures and has been extensively studied in the literature [33, 38–40]. Furthermore, Cr evaporation causes cathode poisoning in the SOFC (see Section 4.1).

Chromium oxide reacts with O_2 predominantly at temperatures above 1000°C, to form CrO_3, as shown in Equation (3.8). In the presence of H_2O, the Cr evaporation occurs even at relatively lower temperatures, to form mainly $CrO_2(OH)_2$ as shown in Equation (3.9). From theoretical and experimental evaluations, it is concluded that $CrO_2(OH)_2$ is

the major volatile compound at temperatures below 900°C when H_2O is present in the air [36, 41, 42]. Cr evaporation is affected by various factors such as temperature, humidity, gas flow, and the orientation of the sample with respect to the flow.

$$Cr_2O_3(g) + \frac{3}{2}O_2(g) \rightarrow 2CrO_3(g) \tag{3.8}$$

$$Cr_2O_3(s) + \frac{3}{2}O_2(g) + 2H_2O(g) \rightarrow 2CrO_2(OH)_2(g) \tag{3.9}$$

Mass gain data are used to evaluate the oxidation kinetics and, thereby, the life of a metallic material exposed to high temperatures. However, when there is simultaneous oxidation and Cr evaporation, Cr consumption in the alloy is higher than indicated by the mass gain measurements. In addition, Cr evaporation results in a thinner oxide scale, resulting in a higher oxidation rate. Chromium depletion due to Cr evaporation can result in breakaway oxidation of the material.

3.4.1 Paralinear oxidation

When a chromia-forming alloy is exposed to an environment that contains O_2 + H_2O at high temperatures, oxidation and oxide evaporation occur simultaneously. Oxidation leads to the growth of the oxide scale, while evaporation leads to loss of the oxide scale. Initially, the oxide scale grows faster than the oxide scale is lost due to Cr evaporation, resulting in a positive net mass gain. As the oxide scale becomes thicker, the oxidation rate decreases. At some elapsed time, the oxide scale growth due to oxidation is equal to the oxide scale lost to Cr evaporation, at which point the critical thickness of the oxide scale is reached [43]. Once the critical thickness of the oxide scale is reached, mass loss is observed due to the continuous loss of Cr species by evaporation. The oxidation phenomenon with a combination of parabolic oxidation and linear evaporation is called 'paralinear oxidation', as shown in Figure 3.4 [43, 44].

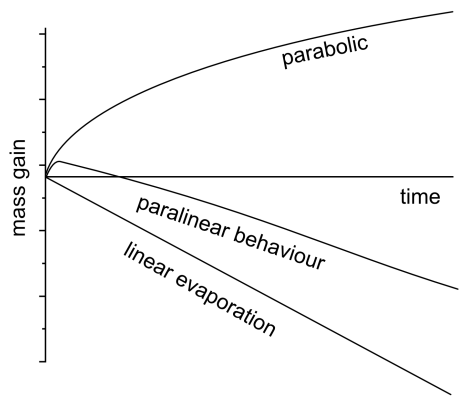

Figure 3.4: Paralinear oxidation behaviour. Adapted from [43, 45]

4 Metallic materials in SOC

At the high operating temperatures (in the range of 600°- 900°C), the metallic materials used in SOCs face the challenge of high-temperature corrosion. Metallic materials that are designed for high temperatures in air rely on the formation of a passivating oxide layer that retards and protects the metallic material from rapid oxidation. Alloys that are capable of forming adherent scales of SiO_2, Al_2O_3 or Cr_2O_3 are usually preferred for high-temperature applications. To ensure long operational lifetimes for the SOFC system, the metallic materials used must have good resistance to high-temperature corrosion. However, additional factors, such as strength, design constraints, applications, temperature, and cost, also play important roles in material selection. This chapter explores the challenges associated with using metallic materials in SOC interconnects and BOP components.

4.1 Interconnect steels

The functions and requirements of the interconnect materials are described in Section 2.3.3. Metallic interconnects have replaced the traditionally used ceramic interconnects in SOCs operating in the temperature range of 600°-900°C. As the interconnects electrically connect the individual cells, the growth of an oxide scale on the interconnect will increase the electrical resistance across the stack, thereby reducing the performance of the SOC. While SiO_2 and Al_2O_3 oxide scales have excellent oxidation resistances, their electrical conductivities are extremely low, making them unsuitable for interconnect applications. Cr_2O_3 is a semiconductor in the operating temperature range of the SOC, and has better conductivity than either SiO_2 or Al_2O_3 [33]. Cr_2O_3-forming alloys represent a good compromise between high-temperature oxidation resistance and oxide scale electrical conductivity. Thus, Cr_2O_3-forming materials have been extensively investigated for use as SOFC interconnects.

4.1.1 Material Selection

There exist numerous commercially available chromia-forming alloys, such as ferritic stainless steels (FSS), austenitic stainless steels, Cr-base alloys, and Ni-base alloys. Of these, Ni-base alloys are considered the best performers at high temperatures [46]. Nevertheless, only FSS and Cr-base alloys are deemed suitable for interconnect applications because their TEC matches well with the other cell components. Cr-base alloys such as Plansee Ducrolloy ($Cr_5Fe_1Y_2O_3$) were initially favoured as substitutes for ceramic interconnects due to their excellent corrosion and electrical properties [47]. However, FSSs have replaced the Cr-base alloys as the material of choice for interconnects, as they are easier to manufacture and less expensive. FSS have a body-centred cubic crystal structure. The TEC of ferritic steel ranges from 11.5 * $10^{-6}K^{-1}$ to 14 * $10^{-6}K^{-1}$, which is similar to that of the other ceramic components in the SOC (TEC = 10.5 - 12.5 * $10^{-6}K^{-1}$) [48]. Consequently, FSS with Cr contents in the range of 16–23 wt% are extensively studied for the large-scale manufacturing of interconnects [49].

Although FSS have several advantages over ceramics for interconnect applications, foremost are ease of formability, and lower cost, they also have specific issues that can impact the long-term operation of SOFC stacks:

- The operation of FSS at high temperatures results in the growth of a chromia scale on the interconnect. This increases the electrical resistance across the stack, which deteriorates the cell performance. Thicker chromia scales can also lead to scale spallation, resulting in the loss of electrical contact with the electrodes.
- At the SOFC air electrode, the chromia scale reacts with oxygen in the presence of water vapour to form volatile Cr (VI) species such as $CrO_2(OH)_2$, as described in Section 3.4. These volatile species then react with the cathode and get deposited at the active triple-phase boundaries, hindering the oxygen reduction reaction. As a result, the electrochemical activity of the cathode is reduced, leading to the degradation of SOFC performance over time. This process is commonly known as 'chromium poisoning' [50]. However, Cr evaporation is minimal in SOEC due to the lack of water vapour at the air electrode.
- Cr evaporation and oxide scale growth result in the depletion of the Cr in the steel. When the Cr content of the steel falls below a certain threshold, breakaway corrosion occurs, leading to rapid degradation of the stack.

4.1.1.1 Effect of alloying elements

FSS contain minor alloying elements, in addition to Fe and Cr, which are either intentionally added or remnants from the steel-making process that are expensive to remove. Some of these minor alloying elements significantly influence the degradation mechanisms in FSS.

Manganese
Manganese is an important minor alloying element in all FSS used for interconnect applications. Upon oxidation, Mn diffuses through the chromia scale and forms a $(Cr, Mn)_3O_4$ spinel on the chromia scale. Several studies have shown that the $(Cr, Mn)_3O_4$ spinel reduces Cr evaporation by a factor of 2-3 compared to the Cr_2O_3 scale at 800 °C [38, 51]. However, Cr evaporation is still high for the long-term operation of SOFCs. The conductivity of the $(Cr, Mn)_3O_4$ spinel is at least one order of magnitude higher than that of Cr_2O_3 [52, 53].

Silicon and Aluminium
Silicon and aluminium are residual elements of the steel production process, where they are used as de-oxidisers [54]. Si and Al require a lower oxygen activity than Cr to oxidise and are oxidised internally underneath the chromia scale due to their lower concentrations. Their presence at concentrations above a certain threshold leads to the formation of subscales, such as SiO_2 and Al_2O_3, resulting in two main issues. First, electrically insulating oxides increase the electrical resistance across the cell [55–57]. Second, the SiO_2 subscale has been reported to reduce the adhesion of the oxide scale to the metal,

due to the dissimilar TEC between the alloy and SiO_2 [39, 58]. To remove Si and Al from steel, an additional vacuum induction melting process is required, which adds to the manufacturing costs.

Refractory elements
Refractory elements, such as Nb, W, and Mo, are added to form Laves phases, such as $(Fe, Cr)_2(Nb, W, Mo)$. Laves phases are known to bind Si and hinder the formation of SiO_2 [55]. Moreover, Laves phases increase the hardness and creep resistance of steel by impeding dislocation motion [56]. However, increasing the Nb content is also reported to increase the oxidation rate of FSS due to doping with Cr_2O_3 [56].

Titanium
Titanium is added to the steel to increase the stability of the ferrite structure at higher temperatures. Ti, along with Nb, W, Mo, and Cr, stabilise the ferrite structure at high temperatures. In similarity to Si and Al, Ti undergoes internal oxidation beneath the chromia scale. Ti internal oxidation is reported to prevent oxide scale buckling by increasing the strength of the material underneath the oxide scale [59]. Moreover, Ti increases the conductivity of the oxide scale due to doping [60], which also results in increased oxidation of the chromia scale [61].

Reactive elements
In 1937, Pfeil [62] discovered that adding small amounts of rare-earth elements, such as Y, Sc, Ce, and La to alloys that form Cr_2O_3 greatly enhanced their oxidation resistance. This beneficial effect of minor additions of Reactive Element (RE) belonging to the rare earth element group such as Y, Zr, Ce, Hf, and La on high-temperature oxidation is well established in the literature, and is known as the reactive element effect (REE) [63–68]. The most common effects of the reactive elements are:

- Decrease in the oxidation rate of the material.
- Improvement of scale adhesion and resistance to spallation.
- Modification of the oxide scale microstructure.
- Enhancement of the selective oxidation of Cr in the alloys.
- Change in the growth mechanism of the oxide scale in chromia formers.

The above-mentioned effects are evident even for small additions (0.01-0.5 wt%) of reactive elements [63]. Although the mechanism for the reactive elements is not yet fully understood, the most prominent hypothesis is that they change the growth mechanism of the oxide scale in chromia formers. A non-doped Cr_2O_3 scale grows predominantly via the outward diffusion of metal cations. In the Cr_2O_3 scale doped with reactive element, the outward diffusion of the metal cations is inhibited by the reactive element that segregates at the oxide grain boundaries. As the smaller oxygen anions are unaffected, the growth of the chromia scale changes from predominantly outward migration of Cr ions to inward

diffusion of oxygen ions [63, 69–71]. This change in diffusion results in a lower oxidation and increased scale adhesion. Pieraggi et al. [72] have proposed a model whereby the reactive elements segregate at the metal-oxide interface by creating a "poisoned interface". Reactive element segregations at the metal-oxide interface impede the annihilation of Cr vacancies ($V_{Cr}^{'''}$), reducing the overall driving force for the outward transport of Cr^{3+} ions, which results in changes to the growth direction and scale growth kinetics. Reactive elements also prevent the detrimental effect of sulphur by sequestering it and preventing it from segregating at the surface, which weakens the interfacial bonding at the metal-oxide interface [73, 74]. Thus, reactive elements improve oxide scale adhesion and interfacial bonding. Several other mechanisms have been proposed for the benefits of reactive element additions [63, 64, 75–77].

Reactive elements can be added to the steel melt during production, as is the case for Crofer 22 APU, Crofer 22 H, and Sanergy HT. However, adding reactive element during steel production increases the overall manufacturing cost, making these steels expensive. Other methods of applying reactive elements include dispersing of reactive element oxides in the alloy or coating the surface with a thin layer of reactive element [78, 79]. Coating the surface with reactive elements is applicable to SOFC interconnects, which will be discussed in detail in Section 4.1.2.

4.1.1.2 Tailor-made steels

Tailor-made steels for interconnect applications are developed by adding and removing certain minor alloying elements so as to improve performance, thereby ensuring long-term operation. The commercially available tailor-made steels developed for interconnect applications are Crofer 22 APU, Crofer 22 H, Sanergy HT, and ZMG232. These steels share the following common features:

- A high Cr content (approximately 22%), to ensure the formation of a chromia scale during long-term operation. Further increasing the Cr content leads to the undesirable formation of a brittle sigma phase.
- Minor addition of Mn (< 1 wt%) to form $(Cr, Mn)_3O_4$ spinel on the chromia scale, reducing Cr evaporation.
- Addition of reactive elements such as La, Ce to improve the oxidation resistance and oxide scale adhesion.
- Impeding SiO_2 subscale formation either by having a low Si content in the alloy, as in the cases of Crofer 22 APU and ZMG232 G10, or by adding refractory elements to bind Si, as in the cases of Crofer 22H and Sanergy HT.

Despite the improved performances of tailor-made steels, they still exhibit high Cr evaporation and chromia scale growth. Furthermore, the addition of reactive elements and enforcement of stringent requirements, combined with low production volumes, make these steels expensive. Interconnects contribute significantly to the total material cost of a

SOFC stack [11]. Therefore, there is a strong incentive to reduce the cost of interconnects, which in turn reduces the overall cost of the SOC stack. One approach to reducing interconnect costs is to replace tailor-made steels with widely available, low-cost FSS such as AISI 441, AISI 444, and AISI 430. These low-cost FSS contain approximately 16-19% Cr, 0.3-0.6% Mn, and minor alloying elements such as Nb, Ti, Mo, and W. However, the main disadvantages of using low-cost FSS are the lower Cr contents and the possibility of SiO_2 subscale formation. Therefore, these steels are mainly explored for intermediate temperature SOFCs with operating temperatures below 800°C.

4.1.2 Protective coatings

Despite the progress made in adapting steel chemistry for SOFC interconnects, the high oxidation rates and Cr evaporation make it impractical to use uncoated FSS as interconnect materials. In order to remain competitive in the market, SOFCs must have a service life of up to 80,000 hours [80]. Protective coatings offer an alternative approach to modifying alloys, where a metallic interconnect surface is modified by the addition of a protective layer. Certain coatings have been proven to be effective at reducing Cr evaporation, and chromia scale growth [81–83].

The criteria for these coatings are similar to those for the interconnects, such as a TEC identical to the other cell components, good electrical and thermal conductivities, ease of manufacturing, chemical compatibility with adjacent cell components, good adhesion, and low cost. In addition, coatings should be effective at mitigating Cr evaporation and oxide scale growth. Protective coatings have been the subject of numerous studies, which vary in terms of their constituent elements, compositions, and deposition techniques. Most of the coatings developed for interconnect applications can be broadly divided into two groups: perovskite coatings, and spinel coatings.

Perovskite coatings

The general formula for the perovskite structure is ABO_3, where the A sites are occupied by low-valence cations such as La, Sr, Ca, and Pb, and the B sites are occupied by higher-valence transition metal cations such as Ti, Co, Fe, and others. Perovskite coatings exhibit p-type electronic conduction in an oxidising environment and are commonly stable under low oxygen partial pressures (pO_2) [81, 84]. The most commonly researched perovskite coatings for interconnect applications are lanthanum chromite ($LaCrO_3$), lanthanum strontium chromite ($La_{1-x}Sr_xCrO_3$), lanthanum strontium manganite ($La_{1-x}Sr_xMnO_3$), lanthanum strontium cobaltite ($La_{1-x}Sr_xCoO_3$), and lanthanum strontium ferrite ($La_{1-x}Sr_xFeO_3$). These coatings can be deposited using radio-frequency magnetron sputtering, sol-gel dip coating, and screen printing [82]. They have high electronic conductivities and similar TECs to other ceramic components. However, thicker coatings are required to decrease the oxidation rate, and the coatings often show poor adhesion to the substrate [81]. Despite improvements, ionically conductive perovskites are not effective barriers to volatile Cr species [38].

Spinel coatings
Spinels are oxide materials with the general formula of AB_2O_4, where A and B are usually divalent, and trivalent cations occupy the octahedral and tetrahedral sites in the face-centred cubic oxygen anion lattice [82]. By adjusting the choice and ratio of A and B cations, the properties of spinels, such as conductivity, thermal and electrical properties, and TEC, can be tailored to a specific application. Spinels are of interest due to their ability to suppress Cr evaporation. For further information on the thermal and electrical properties of various spinels, the reader is referred to [85].

Manganese Cobalt Oxide (MCO) coatings have been extensively researched for interconnect applications. They are considered promising for the air side of the interconnects as they have demonstrated a reduction in Cr evaporation and ASR across the interconnect [86–88]. The $(Co, Mn)_3O_4$ spinel has a conductivity in the range of 6.4–60 Scm^{-1} at 800°C and a TEC in the range of 11.5-14.4 * $10^{-6}K^{-1}$ in the temperature range of 25°-800°C [85]. Several attempts to enhance the conductivity of the $(Co, Mn)_3O_4$ spinel by doping it with Co, Cu, and Fe have been reported [82, 83, 89]. These coatings can be deposited using various techniques, such as sol-gel dip coating, Electrophoretic Deposition (EPD), electroplating, Physical Vapor Deposition (PVD), Atmospheric plasma spraying (APS) coating and screen printing. MCO coatings can also be applied by depositing metallic Co, which upon oxidation and diffusion of the Mn from the steel transforms into MCO. PVD coatings are particularly suitable because they can be efficiently applied in a roll-to-roll, high-volume process, resulting in a lower cost [90]. Using the PVD process, a $(Co, Mn)_3O_4$ spinel coating can be applied to the steel by depositing metallic Co, which oxidises during high-temperature exposure to form a Co_3O_4 spinel. Subsequent outward diffusion of Mn from the steel results in the formation of a $(Co, Mn)_3O_4$ spinel [88].

Reactive element coatings
Reactive element coatings have been proposed for interconnect applications. Even a very thin coating of reactive elements has been shown to have a beneficial effect on the corrosion behaviour of the alloy [91–93]. Moreover, Fontana et al. [91] have shown improvements in the oxidation behaviour and oxide scale adhesion of reactive element oxide (La_2O_3, Nd_2O_3 and Y_2O_3) coated chromia-forming steels such as Crofer 22 APU, AL 453 and Haynes 230. However, a reactive element coating is ineffective at preventing Cr evaporation [79]. Several authors [78, 91, 94] have reported improvements in the electrical properties of oxide scales coated with reactive elements.

The MCO coating and the reactive element coating can be combined to achieve a lower Cr evaporation and improved oxidation resistance. The enhanced behaviours of MCO-coated steels that contain reactive elements in the coatings have been reported in the literature [95–99]. Ce/Co coatings are considered the state-of-the-art coatings, in that they combine the positive effects of both the MCO coating and reactive element coating. A 10 nm Ce and a 600 nm thick Co metallic coating deposited using PVD have been extensively researched for interconnect applications [79, 94, 95, 100–102]. Moreover, the self-healing properties of these coatings allow steel sheets to be shaped into interconnects after coating, which is highly cost-effective [103].

4.1.3 Lifetime prediction of chromia-forming FSS

Most of the alloys used at high temperatures rely on the formation of a slow-growing oxide scale to provide resistance against rapid corrosion attacks. The formation of the protective scale is achieved through the selective external oxidation of the scale forming elements (Cr,Al) during high-temperature service [36]. When the concentrations of these elements fall below the levels needed to sustain the growth of the protective oxide scale during long-term service, the base material begins to oxidise. The consumption of alloy is accelerated, and the rapid oxidation of the alloy is called 'breakaway corrosion' [104]. The oxidation kinetics of the protective oxide scale determines the lifetime of the material. It is desirable to be able to predict the capacity of a material to supply sufficient protective oxide-forming elements (Cr,Al) to the interface. This is especially important in cases where: (i) the total reservoir is small, such as in the thin foils used in SOC interconnects, heat exchangers, heating elements, and tubing [105, 106], or (ii) the surface-to-volume ratio is high, such as in metallic foams [107–109]. Thus, the lifetime prediction for a material (determined as beginning of breakaway corrosion) has been widely studied in the cases of chromia-forming [106, 108, 110–112] and alumina-forming steels [105, 113].

Experimentally, breakaway corrosion is observed to start at the corners and edges partly due to enhanced metal consumption as a consequence of a higher surface-to-volume ratio. In the case of an infinitely large sheet, for which the effect on the edges can be neglected, the diffusion of the oxide scale forming element perpendicular to the sheet determines the oxidation behaviour of the sheet. In the case of FeCrAl alloys, the alumina oxide scales exhibit low growth rates (often deviating from parabolic oxidation kinetics [114]) and have excellent thermodynamic stability. The Al concentration is almost flat, so lifetime modelling of alumina scale forming steels entails a mass balance of Al consumption due to the growth and re-healing of the oxide scale. Quadakkers et al. [115] developed a model to predict the lifetime of a FeCrAl alloy. Young et al. [112] further improved the approach for cases in which a depletion profile is observed, for example, in FCC steels and Ni-based alloys.

In the case of chromia formers, the life-time prediction is more complicated than in the case of alumina formers. The chromia-scale growth is an order of magnitude faster than that of the alumina scale [116]. Cr evaporation influences the Cr consumption in the steel, thereby affecting the lifetime of the material (breakaway corrosion). Moreover, Cr evaporation can create a steep slope in the depletion profile beneath the oxide scale, resulting in breakaway corrosion even when the Cr content in the steel is higher than the critical Cr content for breakaway corrosion. Schütze et al. [111] have shown that a 9%Cr steel is protective for up to 10,000 hours in dry air while suffered breakaway corrosion after 100 hours in the humid air at 650°C. Furthermore, Cr evaporation is significantly influenced by the gas flow conditions and water vapour content [117]. Sachitanand et al. [118] have shown that Fe-22Cr steels undergo breakaway corrosion in 1600 hours under flow conditions of air + 3%H2O at 850°C, while a protective scale is observed up to 3,100 hours under non-flow conditions. Cr evaporation also has a very different activation energy than oxidation [119], meaning that it is differently influenced by temperature.

Furthermore, Gleeson et al. [120] have reported that minor alloying elements exerts significant influences on the lifetime of steels even when the concentrations of minor alloying elements are within the specifications. Moreover, the growth rates of the chromia scales differ in thin and thick specimens [121]. The oxidation behaviours of different steels are different owing to the differences in the Cr contents and alloying elements [122]. The growth of the chromia scale on steel is determined by the oxidation rate (k_p), which is influenced by operating temperature, heat treatment, and surface condition. Thus, steel with a low Cr content has a different Cr consumption behaviour than a steel with a higher Cr content, depending on k_p, making it impossible to extrapolate their lifetimes. Nevertheless, a similar approach to that discussed for FeCrAl alloys [115] has been used to predict the lifetime of chromia formers [106, 110]

4.1.4 Electrical conductivity of oxide scales

The primary function of the interconnect is to conduct electrons, thereby electrically connecting the fuel cells in the fuel cell stack. The main challenge regarding the electrical conductivity of the interconnect is the formation of an oxide scale during high-temperature operation. The conductivity of the oxide scale is several orders of magnitude lower than that of the steel. Therefore, the oxide scale growth increases the overall resistance of the interconnect, decreasing the efficiency of the fuel cell. This degradation can be experimentally evaluated by measuring the Area Specific Resistance (ASR).

The electrical conductivity of a material can be defined using Equation (4.1):

$$\sigma = \sum \mu_i * n_i * q_i \tag{4.1}$$

where μ_i is the mobility, n_i is the number and the q_i is the charge of carrier i. In oxides, the charge carriers are electrons, electron holes, ions, or ion holes. Thus, the conductivity for the oxides can be defined as the sum of the electronic and ionic charge carriers, as shown in Equation (4.2):

$$\sigma = \sigma_{electronic} + \sigma_{ionic} \tag{4.2}$$

The mobility μ_i of electrons decreases, and the mobility μ_i of ions increases with the temperature. The charge carrier concentration n_i increases with the temperature. In oxides, the increased charge carrier concentration and mobility of ions supersedes the decreased mobility of electrons. Therefore, the conductivities of the oxides increase at higher temperatures. In the case of metals, the decreased mobility of electrons supersedes the increased charge carrier concentration, resulting in a decrease in conductivity [33]. The temperature dependence of the electrical conductivity of the oxide scale can be described by the Arrhenius relation in Equation (4.3):

$$\sigma = \sigma_o * exp\left(\frac{-E_a}{R * T}\right) \tag{4.3}$$

where σ_o is the pre-exponential factor, E_a is the activation energy, R is the ideal gas constant, and T is the temperature.

The ASR is commonly used to describe the electrical behaviour of an interconnect, which is independent of the area, as shown in Equation (4.4):

$$ASR = A * R_e = A * \frac{1}{\sigma} * \frac{L}{A} = \frac{L}{\sigma} \tag{4.4}$$

where R_e is the resistance, σ is the conductivity, L is the oxide thickness, and A is the measured area.

Conductivity of chromia
The electrical properties of the interconnect are mostly dependent upon the growth of the chromia scale. Chromia is considered to be an intrinsic semiconductor at temperatures above 1000°C [123] and an extrinsic semiconductor at temperatures below 1000°C [124]. Thus, the electronic conductivity of the chromia scale below 1000°C depends on the pO_2 and is dominated by dopants and impurities. Depending on the dopant and the pO_2, the doped chromia shows either p-type semiconductor behaviour or n-type semiconductor behaviour. Since the pO_2 varies across the oxide scale, some researchers have reported the presence of both n-type and p-type behaviours in the chromia scale [125, 126]. The thermally grown chromia is doped by several alloying elements, such as Ti, Ni, Fe, Mn, and Nb, present in the steel [60, 124, 127]. Usually, the conductivity of the oxide scale is improved by the dopants [60, 128]. The electrical conductivity of the chromia is reported to vary between 0.001 and 0.05 $S.cm^{-1}$ at 800°C [124, 129–131].

Conductivity of spinels
Spinel coatings are extensively used to reduce Cr evaporation, as discussed in Section 4.1.2. Since the coatings are inevitable, it is important to understand the electrical properties of the various spinels proposed as interconnect coatings. Spinels are believed to conduct electrons via a mechanism that involves hopping between the octahedral sites [132]. To act as a good electronic conductor, spinels must be able to accommodate different valence electrons at the octahedral states. The $(Cr, Mn)_3O_4$ spinel has higher conductivity than the Cr_2O_3 scale [52, 53], but has much lower conductivity than the $(Co, Mn)_3O_4$ spinel [85, 133, 134]. This is due to the presence of Cr, which has only one stable oxidation, state Cr^{3+}, and a strong preference to occupy the octahedral sites [85, 135]. An extensive list of the conductivities and thermal expansion values of the various spinels at 800°C can be found elsewhere [85]. Based on that study, $(Co, Mn)_3O_4$ and $(Cu, Mn)_3O_4$ spinels are best suited for the interconnect coating. However, Göebel et al. [136] have shown a minimal influence of coating conductivity on the ASR, as the conductivity of the coating is several orders of magnitude higher than that of the chromia scale.

4.1.5 Dual-atmosphere effect

Research on developing and testing interconnect materials has focussed primarily on simplified conditions (single atmospheres, air/fuel). This approach provides a better understanding of the corrosion phenomena. However, the interconnects in the SOC are exposed to dual-atmosphere conditions, with low pO_2 and high pO_2 on either side. The influence of the dual-atmosphere effect on FSS has been studied by several authors in

recent years [137–146]. Some researchers have reported accelerated corrosion on the air side compared to exposure only to air. In contrast, others have found no detrimental effect of the dual-atmosphere conditions. The anomalous behaviours of FSS, when exposed to dual-atmospheres, is called the "dual-atmosphere effect".

Yang et al. [137, 138] have reported on the detrimental effects of dual-atmosphere conditions on the air side of FSS exposed at 800°C. They have demonstrated the formation of an iron-rich oxide on the air sides of AISI 430 and Crofer 22 APU, with a significant change in the thickness of the oxide scale, which was not observed when exposed to only air. Similar results have been reported by Gannon et al. [139] for AISI 441 at 800°C. In contrast, Skilbred et al. [144] have reported only a minor change to the oxide scale composition, without any change to its structure. Furthermore, Kurokawa et al. [147] and Alnegren et al. [141] have observed no significant dual-atmosphere effect at 800°C. Gunduz et al. [143] have reported a severe dual-atmosphere effect at 800°C on non-pre-oxidised AISI 441, but no dual-atmosphere effect on pre-oxidised AISI 441 at 800°C. The significant differences in the reported intensities of the dual-atmosphere effect may reflect from differences in the surface conditions, pre-treatments, and hydrogen concentration on the fuel side.

While most of the studies discussed above were performed at temperatures $\geq$ 800°C and above, Alnegren et al. [141] have investigated dual-atmosphere effects at lower temperatures (600°-800°C). They have reported that the severe dual-atmosphere effect occurs at 600°C, indicating an inverse temperature relationship. Gunduz et al. [143] have confirmed that the severe dual-atmosphere effect occurs at 600°C, while protective oxide scale formation occurs at 500°C.

Although the dual-atmosphere effect is clearly observed, the mechanism underlying this behaviour is not yet completely understood. Several authors have proposed various mechanisms to explain the abnormal behaviours seen under dual-atmosphere conditions. However, there is a consensus that hydrogen on the fuel side diffuses to the air side and interferes with the oxidation on the air side. Yang et al. [137] have suggested that the incorporation of hydrogen into the oxide scale on the air side alters the defect chemistry, resulting in an enhanced cationic diffusivity. Others have supported this mechanism [144, 145]. Holcomb et al. [148] have suggested that the oxide scale is mechanically disrupted by the formation of steam, which is formed by inward diffusing oxygen and hydrogen. Rufner et al. [145] have proposed that the pO_2 on the air side oxide scale could be locally altered by the diffusing hydrogen. Gunduz et al. [143] have suggested that the Cr diffusion in the steels is impaired in the presence of hydrogen, resulting in the formation of a non-protective oxide scale. Yang et al. [137] have further shown that increasing the Cr content of the steel (17 wt% to 23 wt% Cr) decreased the severity of the dual-atmosphere effect. Despite the numerous studies, further research is required to mechanistically understand and develop mitigation strategies for FSS interconnects.

4.2 BOP materials

BOP components are exposed to various temperatures and atmospheres depending on their locations, functions, and contact with the exhaust. Using Cr_2O_3-forming materials for BOP components raises problems similar to those encountered with the interconnects, such as Cr evaporation. BOP components located upstream of the SOFC can be a significant source of volatile Cr(VI) species [149]. However, unlike the metallic interconnects, which have attracted considerable attention from researchers worldwide, materials for BOP components are often overlooked. Coatings designed to circumvent the drawbacks of metallic interconnects are challenging to implement on BOP components due to the complex geometries of the components.

The metallic materials used for BOP components should have good oxidation resistance, lower cost, and be readily available. Moreover, they should have good mechanical properties, machinability, high thermal conductivity, and long-term creep behaviour. Unlike the materials used for interconnects, there are no restrictions in relation to the conductivity of the scale for the BOP components. Thus, Al_2O_3-forming alloys can be used for this application. With minimal restrictions on the TEC, austenitic steels and Ni-based alloys can be explored for BOP applications.

5 Experimental Setup and Methods

5.1 Investigated materials

Five FSS with thicknesses in the range of 0.30-0.38 mm were studied for interconnect application. Three of these, AISI 430, AISI 441, and AISI 444, are commercial FSSs, while Crofer 22 APU is a tailor-made FSS for interconnect applications. To push the boundaries, AISI 409 with 11.4 wt% Cr was also investigated and compared with the selected steels. The chemical compositions of the investigated steels are listed in Table 5.1. Crofer 22 APU, AISI 444 and AISI 441 are 0.3 mm thick, while AISI 409 and AISI 430 are 0.38 mm thick. The steels were exposed in coupon sizes of 17 mm x 15 mm and 15 mm x 15 mm. These steels were used as substrates for the coatings described in papers I-VI.

Table 5.1: Chemical compositions (in wt%) of the selected steels.

Alloy	Fe	Cr	C	Mn	Si	Cu	Ti	Nb	Mo	RE
Crofer 22 APU	Bal	22.92	0.004	0.38	0.01	0.01	0.06	-	-	0.07
AISI 444	Bal	19.03	0.015	0.35	0.40	-	0.005	0.6	1.86	-
AISI 441	Bal	17.56	0.014	0.35	0.59	-	0.17	0.39	-	-
AISI 430	Bal	16.2	0.04	0.49	0.34	-	-	-	-	-
AISI 409	Bal	11.4	0.012	0.39	0.51	-	0.17	0.39	-	-

Five alloys from four material groups were investigated for their applications in the BOP components. The chemical compositions of the selected alloys are listed in Table 5.2, while Table 5.3 lists their DIN numbers, material groups, and commercial names. The alloys, which had a thickness of 0.5 mm, were cut into 17 mm x 15 mm coupons and exposed without further surface treatment. A197, on the other hand, was obtained as a 2 mm thick sheet, cut into square coupons with dimensions 15 mm x 15 mm x 2 mm, and ground to a thickness of 0.5 mm using SiC paper with a grit #1200 finish. One set of coupons was pre-oxidised at 900°C for 24 h before exposure at 650°C for 500 h.

Table 5.2: Chemical compositions (in wt%) of the selected materials.

Alloy	C	Si	Mn	Cr	Ni	Al	Nb	Fe	Mo	Ti
AISI 441	0.02	0.58	0.42	17.53	0.28	-	0.39	Bal		0.164
AISI 444	0.01	0.37	0.3	18.92	-	-	0.56	Bal	1.85	0.003
Alloy 600	0.02	0.18	0.24	16.25	74.19	0.22	0.08	7.93	-	0.29
Alloy 800H	0.07	0.4	0.6	20.8	30.4	0.28	-	Bal	-	0.3
A197	0.02	1.25	0.1	12.4	-	3.7	-	Bal	Reactive Elements	

Table 5.3: Details of the materials from Table 5.2

Alloy	DIN	Commercial name	Material group	Thickness
AISI 441	1.4509	-	FSS	0.5 mm
AISI 444	1.4521	K44M	FSS	0.5 mm
Alloy 600	2.4816	-	Ni-base alloy	0.5 mm
Alloy 800H	1.4958		Austenitic stainless steel	0.5 mm
A197		Kanthal® EF101	Alumina forming FSS	2 mm

5.2 Coatings

Most of the coatings used in this thesis were deposited using a proprietary physical vapour deposition (PVD) technique at Alleima (formerly Sandvik Materials Technology) [90]. Prior to deposition, the materials were cleaned in a 10% solution of AK 13 (NaOH with tensides) for 10 mins at 60°C, followed by rinsing with tap water and deionised water. The main coating system investigated in this thesis is a Ce/Co coating (10 nm Ce followed by 600 nm Co) deposited using PVD. For exposures performed in air (papers I, II, IV, V, and VI), the coating is deposited on both sides of the substrate. For exposures performed in dual atmospheres (paper III), the coating is deposited only on the side exposed to air. Ce/Co coating on both sides, as well as coatings deposited by collaborators at different universities and research labs, were used in Paper IV. More details of these coatings are presented in Table 6.1 and in Paper IV.

In Paper V, several coatings based on the Ce/Co coating were deposited. In some of the coatings, only Co was used, while in others, Ce was deposited at different locations in the Co coating. Moreover, the coatings were deposited on Crofer 22 APU, which was pre-oxidised for 3 minutes in a box furnace set at 900°C. For more information on the coatings deposited, refer to Section 6.5. The different coatings that were deposited are illustrated in Figures 6.16a and b. In paper VI, Ce/FeNi coatings were compared to Ce/Co coatings. Fe and Ni were co-evaporated for the deposition of Ce/FeNi coatings. The coatings deposited on the various substrates are listed in Table 5.4.

Table 5.4: Details of the coating-steel combinations used in this thesis.

Alloy	DIN	10Ce600Co	20Ce600Co	50Ce600Co	10Ce600FeNi
Crofer 22 APU	1.4760	✓			
AISI 444	1.4521	✓			
AISI 441	1.4509	✓	✓	✓	✓
AISI 430	1.40316	✓			
AISI 409	1.4512	✓			

The coatings were deposited on steel sheets and pre-cut steel, as shown in Figure 5.1. For the pre-cut steel, coupons of 17 mm x 15 mm were etched out of a steel sheet, except for two 1 mm wide sections. The coated coupons on the pre-cut steels have coated faces and coated edges. The coupons from the coated pre-cut steel sheet are referred to as 'precut-coated'. However, the coupons cut from a coated steel sheet, referred to as

'sheet-coated', have coated faces and uncoated edges. All the exposures of the uncoated steels were performed on coupons from pre-cut steels. Unless otherwise specified, the coated steels used for the investigations are pre-cut coated steels.

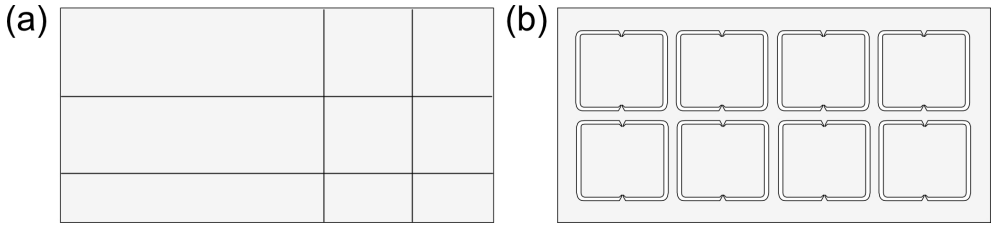

Figure 5.1: Steel used for coating the (a) sheet and (b) pre-cut steel, with coupon dimensions of 17 mm x 15 mm.

5.3 Exposures

All the exposures were carried out in tubular furnaces with a horizontal quartz tube reactor, as shown in Figure 5.2. Most of the exposures were conducted in tube furnaces with a continuous airflow saturated with 3% H_2O, to simulate the airside of the SOFC. The water vapour content of the air was achieved by passing the air through a heated water bath connected to a condenser set at 24.4°C. The water vapour in the air was measured using the Mitchell Instruments Optidew Vision™ chilled mirror humidity sensor. Some of the exposures were conducted in dry air (-19°C dew point). To ensure a flow-independent regime, the airflow was set at 6 lit min^{-1}, corresponding to a linear velocity of 27 $cm.s^{-1}$. A flow restrictor was placed in front of the coupons to minimise natural convection and ensure a more uniform flow pattern. Prior to exposure, all the coupons were degreased and cleaned with acetone and ethanol in an ultrasonic bath at room temperature. At least three identical coupons were used for each exposure, mounted on an alumina holder positioned parallel to the airflow. The exposure conditions, atmospheres and temperatures used in the different papers are presented in Table 5.5

Table 5.5: Exposure atmospheres and temperatures used in the different papers

Paper	air + 3% H_2O	dry air	air +3% H_2O// Ar + 3% H_2O+ 5% H_2	Temperature
Paper I	✓			800°C
Paper II	✓			800°C
Paper III			✓	600°C, 800°C
Paper IV	✓			800°C
Paper V	✓			850°C
Paper VI	✓	✓		850°C
Paper VII	✓			650°C, 850°C

5.3.1 Gravimetry

The oxidation kinetics of the exposed alloys were studied using discontinuous mass gain measurements. For this, coupons were removed from the furnace at regular intervals and allowed to cool down to room temperature. The mass of the coupons was recorded using an XP6 scale (Mettler Toledo). After recording the mass, the samples were placed back in the furnace. The mass gains from the discontinuous mass gain measurements (non-isothermal) were compared to those recorded after continuous chromium evaporation measurements (iso-thermal). The mass gains recorded are the sum of mass gained due to oxidation and mass lost due to Cr evaporation. Thus, measured mass gain does not indicate the true extent of oxidation and Cr consumption in the alloy. The mass gain should be compensated by the mass lost due to Cr evaporation (from Cr evaporation experiments) to determine the true extent of oxidation, called the 'corrected mass gain' (see paper VII).

5.3.2 Chromium evaporation measurements (Denuder technique)

The time-resolved in-situ Cr evaporation measurements were performed using the denuder technique. A denuder tube coated with Na_2CO_3 was placed at the outlet of the reactor, as shown in Figure 5.2. The downstream flow of the gas was directed through a denuder tube coated with Na_2CO_3. The volatile Cr species formed according to Equation (3.9) react with Na_2CO_3 as shown in Equation (5.1):

$$Na_2CO_3(s) + CrO_2(OH)_2(g) \rightarrow Na_2CrO_4(s) + H_2O(g) + CO_2(g) \tag{5.1}$$

The end of the denuder was connected to a wash bottle to collect any detached flakes of Na_2CrO_4. The denuders and wash bottles were replaced at regular intervals. The removed denuders and wash bottles were leached with deionised water. The Cr species were quantified with the Evolution 60s spectrophotometer (Thermo Scientific).

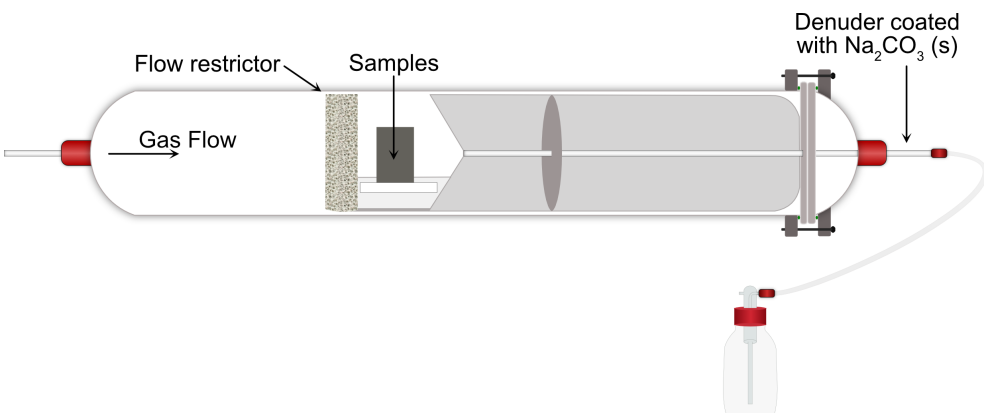

Figure 5.2: Schematic illustration of the experimental setup [150]

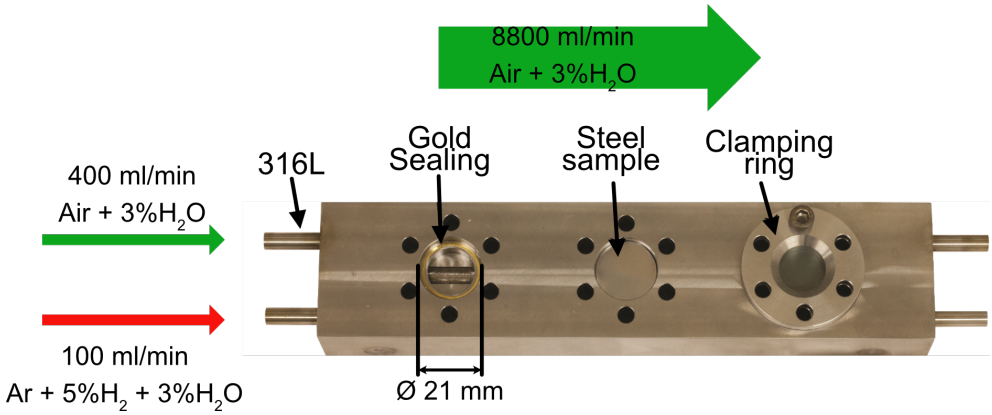

Figure 5.3: Schematic illustration of the dual-atmosphere setup.

5.3.3 Dual atmosphere exposures

The dual-atmosphere exposures were conducted using a custom-made sample holder, as shown in Figure 5.3. The design of this sample holder was based on previous work carried out at Montana State University, and additional information can be found elsewhere [139, 145]. The sample holder can accommodate up to six samples, with three coupons on each side. Gold rings are used to ensure gas tightness, which is tested before and after the exposure. The gas composition and flow rates are shown in Figure 5.3, and the gases were humidified in the same way as described earlier. The heating and cooling ramp for the dual-atmosphere exposures was set to 1 °C/min. Prior to the dual-atmosphere exposure, a pre-oxidation step was carried out in a tubular furnace at 800°C in air + 3% H_2O, with a low flow rate of 280 mL/min.

5.4 Samples preparation

5.4.1 Broad ion beam (BIB) milling

A BIB milling System Leica EM TIC 3X equipped with three Ar ion guns was used to polish the cross-sections of the coupons. A broad ion beam, typically of Ar ions, is used to bombard a target material, sputtering the atoms from the surface of the target. This milling process covers a wide area and yields finely polished cross-sections in the millimetre range for further analysis. The main advantages of using BIB over mechanical polishing are that it is a dry process and produces smoother surfaces, thereby revealing microstructural features.

5.5 Analytical Techniques

5.5.1 Spectrophotometry

Spectrophotometry is an analytical method used to quantify light-absorbing ions or molecules in a solution. Chemical compounds absorb light in a specific range of wavelengths, and the absorption of light increases with the concentration of the substance. The Beer-Lambert law [151] can be used to measure absorbance, as shown in Equation (5.2):

$$A = log_{10}\frac{I_0}{I} = \varepsilon_\lambda.c.l \tag{5.2}$$

where A is the absorbance, I_0 is the intensity of transmitted light for a given wavelength using pure solvent, I is the intensity of transmitted light through the solution, ε_λ is the molar absorptivity, l is the path length of the light through the solution, and c is the concentration. The maximum light absorbance for chromate ions in water solution is seen at a wavelength of 370 nm, so monochromatic light at this wavelength is used for all the concentration measurements. Fournier-Salaün et al. [152] have reported that a pH $\geq$ 9 and above is required for almost 100% chromate predominance in the solution. As such, solutions leached from denuders and wash bottles are pH tested and usually have a pH $>$ 9. In cases where the pH is lower, 0.1 M NaOH is added to the solution.

5.5.2 Scanning electron microscope

Scanning Electron Microscopy (SEM) is an electron microscope that produces high-resolution images by scanning the surface with a focused beam of electrons. As a result, SEM has a much higher resolution compared to optical microscopes, which use visible light. The electron source emits electrons, which are accelerated and passed through a system of magnetic lenses and apertures to produce a focused beam of electrons that hits the surface of the sample. The electrons interact with atoms in the material, producing various signals such as secondary electrons, Auger electrons, back-scattered electrons, and x-ray emissions. These emissions are transformed into signals that contain information about the topography, orientation, and composition of the material with the help of suitable detectors [153]. Figure 5.4 shows the interaction volume and different types of emissions from the electron-material interactions. The SEM used for the work in this thesis is a JEOL JSM-7800F Prime SEM equipped with an Oxford Instruments energy dispersive x-ray spectrometer (EDX).

Secondary Electrons Secondary Electron (SE) interact with the outermost surface of the material and are, therefore, highly surface sensitive. They are generated from the electron shells of atoms as a consequence of being excited by the electrons in the electron beam (Figure 5.4b). The secondary electrons usually have an energy of less than 50 eV [153]; therefore, they can escape from the outermost region of the sample, as shown in Figure 5.4a. As a result, they provide the best resolution for imaging and provide more topological information than the back-scattered electrons [154].

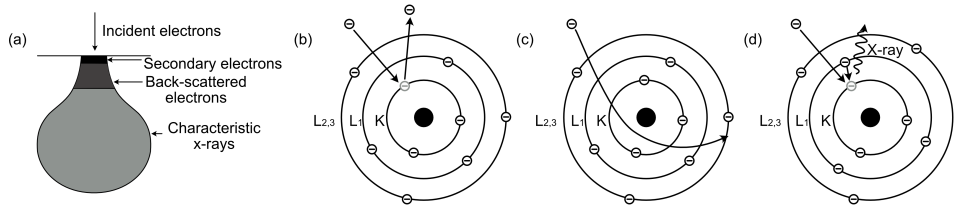

Figure 5.4: Schematic illustration showing the: (a) interaction volume, (b) secondary electrons, (c) back-scattered electrons, and (d) characteristic x-ray. Adapted from [153, 154]

Back-scattered Electrons The Back-scattered Electron (BSE) are highly energetic electrons that are produced when an electron from the electron beam is elastically scattered at the nucleus of an atom (Figure 5.4c). As they are highly energetic, their interaction volume is much larger than that of the secondary electrons (Figure 5.4a), resulting in reduced image resolution and topographic contrast. Nevertheless, they provide more information about the elements in the material. The higher the atomic number, the greater the number of incoming electrons that are back-scattered, resulting in so-called Z-contrast, which makes heavier elements appear brighter. [154].

Energy dispersive x-ray analysis Energy Dispersive X-ray Spectroscopy (EDX) analysis is used to obtain accurate information about the composition of the material. When an electron from the primary electron beam ejects an electron from the inner shell of an atom, the resulting void is filled by an electron from the outer shell with higher energy. The energy difference between the shells is emitted as an x-ray photon, as shown in Figure 5.4d. The energy difference between the shells is characteristic of the element. The emitted x-ray photons are measured with an x-ray spectrometer, to identify the elements in the material. Quantitative elemental information can be obtained using the intensity of an x-ray photon of specific energy. Since the x-rays are produced within the entire interaction volume, as shown in Figure 5.4a, the spatial resolution for the EDX analysis in SEM is in the order of micrometres [153].

5.5.3 Area-specific resistance

ASR measurements were performed ex-situ on the exposed coupons. To achieve a good electrical connection with the oxide layer, an area of 10 mm x 10 mm was sputtered with platinum for 10 minutes using the Quorum 150 sputter coater and a sputtering current of 60 mA. The sputtered area was further painted with platinum paste (Metalor 6926). In a box furnace, the samples were exposed to a temperature of 150°C for 15 minutes, and at the exposure temperature for 1 hour to remove all the binders from the platinum paste and to sinter the platinum paste (see Figure 5.5). The ASR was measured with a 4-point method in DC mode using platinum electrodes. An electrical current of 100 mA was used for the ASR measurements. The current was supplied by a Keithley 2400 source meter. To check the semiconducting behaviour, the ASR was measured as the coupon was cooled down. More details of the set-up can be found elsewhere [155]

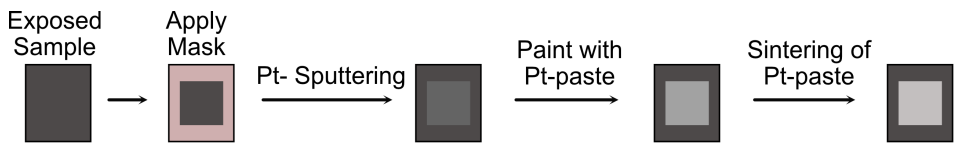

Figure 5.5: Schematic illustration of the step-wise electrode preparation process for ASR measurement.

6 Results and Discussion

This thesis presents the results of experimental investigations into the various metallic materials used in solid oxide fuel cells and electrolysers. The metallic materials used in SOC systems can be broadly categorised into two groups: (a) interconnect materials; and (b) BOP materials. Various FSS and coating-steel combinations are investigated for interconnect applications, while FSS are compared to other metallic materials for BOP applications. The metallic materials are mostly studied under high pO_2 conditions, while some experiments are performed under dual atmosphere conditions. The experiments include assessments of Cr evaporation behaviour, oxidation kinetics, and area-specific resistance measurements, followed by detailed material characterisations using SEM and EDX. The results provide an in-depth understanding of the behaviours of metallic materials that are potentially useful as interconnects and in BOP. Furthermore, potential strategies for mitigating high-temperature corrosion in such applications are explored. The findings systematically present the behaviours of various materials and coating-steel combinations. Improved coatings are proposed for SOEC interconnects, and potential avenues for future research are suggested.

6.1 Uncoated steels - Single atmosphere conditions

The uncoated steels, AISI 409, AISI 430, AISI 441, AISI 444 and Crofer 22 APU, were investigated in as-received condition for Cr evaporation behaviour, oxidation kinetics, and microstructural evolution in cross-section. The aim of this study was to understand the behaviour of uncoated steel as a function of temperature and steel composition. The compositions of these steels are listed in Table 5.1. The uncoated steels were exposed to air + 3% H_2O for 500 hours at temperatures that ranged from 750°C to 850°C.

6.1.1 Chromium evaporation

Figure 6.1 illustrates the cumulative Cr evaporation and the rates of Cr evaporation of uncoated AISI 441 and AISI 444 exposed to temperatures of 850°C, 800°C, and 750°C. The cumulative Cr evaporation of AISI 441 increased with an increase in temperature. The cumulative Cr evaporation at 850°C was approximately 2.5-fold higher than at 750°C. These results are consistent with those reported by Falk-Windisch et al. [119], who found that Cr evaporation of FSS with a similar oxide scale increased by a factor of 2-3 per 100°C within this temperature range. However, this was not the case for AISI 444, where the cumulative Cr evaporation was similar at 750°C, 800°C, and 850°C. The Cr evaporation of AISI 444 was similar to that of AISI 441 at 850°C. However, it was dissimilar at 750°C and 800°C. After 500 hours, the cumulative Cr evaporation was about 1.5-fold and 2.5-fold higher for AISI 444 than for AISI 441 at 800°C and 750°C, respectively.

The rate of Cr evaporation of AISI 441 initially decreased and stabilised within 168 hours at all the exposed temperatures. A similar trend was observed for AISI 444 at 850°C. The rate of Cr evaporation was similar for AISI 441 and AISI 444 at 850°C. However, at

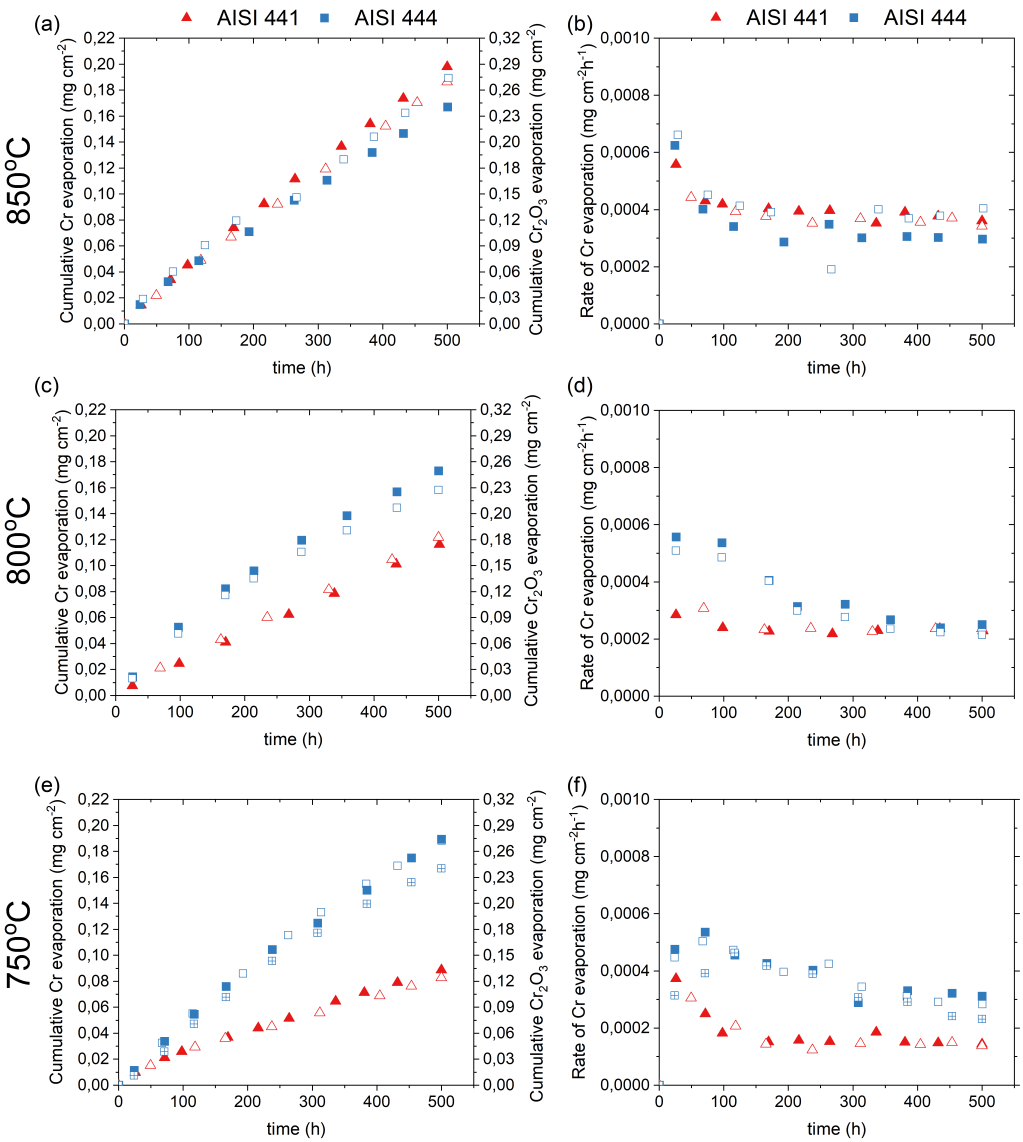

Figure 6.1: (a,c,e) Cumulative Cr evaporation and (b,d,f) rate of Cr evaporation as a function of time for the uncoated AISI 441 and AISI 444 exposed at 850°C, 800°C, 750°C for 500 hours in air + 3% H_2O. The open and filled symbols represent two individual exposures.

800°C, the rate of Cr evaporation of AISI 444 decreased slowly and was in a similar range to AISI 441 after 300 hours. At 750°C, the rate of Cr evaporation of AISI 444 decreased continuously, and was still 50% higher than that of AISI 441 after 500 hours. Although the cumulative Cr evaporation was similar for AISI 444 at 750°C and 850°C, the trend for the rate of Cr evaporation varied. The presence of Mn in the steel (see Table 5.1) resulted in the formation of $(Cr, Mn)_3O_4$ spinel on top of the Cr_2O_3 scale, which has been reported to reduce the Cr evaporation 2-3-fold compared to a Cr_2O_3 scale at 800°C [38, 51]. The decrease in the rate of Cr evaporation observed for the steels is attributed to the formation of $(Cr, Mn)_3O_4$ spinel. Despite the similar Mn contents of AISI 444 and AISI 441 (0.35 wt%), the slower drop in the rate of Cr evaporation seen for AISI 444 at 800°C and 750°C can be attributed to slower Mn transport to the oxide scale.

Nb is added to ferritic steels to stabilise the ferrite matrix and increase creep resistance. Nb precipitates as intermetallic Laves phase particles (type Fe_2Nb) along the grain boundaries, and this increases the creep resistance [55, 156, 157]. The Fe_2Nb phase incorporates some Si in the steel, hindering the formation of a resistive Si-rich oxide subscale at the metal-oxide interface. This has been reported to improve the electrical properties of the FSS [55, 56, 158]. The fraction of Laves phases is much higher in steels that contain Mo and Nb (AISI 444) than in steels that contain only Nb (AISI 441) [156]. The Laves phase precipitation in AISI 441 occurs mostly along the grain boundaries, while in AISI 444, it occurs along the grain boundaries and inside the grains. The high-volume fraction of Laves phase precipitates in AISI 444 might have affected Mn diffusion along the grain boundaries, which resulted in the high Cr evaporation observed at 750°C and 800°C. Ali-Löytty et al. [156] have shown that at 650°C, Laves phases formed at grain boundaries strongly limit Mn diffusion to the oxide scale. At 800°C, it took longer for AISI 444 to have a rate of Cr evaporation similar to that of AISI 441. In contrast, the Laves phase free steels, AISI 430 and Crofer 22 APU, had Cr evaporation lower than those of Laves phase containing steels, AISI 441 and AISI 444, after 500 hours (Figure 6.3). This is probably due to the faster formation of $(Cr, Mn)_3O_4$ spinel.

Falk-Windisch et al. [119] have compared the Cr evaporation of the Mo, Nb-containing steel Sanergy HT and the Nb-containing steel Crofer 22H. At 750°C, the rate of Cr evaporation for Sanergy HT was almost twice that for Crofer 22H. Moreover, the rate of Cr evaporation of Sanergy HT was similar at 750°C and 850°C, which matches the pattern observed for AISI 444. In addition, Crofer 22H, like AISI 441, showed a positive mass gain, while Sanergy HT, like AISI 444, showed a negative mass gain at 750°C after 500 hours (Figure 6.4a). The peculiar behaviours of Sanergy HT and AISI 444 could be due to the lack of a continuous $(Cr, Mn)_3O_4$ spinel.

To confirm the effect of Mn diffusion in Mo-, Nb-containing steels, AISI 444 exposed to 850°C for 168 hours was further exposed to 750°C. The rate of Cr evaporation of AISI 444 at 750°C, after being exposed to 850°C for 168 hours, was similar to that of AISI 441. This further confirms that the lack of a continuous $(Cr, Mn)_3O_4$ spinel causes the high Cr evaporation observed for AISI 444 at 750°C (Figure 6.1e, and f).

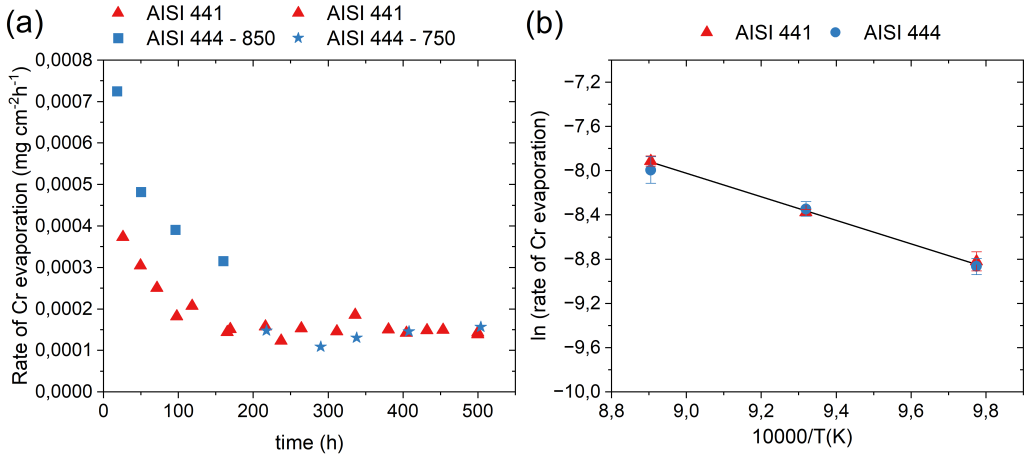

Figure 6.2: (a) Rate of Cr evaporation for the uncoated isothermal AISI 441, and discontinuous AISI 444 (AISI 444 initially exposed at 850°C for 168 hours), later exposed to 750°C for 500 h in air + 3% H_2O. The open and filled symbols represent two individual exposures. (b) Rate of Cr evaporation from Figures 6.1b,d, and f are represented in an Arrhenius plot.

To compare the effects of temperature on Cr evaporation, the activation energy for the rate of Cr evaporation was calculated using Equation (6.1)

$$ln(k) = \frac{-E_a}{RT} + ln(A) \tag{6.1}$$

where k is the rate constant of a chemical reaction (Cr evaporation), E_a is the activation energy, T is the absolute temperature (in K), R is the universal gas constant, and A is the exponential factor. The activation energy of the isothermally exposed samples of AISI 444 could not be calculated because of the differences in the oxide scale structure at 750°C. Thus, the rate of Cr evaporation from Figure 6.2a is used. Moreover, the data on the rate of Cr evaporation after the formation of $(Cr, Mn)_3O_4$ spinel (constant rate of Cr evaporation) is used in Figure 6.2b to calculate the activation energy. The activation energies of AISI 441 and AISI 444 for Cr evaporation were found to be 86 KJ mol^{-1} and 83 KJ mol^{-1}, respectively. The calculated activation energies are in good agreement with the activation energies for Cr evaporation of non-isothermally exposed Sanergy HT (91 KJ mol^{-1}) and Crofer 22H (92 KJ mol^{-1}) [119], as well as the theoretically calculated activation energy for Cr evaporation on a Cr_2O_3 scale (83 KJ mol^{-1}) [159].

The Cr evaporation behaviour of the uncoated steels AISI 409, AISI 430, AISI 441, AISI 444 and Crofer 22 APU exposed at 800°C are presented in Figure 6.3. All the steels showed dissimilar Cr evaporation, with AISI 444 showing the highest and Crofer 22 APU showing the lowest Cr evaporation. As discussed above, all the steels showed a decreasing rate of Cr evaporation, except for AISI 409. The steels with no Laves phases, AISI 430

and Crofer 22 APU, showed the lowest level of cumulative Cr evaporation, probably due to the faster formation of $(Cr, Mn)_3O_4$ spinel.

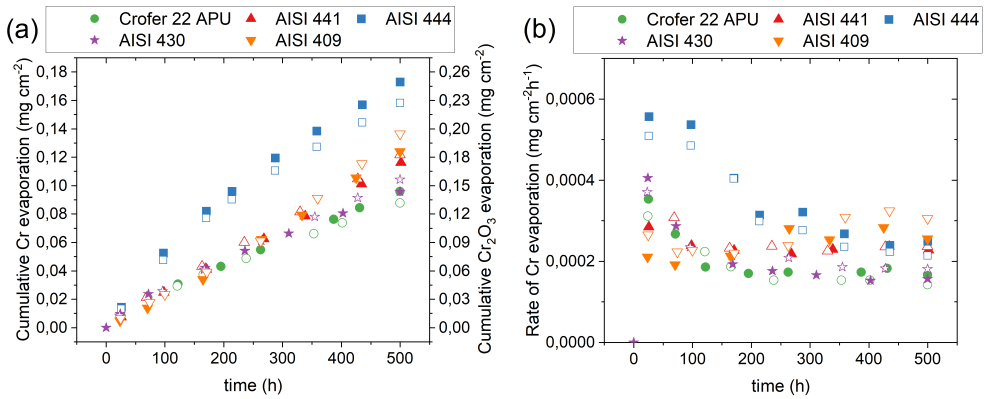

Figure 6.3: (a) Cumulative Cr evaporation and (b) rate of Cr evaporation as a function of time for the uncoated steels AISI 409, AISI 430, AISI 441, AISI 444 and Crofer 22 APU exposed to 800°C for 500 hours in air + 3% H_2O. The open and filled symbols represent two individual exposures.

6.1.2 Oxidation kinetics

Figure 6.4a shows the oxidation kinetics represented by the mass gains of AISI 441, and AISI 444 exposed to 750°C, and 850°C. Figure 6.4b shows the mass gains of various steels including AISI 441 and AISI 444 exposed to 800°C. The mass gains plotted in Figure 6.4 were measured during the exposure, and represent the sum of the mass gain due to oxidation and mass loss due to Cr evaporation. Due to oxide loss through Cr evaporation, the gravimetrically measured mass gain does not indicate the true extent of oxidation. Thus, the mass gain should be compensated with the mass loss due to Cr evaporation, to determine the true extent of oxidation, called the 'corrected mass gain' (see Paper VII).

At 850°C, AISI 441 and AISI 444 show significant differences in the mass gains. Similar differences in the oxidation behaviour of AISI 441 and AISI 444 have been reported in the literature [160]. Nevertheless, the reason for such differences in oxidation kinetics is unclear. AISI 444 showed a mass loss at 750°C, indicating paralinear oxidation kinetics. As discussed in Section 3.4, Cr evaporation significantly affects the oxidation behaviour. Since the mass loss through Cr evaporation is higher than the mass gain through oxidation, a mass loss is observed. On the other hand, AISI 441 showed a mass gain at 750°C. At 650°C, both AISI 441 and AISI 444 showed a mass loss (Figure 6.8.1b), following paralinear oxidation kinetics. As Cr evaporation has lower activation energy ($\approx$ 85 KJmol^{-1}) compared to oxide scale growth ($\approx$ 270 KJmol^{-1}) [119], Cr evaporation is less influenced by the decreasing temperature than the oxide scale growth.

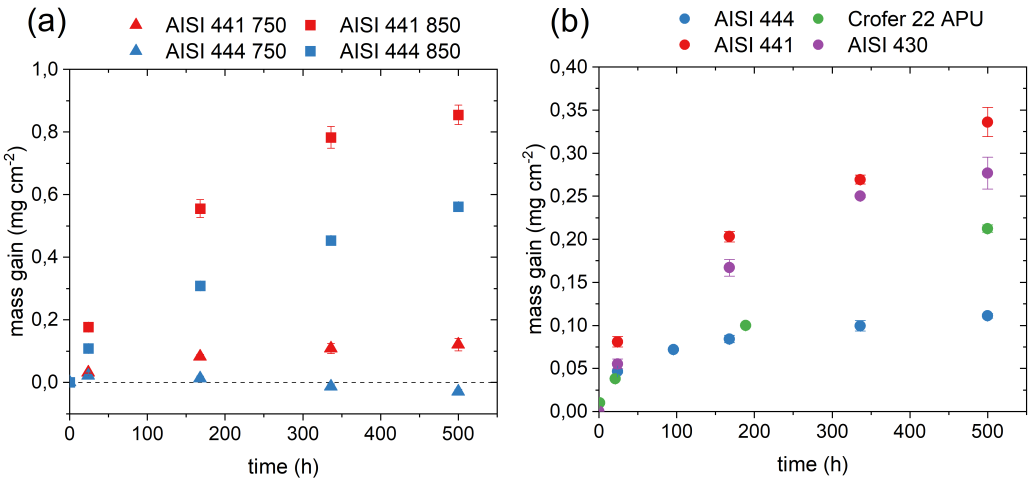

Figure 6.4: Mass gains of (a) AISI 441 and AISI 444 at 750°C and 850°C; and (b) AISI 409, AISI 430, AISI 441, AISI 444 and Crofer 22 APU exposed to 800°C for 500 hours in air + 3% H_2O.

The uncoated steels, AISI 430, AISI 441, AISI 444 and Crofer 22 APU, showed significant differences in mass gains, with AISI 444 showing the least mass gain, followed in increased order by Crofer 22 APU, AISI 430 and AISI 441. The differences in mass gains can be attributed to differences in the chemical compositions and Cr evaporation behaviours. Despite the lack of reactive elements, AISI 444 has a lower mass gain than Crofer 22 APU. However, the corrected mass gains (refer to Paper II) of Crofer 22 APU and AISI 444 are similar after 500 hours. The mass gain of AISI 409 is not presented owing to the occurrence of excessive spallation upon cooling. Nevertheless, the mass gain indicated that uncoated AISI 409 did not proceed to breakaway corrosion even after 500 hours despite having only 11.5 wt% Cr.

6.1.3 Microstructural evolution

Figure 6.5 shows the SEM micrographs and the corresponding EDX maps of the cross-sections of the uncoated steels, AISI 409, AISI 430, AISI 441, AISI 444 and Crofer 22 APU exposed at 800°C for 500 hours. All the uncoated steels showed a continuous oxide scale and no signs of spallation, except for AISI 409. AISI 409 had excessive spallation, yet a Cr-rich scale was found after 500 hours of exposure. All the steels displayed the formation of $(Cr, Mn)_3O_4$ spinel on the top and chromia scale beneath. The oxide scale thicknesses of the uncoated steels varied, following a trend similar to that observed for the mass gains (Figure 6.4b). Underneath the Cr_2O_3 scale, Ti internal oxidation was observed for AISI 441 and Crofer 22 APU. The presence of Nb in AISI 441, and of Nb and Mo in AISI 444 resulted in the Laves phase formation, which is observed as bright particles in the back-scattered electron (BSE) images. The fraction of Laves phases was higher for AISI 444 than for AISI 441.

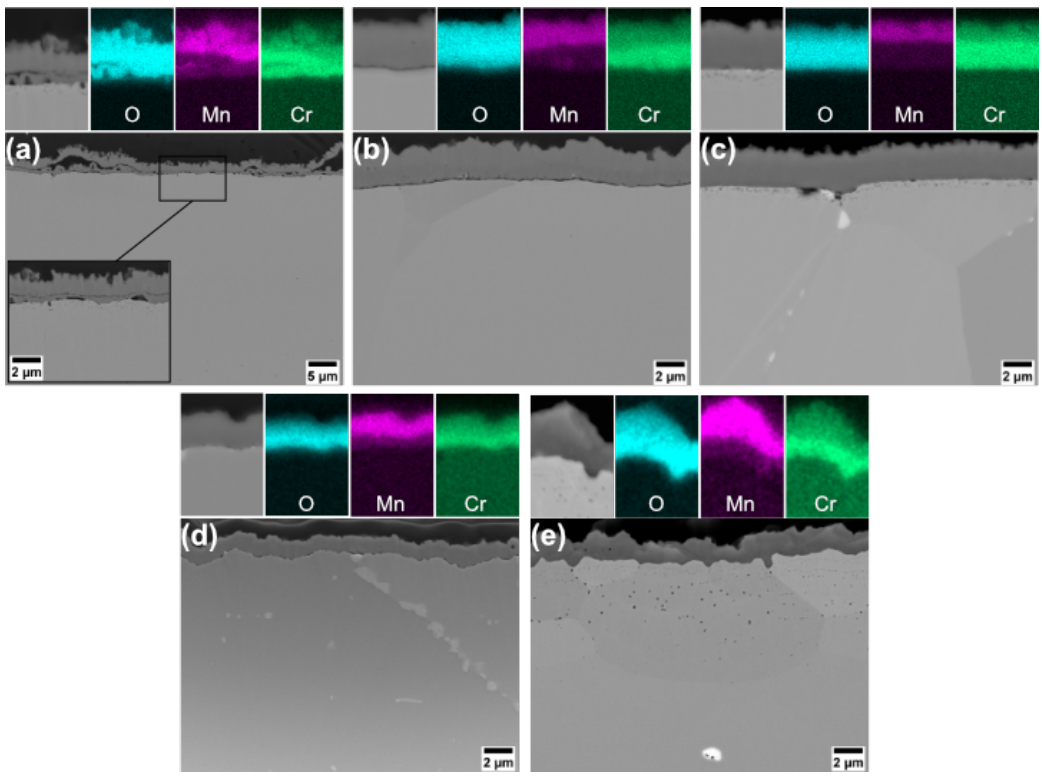

Figure 6.5: SEM micrographs and corresponding EDX maps of the BIB milled cross-section of the uncoated steels (a) AISI 409, (b) AISI 430, (c) AISI 441, (d) AISI 444 and (e) Crofer 22 APU at 800°C for 500 h in air + 3% H_2O.

6.2 Ce/Co-coated steels - Single atmosphere

The high levels of Cr evaporation and oxide scale growth exhibited by uncoated steels make them unsuitable for long-term operation in a SOFC stack. The most-effective way to improve the performance of the FSS is by applying protective coatings. Several protective coatings have been proposed for interconnect applications, as discussed in Section 4.1.2. The most commonly used coatings are based on MCO, which can be deposited using various techniques such as sol-gel deposition, APS, PVD, and EPD. Metallic Co is deposited using PVD, which upon oxidation at the operating temperature of the SOC transforms into Co_3O_4 in-situ [38, 95]. Co_3O_4 transforms to $(Co, Mn)_3O_4$ due to the outward diffusion of Mn from the steel [88, 99]. Furthermore, metallic coatings can be applied in roll-to-roll coating processes and subsequently shaped to interconnects, enabling high-volume production of the interconnects [90]. The cracks formed during the shaping process have been shown to self-heal during the exposure, forming a continuous, protective $(Co, Mn)_3O_4$ spinel [103, 161].

Foritzheim et al. [88] have demonstrated that a metallic Co coating can reduce Cr evaporation by an order of magnitude. However, the Cr evaporation measurements were performed on coupons with uncoated edges. Since the measured Cr evaporation includes contributions from the uncoated edges, it does not accurately reflect the true effectiveness of the Co coating. It has been shown that the addition of 10 nm Ce, a reactive element, to the Co coating significantly improves the oxidation resistance [95, 162]. As a result, Ce/Co coatings deposited using PVD are extensively studied for interconnect applications. As the protective coating is necessary to improve oxidation resistance and reduce Cr evaporation, it is important to compare the behaviours of Ce/Co-coated Crofer 22 APU and low-cost steels. Thus, the Ce/Co-coated steels, AISI 409, AISI 430, AISI 441, AISI 444 and Crofer 22 APU, were investigated for Cr evaporation behaviour, oxidation kinetics, microstructural evolution, and area-specific resistance.

6.2.1 Chromium evaporation

Influence of uncoated edges

Figure 6.6a shows the cumulative Cr evaporation of the Ce/Co-coated steels AISI 441, AISI 444 and Crofer 22 APU exposed to 800°C for 500 hours. The Cr evaporation of the Ce/Co-coated steels vary but are 10 times lower than those of the respective uncoated steels (Figure 6.3). These results are consistent with earlier published Cr evaporation data for Ce/Co coated steels [79, 88, 102, 103, 163, 164]. The Cr evaporation measurements were performed on coupons that were cut from Ce/Co-coated steel sheets (sheet-coated coupons), as shown in Figure 5.1a. As the sheet-coated coupons have uncoated edges, the Cr evaporation measured includes a contribution from these uncoated edges, which accounts for 3.6% of the total coupon area. Thus, the data shown in Figure 6.6a do not represent the true effectiveness of the Ce/Co coatings. The higher Cr evaporation of Ce/Co-coated AISI 444 compared to Ce/Co-coated AISI 441 and Crofer 22 APU may be due to the larger contribution to Cr evaporation from the uncoated edges of AISI 444.

To investigate the influence of the uncoated edges on Cr evaporation measurements, Ce/Co coatings were deposited on the pre-cut steel (see Figure 5.1b). Although PVD is a line-of-sight process, some coating material was found to be deposited on the edges of the precut-coated coupons, resulting in coupons with both coated faces and coated edges. Figure 6.6b shows the cumulative Cr evaporation of sheet-coated and precut-coated Crofer 22 APU exposed to 800°C for 500 hours. The precut-coated coupons exhibited about 6-fold lower Cr evaporation than the sheet-coated coupons after 500 hours. In addition, the pre-cut coated coupons demonstrated a consistent rate of Cr evaporation (see Paper I) throughout the exposure period. In contrast, the sheet-coated coupons exhibited a decrease in the rate of Cr evaporation over time, in similarity to the uncoated coupons.

To confirm this behaviour, the coating on all the edges of the precut-coated coupons was removed by carefully grounding the edges, referred to as 'precut-coated with all edges ground' in Figure 6.6b. The cumulative Cr evaporation of the precut-coated with all edges ground was similar to that of the sheet-coated coupons, confirming the effect of the uncoated edges. As expected, the precut-coated with only one edge (top edge) ground had a lower Cr evaporation than both the 'precut-coated with all edges ground' and sheet-coated coupons. Moreover, the rate of Cr evaporation decreased with time (see Paper I), in similarity to the sheet-coated and uncoated coupons, while it was constant for the pre-cut coated steels. These findings suggest that uncoated edges have a disproportionate impact, as compared with the area, on the Cr evaporation measurements of the sheet-coated coupons. It is speculated that the flow dynamics inside the reactor resulted in this behaviour.

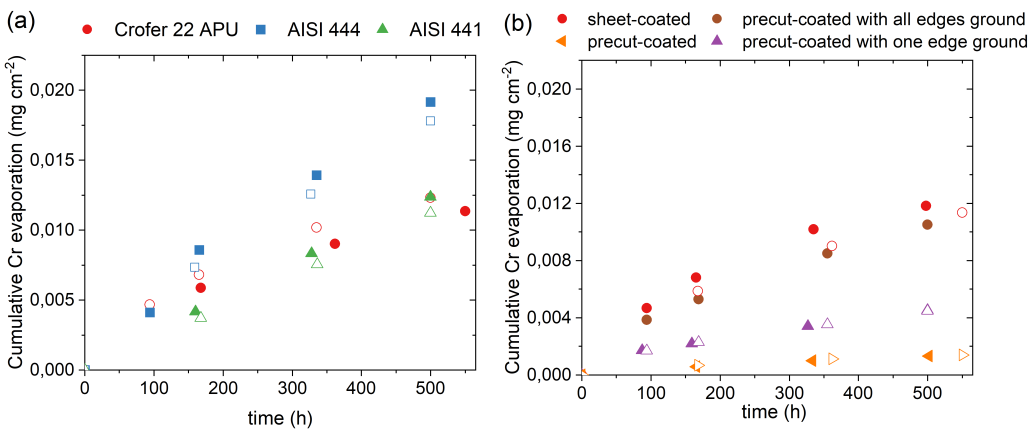

Figure 6.6: Cumulative Cr evaporation of (a) Ce/Co sheet-coated AISI 441, AISI 444 and Crofer 22 APU; and (b) Ce/Co precut-coated Crofer 22 APU, precut-coated coupons with ground edges and sheet-coated Crofer 22 APU exposed to 800°C for 500 h in air + 3% H_2O. The open and filled symbols represent two individual exposures.

Pre-cut coated steels

Since the uncoated edges were found to exert a significant influence, subsequent Cr evaporation measurements in this thesis were performed on pre-cut coated coupons, which have a coating on both the faces and edges. Figure 6.7a shows the cumulative Cr evaporation of Ce/Co-coated AISI 409, AISI 430, AISI 441, AISI 444, and Crofer 22 APU after 1,000 hours of exposure at 800°C in air + 3% H_2O. The Cr evaporation from the Ce/Co-coated steels was 60-100 times lower than that from the uncoated steels. In contrast to the differences observed for the sheet-coated coupons of AISI 441, AISI 444, and Crofer 22 APU (see Figure 6.6a), all the precut-coated steels exhibited similar Cr evaporation. The rate of Cr evaporation (Paper II) remained constant throughout the exposure, unlike the uncoated steels. Despite the slower Mn diffusion to the surface, Ce/Co-coated AISI 444 had a similar Cr evaporation compared with the other coated steels. In summary, various steels, once coated with Ce/Co, have extremely low and similar Cr evaporation. Moreover, the Cr evaporation at 750°C and 850°C (Figure 6.7b) were also significantly lower than those reported in the literature [79, 155, 161, 163]. Therefore, efforts to develop new steels must focus on improving oxidation resistance and ASR.

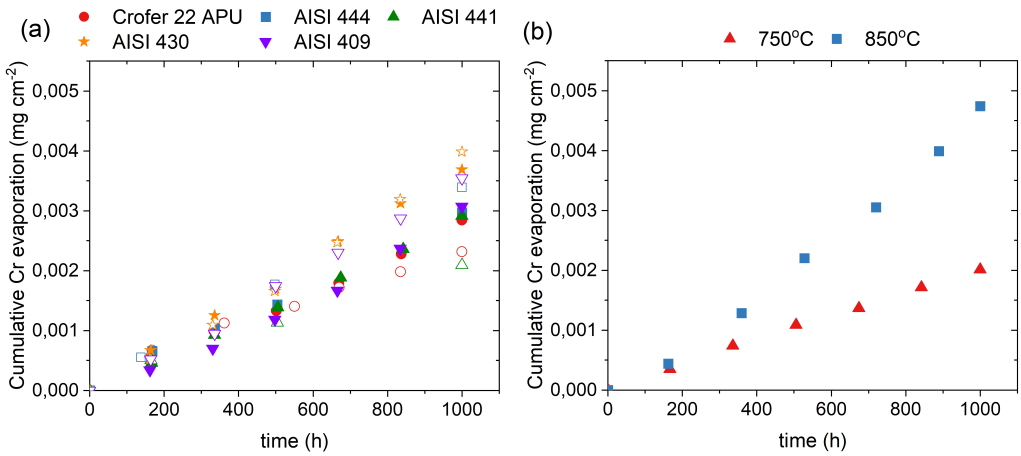

Figure 6.7: Cumulative Cr evaporation of Ce/Co-coated (a) AISI 409, AISI 430, AISI 441, AISI 444 and Crofer 22 APU exposed to 800°C; and (b) AISI 441 exposed to 750°C and 850°C in air + 3% H_2O, for 1,000 h. The open and filled symbols represent two individual exposures.

6.2.2 Oxidation kinetics

Figure 6.8 shows the mass gains of the Ce/Co-coated AISI 409, AISI 430, AISI 441, AISI 444, and Crofer 22 APU exposed to 800°C for 3,000 hours. All of the coated steels showed a rapid increase in mass gain during the first 2 hours due to the oxidation of the metallic Co coating to Co_3O_4. The coated steels exhibited an increase in mass over time, following

parabolic oxidation kinetics. Despite significant differences in the chemical compositions and oxidation kinetics of the uncoated steels, all the coated steels showed highly similar oxidation behaviours. Ce/Co-coated AISI 409, which contains only 11.4 wt% Cr, did not show signs of breakaway corrosion or oxide scale spallation during exposure for 3,000 hours, whereas the uncoated AISI 409 showed excessive spallation already after 168 hours. This is attributed to the reactive element, Ce, being deposited on AISI 409 as part of the coating, resulting in improved oxide scale adhesion. Highly similar oxidation behaviours were observed for various Ce/Co-coated steels at exposure temperatures in the range of 750°-900°C (Figure 6.18). The reason for these oxidation behaviours are discussed in Section 6.5.

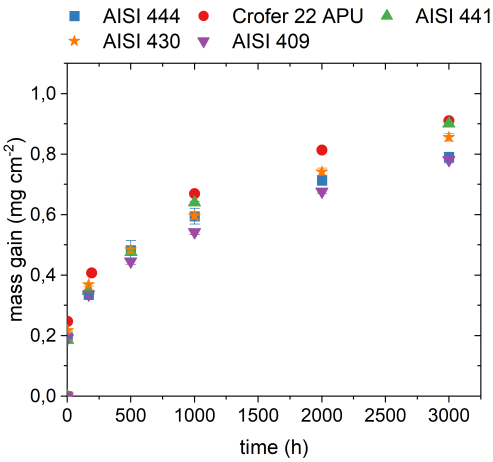

Figure 6.8: Mass gains of Ce/Co-coated AISI 409, AISI 430, AISI 441, AISI 444 and Crofer 22 APU exposed at 800°C for 3,000 h in air + 3% H_2O.

6.2.3 Microstructural evolution

Figure 6.9 presents the SEM micrographs and corresponding EDX maps of the cross-sections of Ce/Co-coated steels (AISI 409, AISI 430, AISI 441, AISI 444, and Crofer 22 APU), which were exposed to 800°C for 3,000 h. The coated steels exhibited a continuous oxide scale with no signs of spallation. The structures of the oxide scales were similar for all the coated steels, with $(Co, Mn)_3O_4$ on the top and Cr_2O_3 beneath. The thicknesses of the chromia scales on the coated steels were similar, which is consistent with the mass gains observed, as shown in Figure 6.8.

Compared to other coated steels, the chromia scale on Crofer 22 APU is undulating. This effect is likely due to the partly inward growth of the chromia scale, which is caused by the presence of the reactive element La. A significant difference was observed in the EDX Si map between the Ce/Co-coated low-cost steels (AISI 409, AISI 430, AISI 441, and AISI 444) and Crofer 22 APU. A Si-rich subscale was observed at the metal-oxide interface of the low-cost steels, but not for Crofer 22 APU, due to the lower Si content of

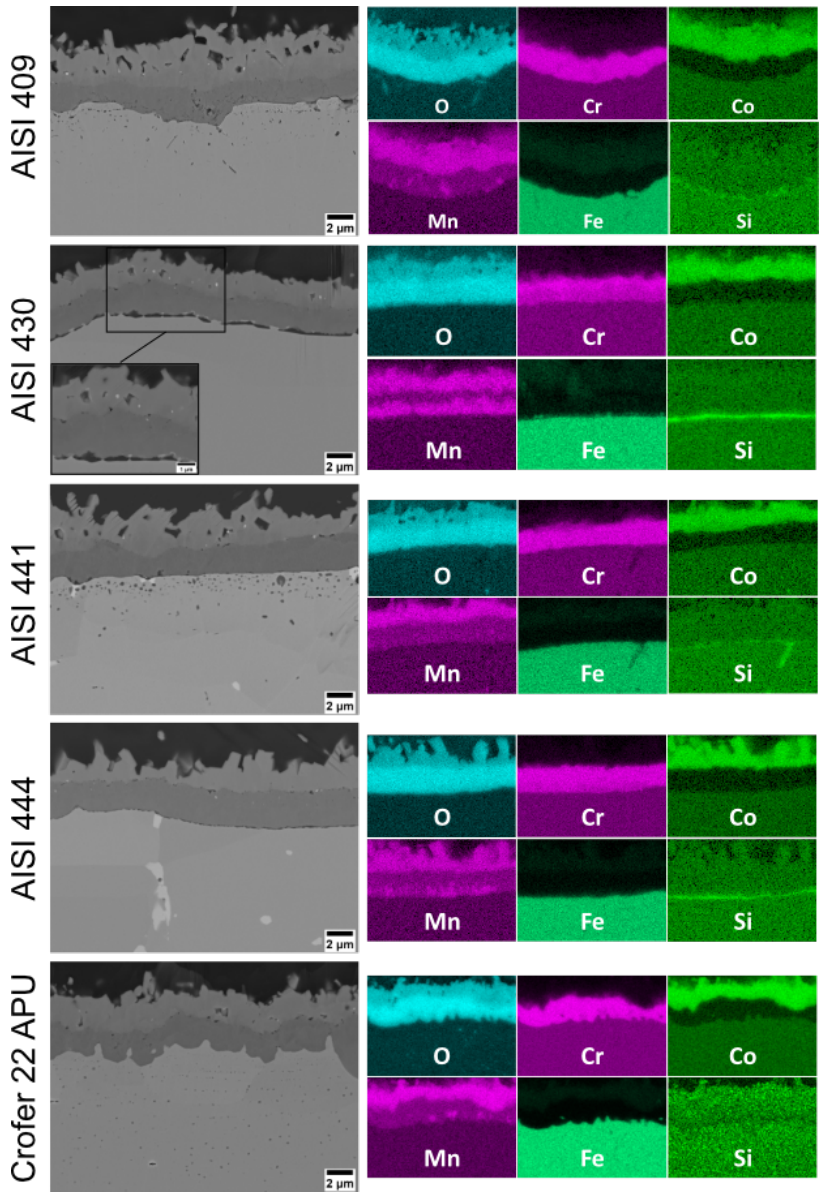

Figure 6.9: SEM micrographs and corresponding EDX maps of the BIB-milled cross-sections of the Ce/Co-coated steels AISI 409, AISI 430, AISI 441, AISI 444 and Crofer 22 APU exposed at 800°C for 3,000 h in air + 3% H_2O.

the alloy (0.01 wt% in Crofer 22 APU vs 0.34 wt% in AISI 430). This is because Crofer 22 APU undergoes a vacuum melting process to lower the Si content of the steel. The Si subscale appeared to be thicker on AISI 430, despite having a lower Si content than AISI 409, AISI 441 and AISI 444 (Table 5.1).

6.2.4 Area-specific resistance

Figure 6.10 shows the ex-situ ASR of the uncoated Crofer 22 APU, Ce/Co-coated AISI 409, AISI 430, AISI 441, AISI 444 and Crofer 22 APU exposed to 800°C for 3,000 h in air + 3% H_2O. The ASR values of the coated steels were significantly lower than the ASR values of the uncoated Crofer 22 APU after 3,000 hours. Moreover, the ASR values of the coated steels were highly similar, with the exception of the Ce/Co-coated AISI 430, which showed a higher ASR, of about 50 mohm cm^2. The other coated steels showed ASR values in the range of 18-23 mohm cm^2. The ASR increased with decreasing temperature, indicating the semi-conducting behaviour of the oxide scale.

Si-rich oxide scales are highly resistive [165] and are reported to increase the ASR and degrade the performance of the SOFC. The Si subscale formed on low-cost steels, other than AISI 430, did not result in ASR values higher than that of Crofer 22 APU. This might be because the Si-rich oxide scale is not continuous. The Laves phases in AISI 441 and AISI 444 are known to bind Si, preventing the formation of a continuous Si oxide layer. The lack of Laves phases in AISI 430 might have resulted in a pronounced Si-rich subscale, resulting in a higher ASR.

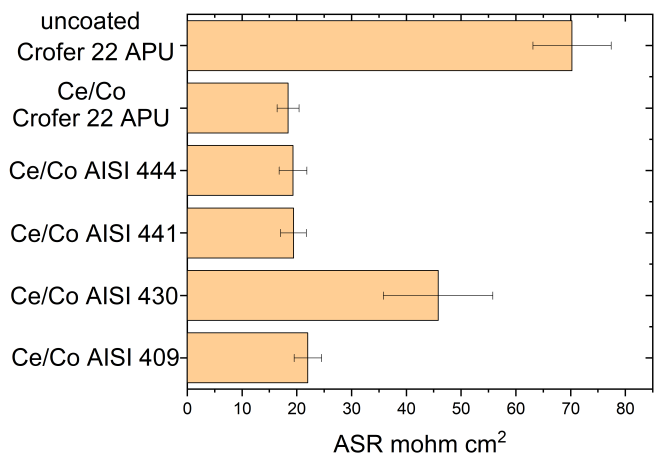

Figure 6.10: Ex-situ ASR values of uncoated Crofer 22 APU and Ce/Co-coated AISI 409, AISI 430, AISI 441, AISI 444 and Crofer 22 APU exposed at 800°C for 3,000 h in air + 3% H_2O.

6.3 Ce/Co-coated steel: Dual-atmosphere

The experiments conducted in a single atmosphere do not fully reflect the real-world conditions experienced by an interconnect in a SOC stack. In the stack, the interconnect is exposed to high-pO_2 (air) conditions on one side and low-pO_2 (fuel) conditions on the other. In the context of SOFCs, several studies [138, 141, 143–145, 148] have reported differences in the air side oxide scale formed when FSS interconnects are exposed to hydrogen and air on either side, as compared to when they are exposed to air only. Some authors [144] have reported only minor changes in the oxide scale composition, while others [138, 143] have shown more severe effects with a significant change in the oxide scale thickness, often leading to breakaway corrosion. This phenomenon, known as the 'dual-atmosphere effect', is believed to be caused by the interference of hydrogen with the oxidation process on the air side of the sample. The exact mechanism behind the dual-atmosphere effect is highly debated, and various suggested mechanisms are discussed in Section 4.1.5.

To replace the expensive tailor-made Crofer 22 APU with low-cost steels such as AISI 444 or AISI 441, it is important to understand the behaviours of these steels under dual-atmosphere conditions. The performance of Ce/Co-coated low-cost FSS was similar to that of Ce/Co-coated Crofer 22 APU under single-atmosphere conditions, as reported in Section 6.2. It is important to examine the effect of the air side Ce/Co coating under dual-atmosphere conditions and to compare Ce/Co-coated low-cost steels to Crofer 22 APU. Thus, uncoated and air side Ce/Co-coated steels, including AISI 441, AISI 444, and Crofer 22 APU, were exposed to dual-atmosphere conditions with air + 3% H_2O and Ar + 5% H_2 + 3% H_2O on either side at 800°C.

Figure 6.11 shows the SEM micrographs of the cross-sections of the air side and fuel side oxide scales on uncoated and Ce/Co-coated coupons exposed to dual-atmosphere conditions for 336 hours at 800°C. Both Ce/Co-coated and uncoated steels exhibited a continuous oxide scale on the air side and fuel side, without any signs of spallation. The surface view and the Cr-rich oxide scale (see Paper III) on the air side and fuel side indicate the presence of a protective oxide scale with no signs of breakaway corrosion. Although some researchers [138, 143] have reported breakaway corrosion on uncoated steels exposed at 800°C, this was not observed in this particular case. This is likely due to the pre-oxidation of the samples at 800°C in air for 20 minutes before the exposure. This pre-oxidation step is important for simulating the conditions that interconnects experience in stacks, which must be conditioned at temperatures higher than the operating temperatures to ensure gas tightness.

The uncoated steels exposed to the dual-atmosphere showed the formation of $(Cr, Mn)_3O_4$ spinel on the top and Cr_2O_3 scale underneath on the air side, resembling the oxide scale structure observed in the single atmosphere (Figure 6.5). The uncoated steels showed differences in oxide scale thickness between the different steel grades. The Ce/Co-coated steels formed $(Co, Mn)_3O_4$ spinel on the top and Cr_2O_3 scale beneath, similar to the

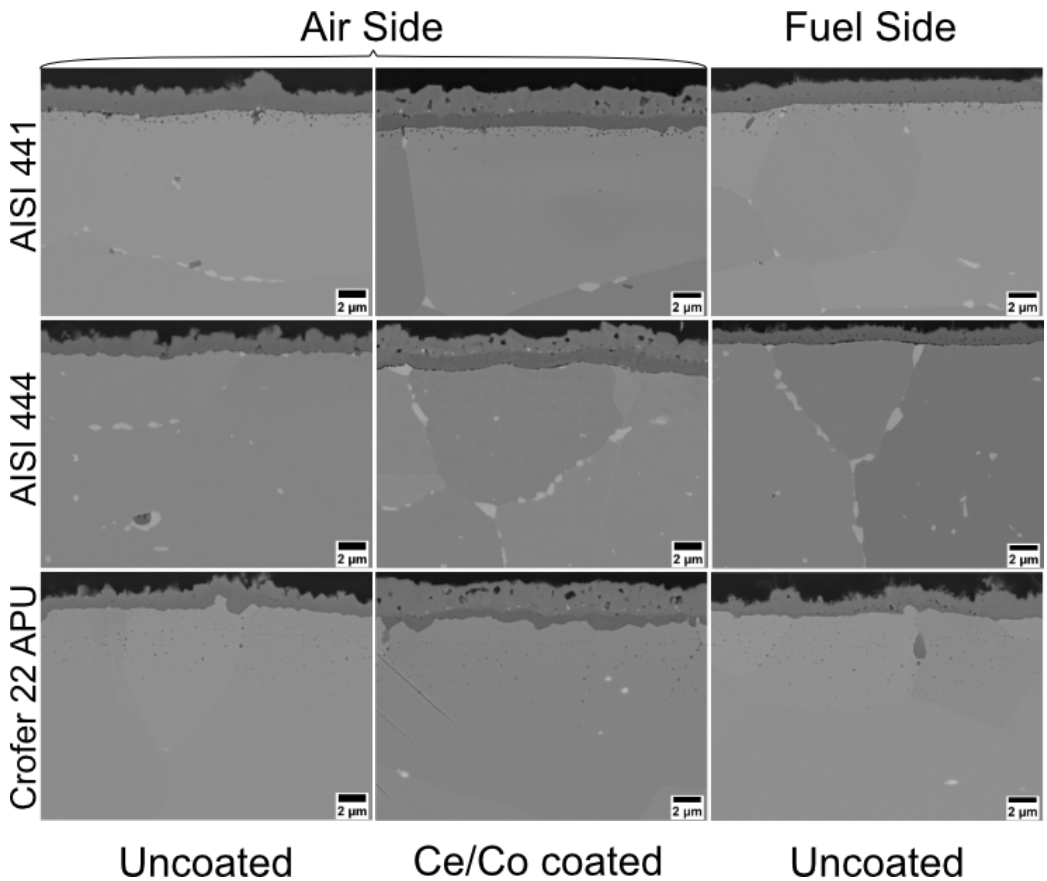

Figure 6.11: SEM micrographs of the BIB-milled cross-sections of the uncoated air side, uncoated fuel side, and the air side of Ce/Co-coated AISI 441, AISI 444 and Crofer 22 APU exposed under dual-atmosphere conditions at 800°C for 336 h.

oxide scale structure observed after 3,000 hours in the single atmosphere (Figure 6.9). Different Ce/Co-coated steels showed similar thicknesses of the oxide scale on the air side, indicating similar oxidation kinetics, as noted also under single atmosphere conditions (Figure 6.8).

On the fuel side (which was uncoated in both cases), the oxide layer had $(Cr, Mn)_3O_4$ spinel on top and a Cr_2O_3 scale beneath. The oxide scale thickness and structure on the fuel side were found to be similar to those on the air side, as also reported by other researchers [166]. On the Ce/Co-coated steels, the Cr-rich scale on the air side (Cr_2O_3) was thinner than that on the fuel side (Cr_2O_3 + $(Cr, Mn)_3O_4$). This indicates that Cr consumption is lower on the air side in the presence of the Ce/Co-coating, indicating a potential need for coating on the fuel side to reduce Cr scale growth.

6.4 Ce/Co coating: Benchmarking against other coatings

As discussed in Section 4.1.2, MCO coatings can be deposited using various methods, including APS, spray pyrolysis, PVD, and EPD. The coatings deposited using various methods were extensively evaluated [79, 89]. Few studies have compared the same coating deposited on different substrates [99, 167, 168] or compared the same coating deposited using different techniques [169, 170]. Comparisons of coatings deposited using different methods in terms of Cr evaporation, oxidation resistance, and area-specific resistance under similar conditions have rarely been performed. The MCO coatings deposited using other techniques are usually thicker, so it is important to compare the PVD-deposited Ce/Co coatings to other MCO coatings. In the following section, MCO-based coatings deposited through APS, spray pyrolysis, and sol-gel ultrasonic spraying are compared to PVD-deposited Ce/Co coatings. Uncoated Crofer 22 APU and coated Crofer 22 APU are compared in terms of their Cr evaporation behaviours, oxidation kinetics, and area-specific resistances for up to 3,000 hours at 800°C in air + 3% H_2O atmosphere. The coatings compared are a subset of the coatings compared in paper IV. To facilitate easier comparisons with other coatings, the PVD-deposited Ce/Co coating will be referred to as 'CeCoPVD coating' in this section.

6.4.1 Coatings

Table 6.1 provides detailed information regarding the coating, including the compositions, thicknesses, and heat treatments prior to exposure. The CeCoPVD coating is metallic, while the MCFAPS coating is partially oxidised, and the MCOCeUSC and MCOCeSP coatings are completely oxidised. The CeCoPVD, MCOCeSP, and MCOCeUSC coatings contained varying amounts of the reactive element Ce, while no reactive elements were present in the MCFAPS coating. The MCOCeUSC coating was pre-treated in reducing (H_2) and oxidising atmospheres prior to exposure, to produce denser coatings [171], while the other coatings were not pre-treated. The MCOCeSP coating was exposed to 800°C for 30 minutes to burn off the binder from the coating. More information on the coating deposition technique and parameters can be found in the references provided in Table 6.1.

The SEM micrographs of the as-received coatings are shown in Figure 6.13. The thicknesses of the coatings in Table 6.1 were determined from the SEM micrographs of the as-received coatings. The coating thicknesses varied from 0.6 ± 0.1 μm to 93 ± 7 μm. One significant difference between the as-received coatings was the presence of chromia scale at the steel-coating interface of the MCOCeUSC-coated steel. The chromia scale was formed during the pre-treatment of the coated steel. The MCOCeSP and MCOPVD coatings appeared to be dense, while porosity was observed in the MCOCeUSC and MCFAPS coatings. In the MCOCeUSC coating, the coating appeared to be dense at the coating-chromia interface and was more porous towards the air-coating interface.

Table 6.1: Specifications of the investigated coatings.

Coating	CeCoPVD	MCOCeSP	MCOCeUSC	MCFAPS
Composition	10 nm Ce 600 nm Co	MCO + 5%CeO	$(Mn, Co)_{2.98}O_{2.98}$ + 0.02CeO	$(Mn, Co, Fe)_3O_4$ (MCF)
Thickness (μm)	0.6 ± 0.1	3.3 ± 0.8	5.2 ± 0.7	93 ± 7
Coating deposition method	Physical vapour deposition	Spray pyrolysis (SP)	Sol-gel ultrasonic spray coating (USC)	Atmospheric plasma spraying (APS)
Pre-treatment	-	800°C, 30 mins (Binder burn-off)	Reduction: 5 h, 850°C, H_2; Oxidation: 1 h, 1,000°C, air	-
References	[79, 88]	[172, 173]	[174]	[175–177]

6.4.2 Chromium evaporation

Figure 6.12a shows the cumulative Cr evaporation of Crofer 22 APU, both uncoated and coated with CeCoPVD, MCOCeSP, MCOCeUSC, and MCFAPS, exposed to 800°C for 500 hours. As anticipated, the uncoated steel exhibited the highest Cr evaporation. All the coated steels exhibited significantly lower Cr evaporation than the uncoated steel (at least 60-times lower). The MCFAPS coating, with a thickness of 93 ± 7 μm, exhibited the lowest Cr evaporation, about 100-times lower than that of the uncoated steel. The other coated steels, with thicknesses in the range of 1-6 μm, showed similar Cr evaporation to the MCFAPS-coated steel, indicating the effectiveness of $(Co, Mn)_3O_4$ spinel in mitigating Cr evaporation.

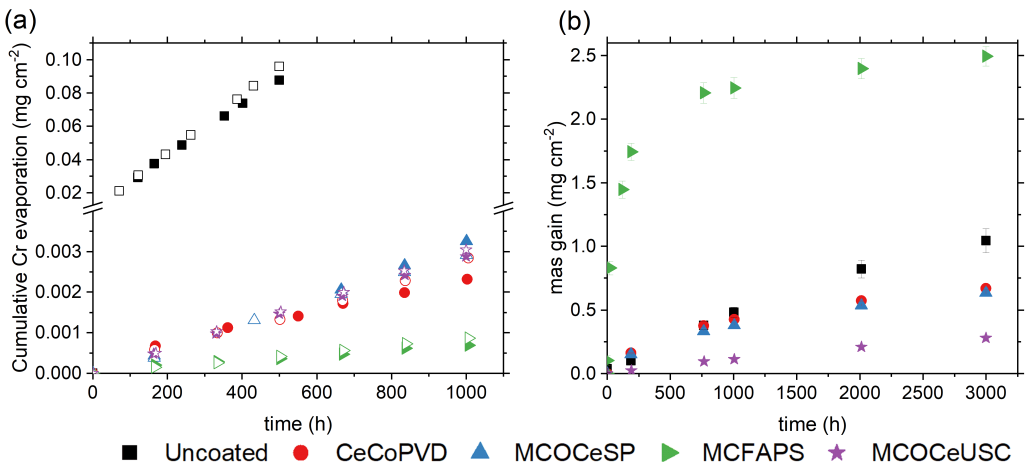

Figure 6.12: (a) Cumulative Cr evaporation and (b) mass gains of uncoated, CeCoPVD-, MCOCeSP-, MCOCeUSC-, MCFAPS-coated Crofer 22 APU exposed at 800°C for up to 3,000 h in air + 3% H_2O.

6.4.3 Oxidation kinetics

Figure 6.12b shows the mass gains of the uncoated, and CeCoPVD-, MCOCeSP-, MCOCeUSC-, MCFAPS-coated Crofer 22 APU exposed at 800°C for 3,000 hours. Since the CeCoPVD and MCFAPS coatings were not completely oxidised, the mass gain due to coating oxidation after 1 hour at 800°C was removed (0.93 mg.cm^{-2} - MCFAPS; 0.24 mg.cm^{-2} - CeCoPVD) on subsequent data points before plotting Figure 6.12b. The CeCoPVD coating was completely oxidised during the 1-hour exposure at 800°C; however, this was not the case for the MCFAPS coating. Upon further exposure, a steep increase in the mass of the MCFAPS coating was observed. Based on the mass gain data, it appears that the MCFAPS coating was not completely oxidised before 200 hours of exposure. Thus, MCFAPS had the highest mass gain of 2.49 ± 0.07 mg.cm^{-2} after 3,000 hours. The MCOCeSP- and CeCoPVD-coated steels had similar mass gains after 3,000 hours, but these were substantially lower than the mass gain of the uncoated steel.

MCOCeUSC-coated steel, which had a slightly thicker coating (5 μm) than the MCOCeSP (2.2 μm) and CeCoPVD (1 μm after oxidation) coatings, and which contained additions of the same reactive element (Ce), albeit with different amounts, showed a substantially lower mass gain. The mass gain of the MCOCeUSC-coated steel after 3,000 hours was 0.24 ± 0.01 mg.cm^{-2} while the mass gains of the MCOCeSP- and CeCoPVD-coated steels were 0.63 ± 0.01 mg.cm^{-2} and 0.66 ± 0.01 mg.cm^{-2}, respectively. The main difference between the MCOCeUSC-coated steel to MCOCeSP-coated and CeCoPVD-coated steels was the pre-treatment step after coating deposition. The pre-treatment for the MCOCeUSC-coated steel was performed in H_2 for 5 hours at 850°C and 1 hour in air at 1,000 °C. This pre-treatment resulted in the chromia scale formation seen in Figure 6.13i. Thus, the mass gain measured for the MCOCeUSC-coated steel does not reflect the thickness of the chromia scale after the exposure (Figure 6.13j).

6.4.4 Microstructural characterisation

Figure 6.13a, and b shows the SEM micrographs and EDX maps of uncoated Crofer 22 APU exposed for 3,000h at 800°C. Two distinct layers were observed in the oxide scale, which were identified as $(Cr, Mn)_3O_4$ on the top and Cr_2O_3 beneath, as discussed in earlier sections. The thickness of the Cr-rich oxide scale after 3,000 hours was 8.7 ± 0.5 μm. The oxide scale on the coated steels was multilayered, with the coating on the top and the chromia scale beneath. Along with the thickness of the coating, the Cr_2O_3 scale thickness differed between the coated steels. In the oxide scales of the CeCoPVD-, MCOCeSP-, and MCFAPS-coated steels, a distinct Cr-rich oxide layer was observed. However, in the case of MCOCeUSC, a part of the coating enriched with Cr (mixed layer of the coating and the chromia scale) was observed at the chromia-coating interface. This is probably due to pre-oxidation at high temperatures (1,000°C) before the exposure. The presence of a Cr-enriched coating at the chromia-coating interface has been reported previously [178, 179].

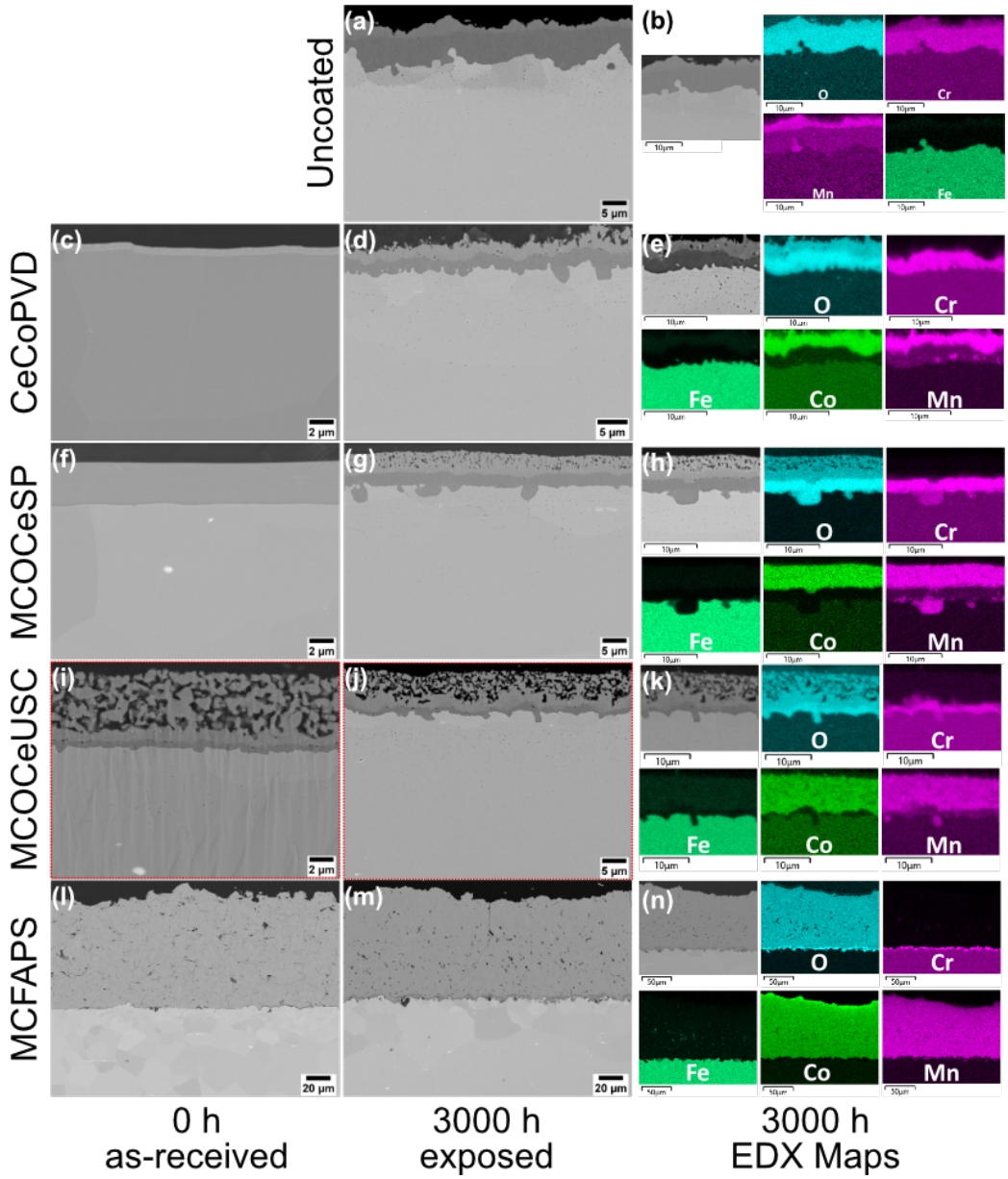

Figure 6.13: SEM micrographs of the cross-sections of (c,f,i,l) as-received CeCoPVD-, MCOCeSP-, MCOCeUSC-, and MCFAPS-coated Crofer 22 APU. (a,d,g,j,m) SEM micrographs of the cross-sections (b,e,h,k,n) and EDX maps of the corresponding cross-sections of the uncoated, and CeCoPVD-, MCOCeSP-, MCOCeUSC-, and MCFAPS-coated Crofer 22 APU steels exposed for 3,000 hours at 800°C in air + 3% H_2O.

The mass gains observed in Figure 6.12b do not correlate to the Cr-rich oxide scale thicknesses of the uncoated, MCFAPS- and MCOCeUSC-coated Crofer 22 APU. For the uncoated steel, the significant Cr evaporation observed (see Figure 6.12a) influenced the mass gain and the thickness of the Cr-rich oxide scale. In the case of MCFAPS, the coating oxidation resulted in a very high mass gain, as seen in Figure 6.12b; however, the chromia scale thickness was similar to those observed for the MCOCeSP- and CeCoPVD-coated steels. For detailed information on the Cr-rich oxide scale thickness, refer to paper IV. The MCOCeUSC-coated steel had a chromia scale prior to the exposure, so the mass gain measured does not correlate with the measured thickness of the Cr-rich oxide scale.

The Cr-rich scale was thickest on the uncoated steel and thinnest on the MCOCeUSC-coated steel. Although the MCOCeUSC-coated steel had the thickest chromia scale before exposure (Figure 6.13i), it had the thinnest Cr-rich scale after exposure at 800°C for 3,000 hours. It appears that pre-oxidation significantly improved the oxidation resistance of the MCOCeUSC-coated steel. This effect may be due to a higher level of purity of the Cr_2O_3 scale or the formation of coarser-grained Cr_2O_3 at higher temperatures, which resulted in slower oxidation kinetics. The Cr-rich oxide scale on the MCOCeUSC-coated steel after the exposure was estimated to be 30-40% thinner than the Cr-rich scales on the CeCoPVD-, MCOCeSP-, and MCFAPS-coated steels.

The presence of a reactive element, Ce, significantly lowered the oxidation kinetics in the CeCoPVD- and MCOCeSP-coated steels compared to the uncoated steel. The concentration of reactive elements in the MCOCeSP coating was 5% compared to 1.6% in the CeCoPVD coating. Moreover, the MCOCeSP coating was 3-times thicker than the CeCoPVD coating, indicating a much higher reactive element content in the former coating. Nevertheless, the Cr-rich oxide scale on the CeCoPVD-coated steel was similar to that on the MCOCeSP-coated steel, despite the significant differences in coating thickness and reactive element content. These results are consistent with those described in Section 6.5.1.

The CeCoPVD and MCOCeSP coatings, which showed no porosity in the as-received form, did exhibit porosity after 3,000 hours of exposure. Some porosity was observed on the CeCoPVD, with it being spread throughout the coating. In contrast, the MCOCeSP and MCOCeUSC coatings were more porous, with the porosity located mostly towards the coating-air interface. Thus, the Cr evaporation of these coated steels was extremely low. In MCFAPS-coated steel, the cracks in the as-received coating were closed due to the coating oxidation and volume expansion, although some porosity was observed after 3,000 hours.

6.4.5 Area-specific resistance

Figure 6.14 shows the ex-situ area-specific resistances of the uncoated and coated steels that were exposed for 3,000 hours at 800°C. The uncoated and coated steels showed increased ASR with decreasing temperature, indicating the semiconductive behaviour of the oxide scale. All the coated steels had significantly lower ASR values than the

corresponding uncoated steel. This matches well with the observed Cr-rich oxide scale thicknesses depicted in Figure 6.13. MCFAPS-coated steel, with a 93 μm thick coating, and CeCoPVD coating, with a 1 μm thick coating, exhibit similar ASR values. This is likely due to similar chromia scale thicknesses on the MCFAPS- and CeCoPVD-coated steels. These results agree with the earlier work by Goebel et al. [136], who showed that the ASR of a coated steel is determined by the Cr-rich oxide scale rather than the coating thickness or coating conductivity. MCOCeUSC-coated steel, which has the thinnest Cr-rich oxide scale, showed the lowest ASR, albeit in a similar range to the other coated steels.

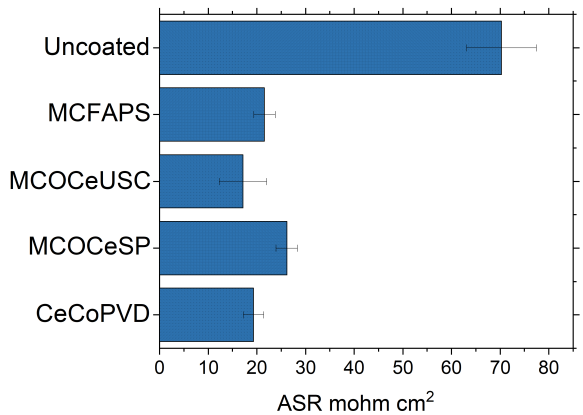

Figure 6.14: Ex-situ ASR values for uncoated, and CeCoPVD-, MCOCeSP-, MCOCeUSC-, MCFAPS-coated Crofer 22 APU exposed at 800°C for 3,000 h in air + 3% H_2O.

6.5 The role of Ce in the Ce/Co coating

The reactive element effect (REE) and various mechanisms proposed in the literature to explain the REE were presented in Section 4.1.1.1. Adding small amounts of reactive elements to the FSS significantly improves their oxidation resistance and oxide scale adhesion. As a result, these elements are incorporated into steel grades that are designed for high-temperature applications, including steels designed for interconnects, such as Crofer 22 APU, Crofer 22H, ZMG232, and SanergyHT. Since protective coatings are essential for interconnects, various researchers have devised coatings that contain reactive elements. Fontana et al. [91] have demonstrated that adding a 100-200 nm thick reactive element coating to Crofer 22 APU reduces oxide scale growth and enhances oxide scale adhesion. Similarly, Grolig et al. [79] have demonstrated that adding a 600 nm thick layer of Ce or La to AISI 441 reduces the chromia scale growth and improves its adhesion, albeit without any significant effect on Cr evaporation. It is crucial to develop coatings that can effectively improve oxidation performance and oxide scale adhesion while also reducing Cr evaporation.

Froitzheim et al. [88] and Stanislowski et al. [38] have demonstrated that Co coatings are highly effective at inhibiting Cr evaporation. Canovic et al. [95] have shown that the addition of Ce to Co coatings significantly reduces the chromia scale growth, and this has been confirmed by other researchers [94, 97, 162]. Ce added to Co coatings not only reduced the chromia scale growth but also significantly lowered the Cr evaporation, as shown in Section 6.2. Similar improvements achieved by the addition of reactive elements to MCO coatings have been reported by other researchers [96, 98].

While the impact of Ce in Ce/Co coatings is evident, the mechanism underlying this effect remains poorly understood. Goebel et al. [102] have demonstrated the suitability of Ce/Co coatings by studying them for 38,000 hours of exposure at 800°C. Nonetheless, the authors have suggested that higher concentrations of REs may be more optimal for prolonged operation. To design coatings that meet the necessary lifetime targets for SOC interconnects, it is essential to understand the REE mechanism in the presence of Ce/Co coatings. Here, the influence of reactive element concentration in Ce/Co coatings is studied. Efforts are made to understand the mechanism behind the improved behaviour observed upon Ce addition to Co coatings.

6.5.1 Influence of Ce thickness in the Ce/Co coating

Based on the results shown in Figures 6.13a, and d, 10 nm of Ce in the Ce/Co coating significantly reduced the chromia scale growth on Crofer 22 APU. It is reasonable to assume that increasing the thickness of the Ce coating will lead to further enhancement of the oxidation behaviour for the substrate. It is commonly accepted that the REE is due to doping of the chromia scale by the reactive element (in this case, Ce). As the thickness of the oxide scale increases, the reactive element doping per unit volume of the chromia scale decreases, which might affect the oxidation behaviour in the long term. To enhance further the REE, coatings with a thicker Ce layer were deposited onto AISI 441,

as shown in Table 5.4. Contrary to expectations, the mass gains of the AISI 441 coated with different thicknesses of Ce in Ce/Co coating (Figure 6.15) were similar until 6,000 hours of exposure; however, they were lower than the mass gain of the uncoated steel. This result can be interpreted in several ways: (i) that 10 nm is a sufficient thickness for the reactive element layer; (ii) that the beneficial effect provided by reactive element thickness occurs at even longer exposure times; and (iii) that the mechanism behind the Ce effect is different from what is commonly accepted.

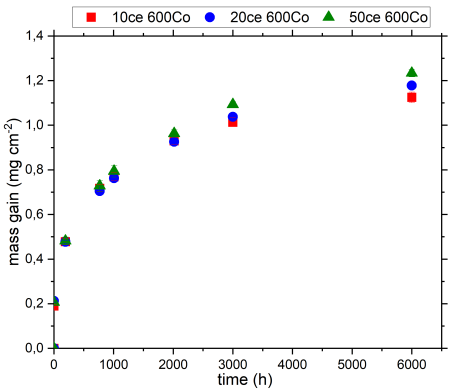

Figure 6.15: Mass gain of 10Ce600Co-, 20Ce600Co-, and 50Ce600Co-coated AISI 441 exposed at 800°C for 6,000 h in air + 3% H_2O.

6.5.2 Influence of Ce location in the Ce/Co coating

The presence of Ce in the Ce/Co coatings improved the oxidation resistance of the alloy, although increasing the Ce thickness did not provide any further improvement in oxidation resistance. To gain a better understanding of the mechanism of REE caused by Ce in Ce/Co coatings, several coatings similar to Ce/Co coatings were fabricated in different combinations and sequences on pre-oxidized Crofer 22 APU, as illustrated in Figure 6.16a, and b. The substrate, precut Crofer 22 APU (Figure 5.1b) was pre-oxidised for 3 minutes in a furnace that was pre-set to 900°C and then cooled in laboratory air. The pre-oxidation step resulted in the formation of a thin chromia layer on the steel. The substrate was pre-oxidised to inhibit the interdiffusion of metallic Co coatings with the steel, which has been shown to be detrimental [136].

The coatings shown in Figure 6.16a were fabricated by depositing 10 nm of Ce at different locations in the Co coating onto the pre-oxidised Crofer 22 APU. The coatings included: (a) 600 nm Co; (b) 10 nm Ce, followed by 600 nm Co (referred to as Ce/Co coating/ CeCoPVD coating in this thesis); (c) 300 nm Co then 10 nm Ce followed by 300 nm Co; and (d) 600 nm Co followed by 10 nm Ce. The terminology used for these coatings on pre-oxidised Crofer 22 APU is given in Figure 6.16a. The fabricated coatings were exposed to 850°C for 1,000 hours in air + 3% H_2O.

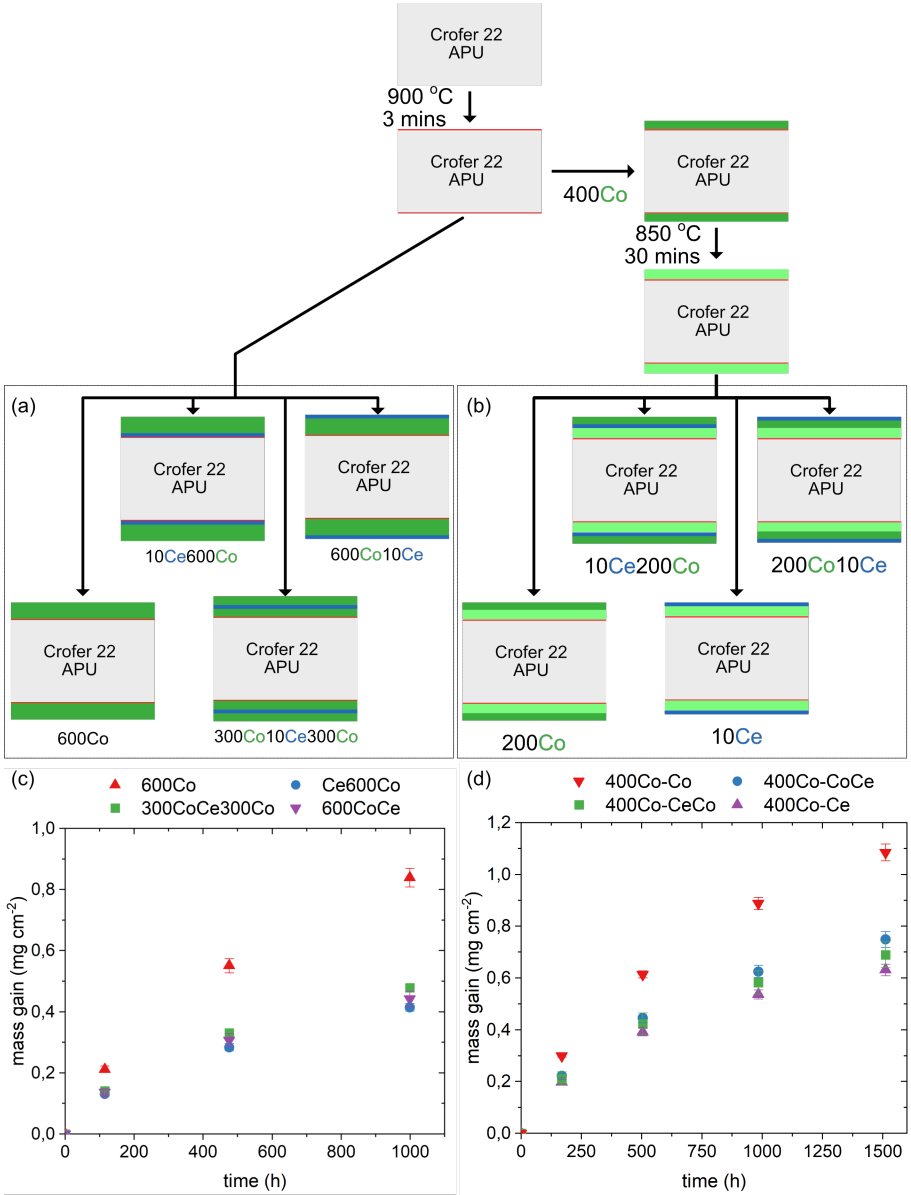

Figure 6.16: Fabricated coatings on pre-oxidised Crofer 22 APU (a) The four fabricated coatings are: 600 nm Co; 10 nm Ce + 600 nm Co; 300 nm Co + 10 nm Ce + 300 nm Co; and 600 nm Co + 10 nm Ce. (b) On four additional sheets of pre-oxidised Crofer 22 APU, 400 nm Co was deposited and then exposed to 850°C for 30 minutes to oxidise the Co to Co_3O_4. The four fabricated coatings are: 200 nm Co;10 nm Ce + 200 nm Co; 200 nm Co + 10 nm Ce; and 10 nm Ce. (c,d) Mass gains of the coated steels in (a), and (b) exposed to 850°C in air + 3% H_2O. Mass gain due to oxidation of metallic Co is subtracted from subsequent data before plotting.

Figure 6.16c shows the oxidation behaviours of the coated steels shown in Figure 6.16a, as represented by the mass gains. All the coatings showed rapid mass gains after 0.5 hours due to the oxidation of 600-nm metallic Co coating to Co_3O_4. This mass gain was subtracted from the subsequent data before plotting Figure 6.16c. The coating without Ce, 600Co, showed the highest mass gain. Moreover, all the coatings that contained Ce, irrespective of the location of Ce deposition, showed similar mass gains, substantially lower than that of 600Co. The 600Co10Ce coating, in which the Cr_2O_3 layer is separated from the Ce layer by 600 nm of Co, showed a similar mass gain as when Ce was deposited onto the Cr_2O_3 layer. After 1,000 hours, all the coated steels showed a continuous oxide scale with two layers: $(Co, Mn)_3O_4$ on top and Cr_2O_3 beneath (see Paper V). However, the Cr_2O_3 scale thickness on 600Co was notably greater than that on the coatings with Ce, supporting the observed mass gains. The continuous 10 nm of Ce in the coatings was detected as distinct Ce particles in the $(Co, Mn)_3O_4$. According to the commonly accepted mechanism of REE, the beneficial effect of Ce is manifested in the Cr_2O_3 layer. Due to the rapid oxidation of the Co coating, it is possible that Ce came in contact with the chromia scale in the 300Co10Ce300Co and 600Co10Ce coatings.

To prevent Ce interaction with the chromia scale, a second set of coatings – with Co_3O_4 oxide as a barrier between the Ce and chromia scale – was proposed (Figure 6.16b). Thus, 400 nm of Co was deposited on the pre-oxidised Crofer 22 APU, and this was further oxidised at 850°C for 30 minutes in a box furnace. The 400-nm Co coating oxidised to Co_3O_4 [88]. The thickness of the oxidised Co layer was ≈800 nm based on the Pilling-Bedworth ratio of Co. The oxidised coated steel substrate was then further coated with the following: (a) 200 nm Co; (b) 10 nm Ce followed by 200 nm Co; (c) 200 nm Co followed by 10 nm Ce; and (d) 10 nm Ce. Figure 6.16d shows the oxidation behaviours of the coatings shown in Figure 6.16b, as represented by mass gains. The mass gains in Figure 6.16d were plotted subtracting the mass gain due to the oxidation of the 200 nm Co coating in 200Co10Ce-, 10Ce200Co- and 200Co-coated steels. The coated steel without Ce had the highest mass gain, while coated steels with Ce had similar, substantially lower mass gains. Notably, a significant difference in mass gain was observed between the coated steel with and without Ce very early in the exposure (at 168 hours).

Figure 6.17 shows the time-resolved, back-scattered SEM micrographs of the cross-sections of the coated steels with Ce in the coating (200Co10Ce, 10Ce200Co and 10Ce) that were exposed for up to 500 hours. Ce appears bright in the back-scattered SEM micrographs because of its high atomic mass. After 0.5 hours of exposure, the Ce oxide in 10Ce200Co-coated steel appeared to be in a continuous layer sandwiched between Co_3O_4 layers, while in 200Co10Ce, it was spread in the outermost part of Co_3O_4 spinel at the air interface. After 24 hours of exposure, the Ce oxide appeared to be agglomerating, but it was in the same location as after 0.5 hours. In the 200Co10Ce- and 10Ce-coated steels, agglomerated Ce oxide particles were clearly visible in the outermost part of the $(Co, Mn)_3O_4$ spinel at the air interface. After 168 hours, the Ce particles appeared larger and closer to the Cr_2O_3 scale than before. The chromia scale increased in thickness; however, it had a similar thickness on all the coated steels in Figure 6.17, consistent with the mass gains in Figure 6.16d.

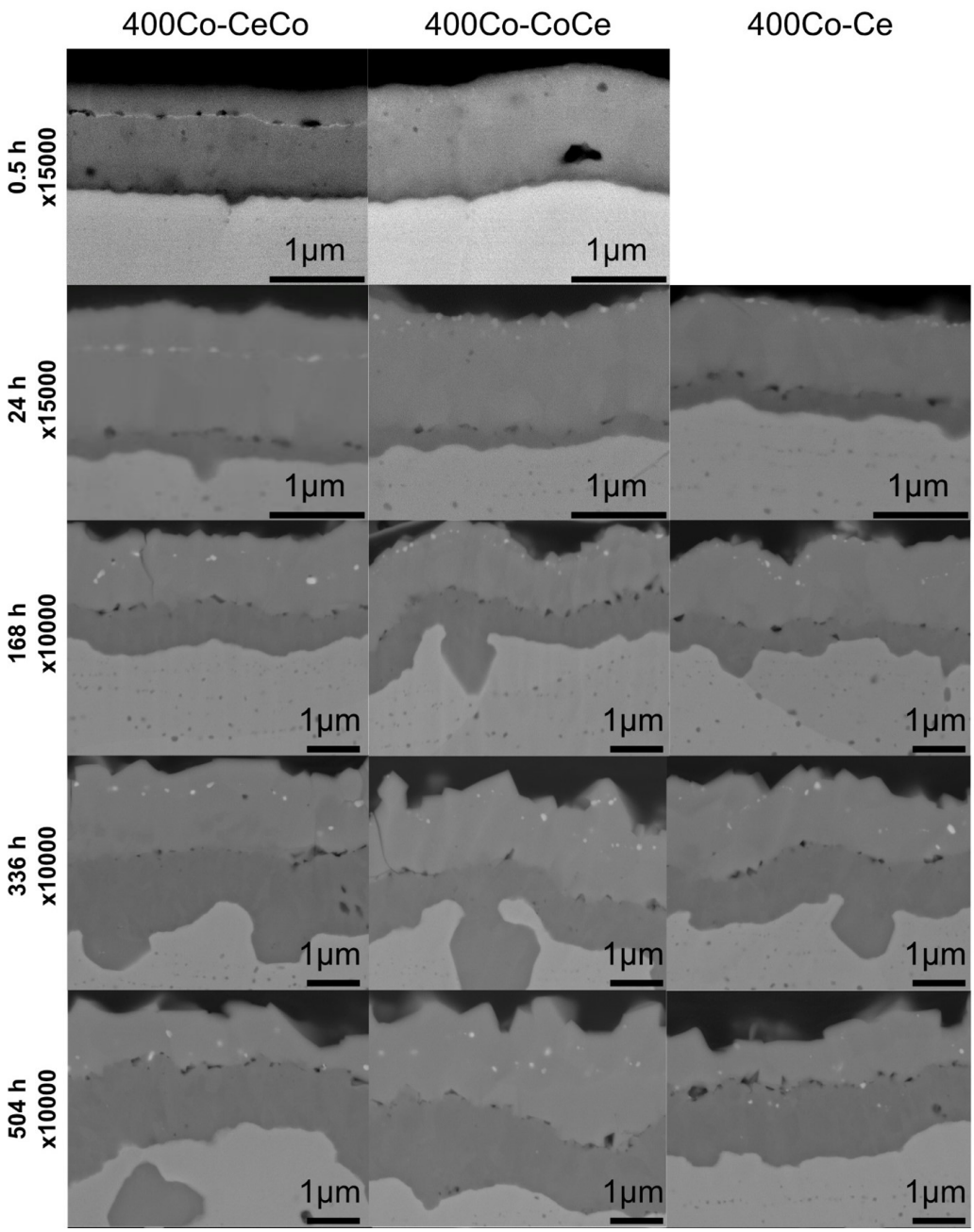

Figure 6.17: Time-resolved SEM images in the cross-section of 200Co10Ce, 10Ce200Co and 10Ce coated pre-oxidised Crofer 22 APU (refer to Figure 6.16b) exposed at 850°C till 500 hours in air + 3% H_2O.

The oxide scale thickness increased upon further exposure to 336 and 500 hours due to chromia scale growth. The Ce oxide particles in the 200Co10Ce- and 10Ce-coated steel, which were deposited at the coating-air interface, now appeared closer to the Cr_2O_3 -$(Co,Mn)_3O_4$ interface. The cross-sections of the coated steels shown in Figure 6.16b after 1500 hours can be found in Paper V. The Cr_2O_3 scale was thinner in the coatings with Ce, consistent with mass gains observed in Figure 6.16d.

Based on the gravimetric data shown in Figure 6.16c and d, it appears that the presence of Ce, regardless of its position relative to the chromia scale, is highly effective at reducing chromia scale growth. In the case of the 10Ce600Co-coated steel, it is plausible that Ce deposition on the Cr_2O_3 formed during pre-oxidation step resulted in a RE-doped chromia scale. Crofer 22 APU substrate contains La, hence some RE-doping of the chromia scale is expected, even in the substrate coated with only Co. However, adding Ce to the Co coating significantly reduces Cr_2O_3 scale formation. The 300Co10Ce300Co- and 600Co10Ce-coated steels have a Ce layer separated from Cr_2O_3 by 300 nm and 600 nm of metallic cobalt, respectively. In the coatings shown in Figure 6.16b, the Ce layer is separated from the Cr_2O_3 by 800 nm of oxide scale (Co_3O_4). Despite the separation, REE was observed, which means that the mechanisms commonly explained in terms of RE-doped chromia scale - whereby REs at the grain boundaries impede Cr^{3+} ions diffusion within the chromia scale and enhance O^{2-} ion diffusion - do not apply in this case. The solubility of Ce in the $(Co,Mn)_3O_4$ spinel is expected to be very low, owing to the large atomic radius of Ce, which would result in the Ce oxide accumulating at the grain boundaries. Thus, Ce particles at the grain boundaries of $(Co,Mn)_3O_4$ may impede the O^{2-} ions that are diffusing towards the chromia scale. This would result in slower chromia scale growth on the Ce-containing coated steels.

Surprisingly, the Ce-rich oxide particles appeared to move towards the steel substrate. After 1,500 hours of exposure, these particles were observed in the lower part of the spinel layer, closer to the chromia scale. In fact, some Ce-rich oxide particles were even found in the chromia scale (see Paper V). It is difficult to explain why Ce, which has a high affinity for oxygen, should be migrating towards the metal-oxide interface. Nevertheless, after 168 hours, when the Ce-rich oxide particles were at the deposited position, distant from the chromia scale (Figure 6.17), significant differences in mass gain were observed (Figure 6.16d), supporting the proposed mechanism.

The proposed mechanism is further supported by the mass gain data shown in Figures 6.4 and 6.8, where uncoated and Ce/Co-coated RE-free steels are compared to Crofer 22 APU. The oxidation kinetics of the uncoated steels varied greatly at 750°C, 800°C and 850°C (see Section 6.1). However, all of the steels behaved similarly once coated with Ce/Co. The mass gains of the Ce/Co-coated steels at 800°C are presented in Figure 6.8, and those at other temperatures are presented in Figure 6.18. This indicates that the kinetics of the chromia scale growth is determined by the Ce/Co coating on the steel, rather than the inherent behaviour of the steel itself. This further strengthens the argument that the presence of Ce in the spinel layer governs the oxidation kinetics of the chromia scale.

6.6 Predicting the lifetime of the interconnect

The FSS used as interconnects rely on the formation of a slow-growing, protective chromia scale, which prevents rapid oxidation of the interconnect. Cr in the steel is consumed by Cr_2O_3 scale growth and Cr evaporation, leading to the depletion of Cr in bulk over time. Chromium depletion below a certain threshold will lead to breakaway oxidation, limiting the lifetime of the SOC stack. One of the biggest concerns with using low-cost FSS is the low chromium content, typically in the range of 16-19 wt% compared to tailor-made steels (22-24 wt%). Low-cost steels may not sustain long-term operation and can lead to stack failure due to their low Cr content. Therefore, thicker steel components must be used as interconnects to compensate for the lower Cr content. This contrasts with market demands to reduce the size and/or weight of fuel cells.

To optimise the thickness and material selections for the interconnects, it is important to estimate their lifetime. However, predicting the lifetime of an FSS interconnect is difficult, and has been a long-cherished dream of corrosion scientists. First, the steels that have high Cr contents take a very long time to undergo breakaway corrosion. Although low Cr-content steels undergo breakaway corrosion faster, the data cannot be easily extrapolated. This is due to significant variations in the oxidation kinetics and Cr evaporation of these steels, as shown in Figures 6.4 and 6.1. When coated with Ce/Co, various steels exposed to 800°C exhibited very low but highly similar Cr evaporation (Figure 6.7) and oxidation rates (Figure 6.8), regardless of their behaviours when uncoated. If similar oxidation behaviours for various Ce/Co-coated steels are observed at other temperatures, a model can be developed to determine their lifetime, which would be valid regardless of the steel composition. For these experiments, Ce/Co-coated FSS, AISI 409, AISI 430, AISI 441, and Crofer 22 APU, with varying Cr contents (11.4-22.9 wt%; Table 5.1), were exposed in air + 3% H_2O at temperatures in the range of 750°C to 900°C for up to 1,500 hours.

6.6.1 Oxidation kinetics - Influence of temperature

Figure 6.18 shows the oxidation behaviours of Ce/Co-coated AISI 409, AISI 430, AISI 441, and Crofer 22 APU in terms of mass gains. All of the coated steels showed a rapid mass gain during the first few hours due to rapid oxidation of the metallic Co coating, regardless of the temperature of exposure. At 900°C, Ce/Co-coated AISI 409 (11.4 wt% Cr) and AISI 430 (16 wt% Cr) experienced rapid breakaway corrosion within the first 24 hours. Ce/Co-coated AISI 409 was completely oxidised while breakaway corrosion of AISI 409 progressed along the edges. In contrast, Ce/Co-coated AISI 441 (17.5 wt% Cr) and Crofer 22 APU (22.9 wt% Cr) remained protective for 1,500 hours, exhibiting parabolic oxidation kinetics. In contrast, Huczkowski et al. [106, 110] reported breakaway corrosion of 0.3 mm Crofer 22 APU after 1,000 hours. The observed differences in behaviours can be attributed to the low Cr evaporation and low oxidation rate on the Ce/Co-coated Crofer 22 APU. Furthermore, the oxidation rates of Ce/Co-coated AISI 441 and Crofer 22 APU were similar at 900 °C, despite the lower Cr content and the absence of reactive elements in AISI 441.

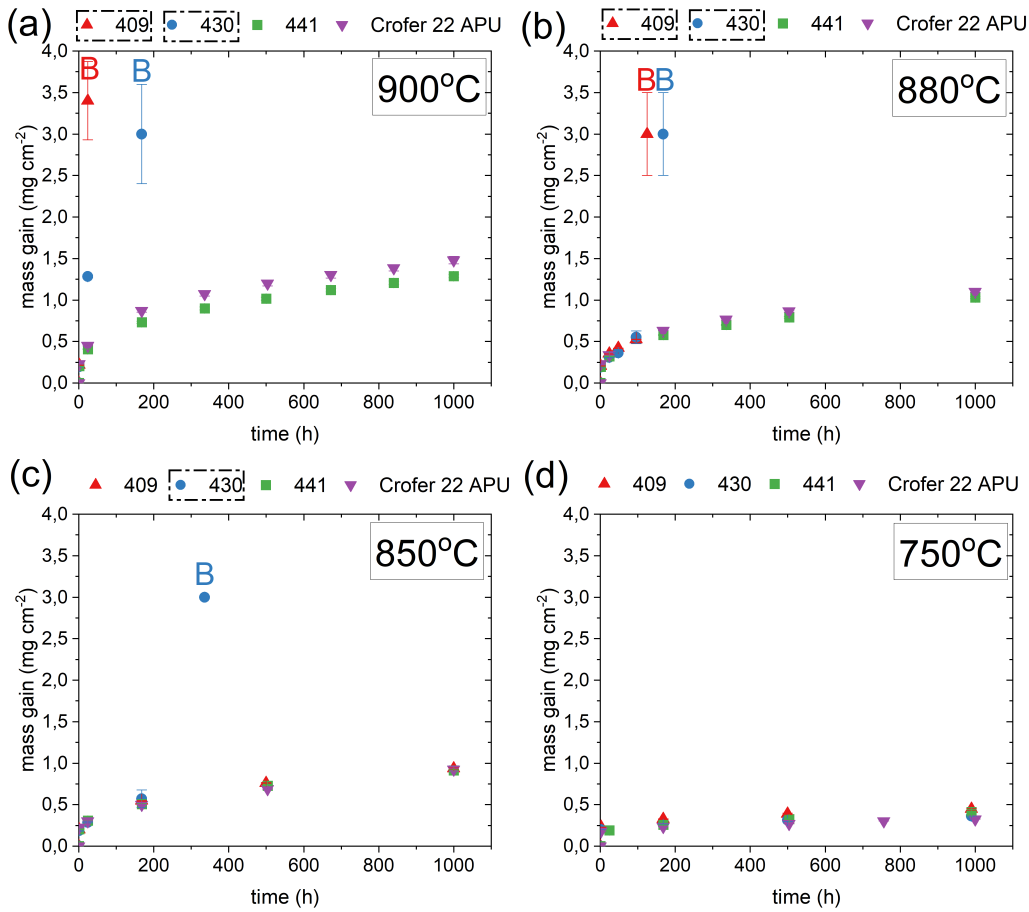

Figure 6.18: Mass gains of Ce/Co-coated AISI 409, AISI 430, AISI 441 and Crofer 22 APU exposed at temperatures in the range of 750°-900°C for 1,000 h in air + 3% H_2O. The "B" indicates the time at which breakaway corrosion was observed.

At 880°C, Ce/Co-coated AISI 409 and AISI 430 remained protective for 96 hours; however, breakaway corrosion was observed after 120 hours. The Ce/Co-coated AISI 441 and Crofer 22 APU remained protective and showed similar oxidation kinetics until 1,000 hours (Figure 6.18b). To understand further the early breakaway of AISI 430, Ce/Co-coated AISI 430 and AISI 409 were exposed at 865°C. Ce/Co-coated AISI 430 suffered breakaway corrosion between 24 and 168 hours, while Ce/Co-coated AISI 409 suffered breakaway corrosion between 600 and 800 hours. These are interesting outcomes, given that AISI 430 has a 50% higher Cr content than AISI 409, which will be addressed in Section 6.6.1.1

At 850°C, all Ce/Co-coated steels, with the exception of AISI 430, remained protective and showed highly similar oxidation kinetics up to 1,000 hours (Figure 6.18c). However, Ce/Co-coated AISI 430 suffered breakaway corrosion within 336 hours. Nonetheless, at 800°C and 750°C, AISI 430 remained protective for up to 3,000 and 1,500 hours, respectively. The oxidation behaviours of the various Ce/Co-coated steels were similar at the respective temperatures of 800°C (Figure 6.8b) and 750°C (Figure 6.18d).

The mass gain data presented in Figure 6.8 and Figure 6.18 were used to calculate the oxidation rate constants of the Ce/Co-coated steels at different temperatures, as determined by Equation (6.2). These oxidation rate constants were plotted against exposure temperature in an Arrhenius plot (Figure 6.19). The temperature dependence of the oxidation process in the Ce/Co-coated steels was observed. The activation energy for chromia scale formation was found to be 260 kJ mol^{-1}. Based on this activation energy, the oxidation kinetics of the Ce/Co-coated steels could be estimated at any temperature, provided the chromia scale formation mechanism does not change.

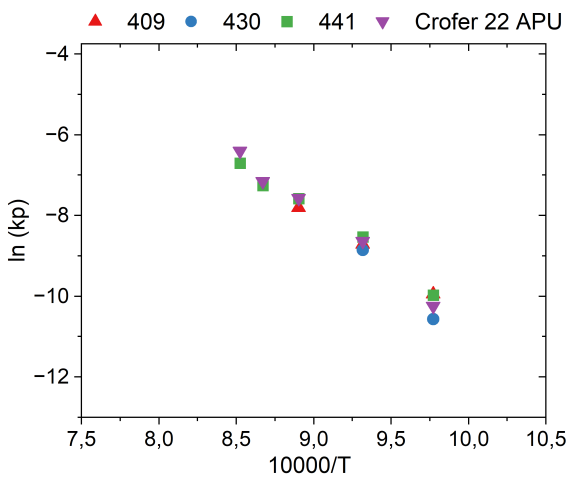

Figure 6.19: Arrhenius plot of the oxidation kinetics (k_p) of the Ce/Co-coated steels, AISI 441, AISI 430, AISI 409 and Crofer 22 APU exposed for 1,000 hours at the temperatures in the range of 750°- 900°C.

6.6.1.1 Premature failure - AISI 430

As previously discussed, Ce/Co-coated AISI 430 underwent breakaway corrosion within 336 hours when exposed to temperatures > 850°C. However, with only a slightly higher Cr content, the Ce/Co-coated AISI 441 remained protective for 3,000 hours at 850°C. Moreover, due to the difference in thickness between AISI 441 (0.30 mm) and AISI 430 (0.38 mm), the total Cr content of AISI 430 is higher than that in AISI 441. These data suggest that factors other than Cr content in the steel play a role in the breakaway corrosion of Ce/Co-coated AISI 430.

Based on the alloy composition (Table 5.1), the major differences in composition between AISI 441 and AISI 430 are: (i) lower Cr concentration in AISI 430; (ii) higher C concentration in AISI 430; and (iii) lack of ferritic stabilisers, such as Nb and Ti, in AISI 430. It is suggested that the lack of ferrite stabilisers and higher C content in AISI 430 might have caused a transition from ferrite to austenite at higher exposure temperatures. Previous studies [180] have shown that Cr diffusion is significantly lower in an austenitic structure than in a ferritic structure. This transition could have led to the breakaway corrosion observed at temperatures > 850°C.

Figure 6.20a shows the JMatPro analysis of AISI 430 (Table 5.1). The calculations show that the austenite phase in AISI 430 at 850°C is expected to be above 20 wt%. It is proposed that the transformation of ferrite to austenite resulted in slower Cr diffusion to the surface, leading to the breakaway corrosion observed in the exposures conducted at and above 850°C. Long lifetimes were observed below 800°C, as there is no austenitic transformation at this temperature. In a steel with a lower C content and 0.44 wt% titanium (Figure 6.20b), it was calculated that no austenitic transformation occurred up to 1200°C.

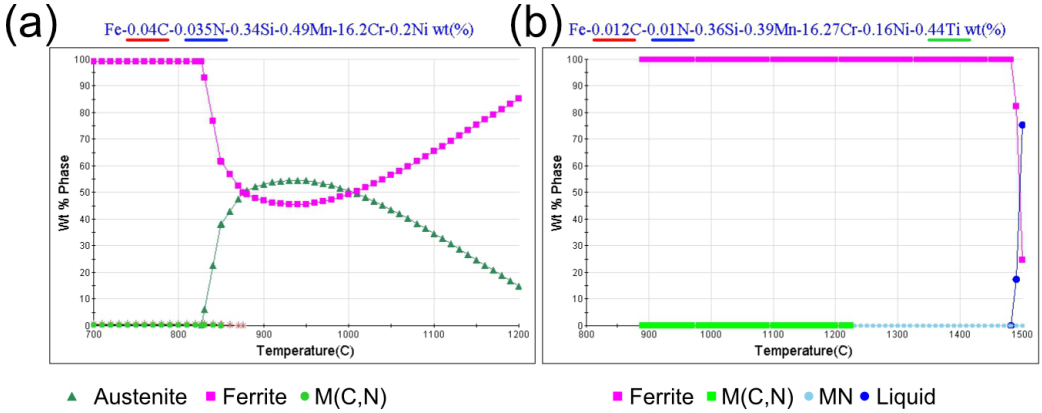

Figure 6.20: JMatPro phase analysis of (a) investigated AISI 430 and (b) Ti stabilised AISI 430 [181]

6.6.2 Breakaway Corrosion - Ce/Co-coated AISI 409

Due to the low Cr content of AISI 409 (11.4 wt%), it is possible for Ce/Co-coated AISI 409 to undergo breakaway corrosion at 850°C in a relatively shorter time than AISI 441 or Crofer 22 APU. Upon further exposure of > 1,000 hours, it was observed that the Ce/Co-coated AISI 409 suffered breakaway corrosion between 1500-2300 hours. The breakaway corrosion started at the connecting points of the coupon to the frame, as shown in Figure 6.21, and progressed along the edges. It is commonly observed that breakaway starts at the corners and edges, in part due to out-of-plane tensile stresses and/or the higher metal consumption that results from a larger surface-to-volume ratio [112]. After prolonged exposure, breakaway corrosion was observed on the faces, too, as shown in Figure 6.21. Based on data from different exposures, the mass gain at the onset of breakaway corrosion was found to be 0.91 ± 0.02 mg.cm^{-2}, excluding the mass gain due to coating oxidation.

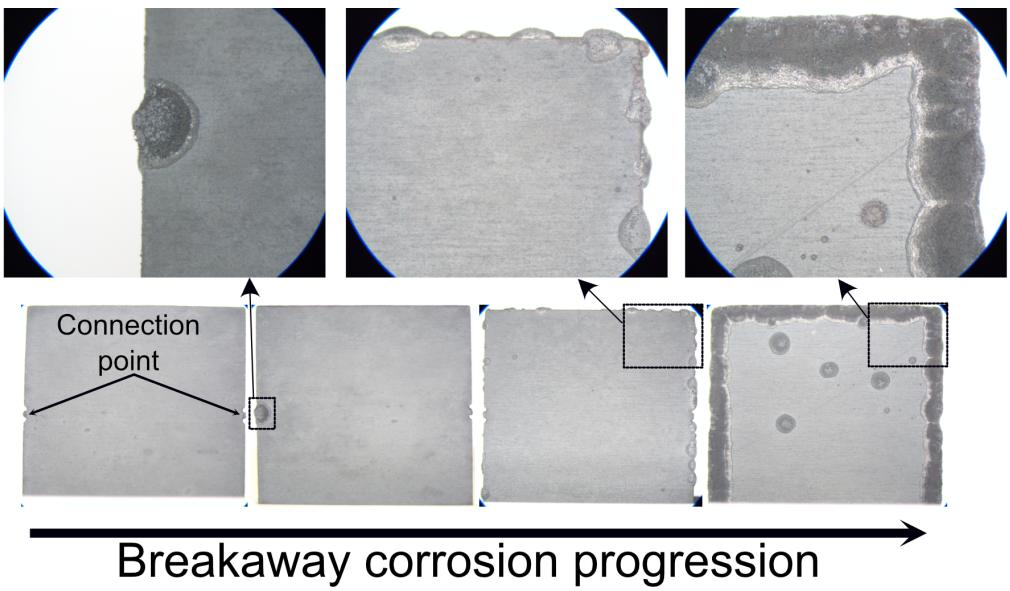

Figure 6.21: Corrosion progression on Ce/Co-coated AISI 409 exposed at 850°C in air + 3% H_2O.

The mass gain recorded before failure (≈ 0.91 mg.cm^{-2}) is the sum of the mass gain due to Cr oxidation and mass loss of Cr due to Cr evaporation. Due to the high effectiveness of Ce/Co coatings in inhibiting Cr evaporation, the amount of Cr lost is minimal (For 2,000 hours, it is less than 0.01 mg.cm^{-2}). Therefore, the uptake of oxygen to form oxides, primarily Cr_2O_3, resulted in a mass gain of 0.91 mg.cm^{-2} (not including the oxidation of the metallic coating). It should be noted that a small part of the mass gain arose from the oxidation of Mn diffusing to the coating to form $(Co, Mn)_3O_4$, as well as from internal oxidation of Al and Si. However, due to the low concentrations of these elements, their

contributions to the final mass gain are expected to be very low.

6.6.3 Lifetime Model

The oxidation kinetics for the various steels coated with Ce/Co at 850°C were very similar (Figure 6.18). Based on the insights obtained from the breakaway corrosion on Ce/Co-coated AISI 409, it is possible to predict the lifetime based on the Cr depletion for the other Ce/Co-coated steels. To develop a model, the following assumptions were made:

1. The measured mass gain is solely due to the uptake of oxygen by chromium to form Cr_2O_3;
2. No spallation has occurred over the coupon or its edges. (Not observed experimentally);
3. Cr depletion in the steel does not result in a gradient being formed beneath the oxide layer, i.e., the Cr concentration in the bulk is flat. (Experimentally, a flat profile is observed at 850°C for Ce/Co coated AISI 409).
4. The thickness of the steel is constant throughout its lifetime.

The oxidation kinetics, determined by the mass gain at 850°C (Figure 6.18c), of Ce/Co-coated AISI 409 followed parabolic oxidation kinetics. The relationship between the mass gain and oxidation kinetics can be described by Equation (6.2):

$$\Delta m_o^2 = k_p * t + A \tag{6.2}$$

where Δm_o (in mg.cm^{-2}) is the mass gain per unit area due to the uptake of oxygen, k_p is the parabolic rate constant, t is the exposure time (in hours), and A is the integration constant. Following the assumption that the oxygen uptake is solely due to the formation of the Cr_2O_3 scale, the amount of Cr consumed per unit area Δm_{Cr} (in mg.cm^{-2})in the oxide scale is given by Equation (6.3)

$$\Delta m_{Cr} = \Delta m_O * \frac{2}{3} * \frac{M_{Cr}}{M_O} = 2.168 * \Delta m_O \tag{6.3}$$

where Δm_O (in mg.cm^{-2}) is the mass gain due to oxygen uptake, and M_O and M_{Cr} are the atomic masses of oxygen and Cr, respectively. The Ce/Co-coated AISI 409 was exposed to air on both sides. Thus, for the Cr_2O_3 scale formation on one face, Cr is depleted from half the volume, i.e., $\frac{1}{2} * \mathrm{t} * \mathrm{A}$, where t is the thickness (in cm) and A is the area (in cm^2). The $\Delta \mathrm{m_{Cr}}$ per unit area after time t can be determined using Equation (6.4):

$$\Delta m_{Cr} = \frac{C_o - C_t}{100} * \rho * \frac{h}{2} \tag{6.4}$$

where ρ is the density of the steel (in mg.cm^{-3}), C_o is the Cr content of the steel (in wt%) in the as-received coupon, and C_t is the Cr content of the steel in wt% after time t. The breakaway oxidation is observed along the edges due to the larger surface-to-volume ratio.

For specimens with rectangular cross-sections having length l, width w and thickness h, the specimen thickness in Equation (6.4) is replaced by a factor based on the ratio of surface to volume [105], as expressed in Equation (6.5):

$$h_{rectangle} = \frac{h}{1 + \frac{h}{l} + \frac{h}{w}} \tag{6.5}$$

The mass gain (Δm_O) at the breakaway corrosion of Ce/Co-coated AISI 409 was found to be 0.91 mg.cm^{-2}. Using Equations (6.3) and (6.4), the experimental mass gain can be used to calculate the C_t (Cr content of the steel in wt% at time t). It was calculated that the Cr content (C_{1500h}) after 1,500 hours of exposure at 850°C in the Ce/Co-coated AISI 409 was 10.06 wt%. The critical Cr content at breakaway corrosion ($C_{breakway}$) was 10.06 wt% at 850°C as the steel proceeded to breakaway corrosion after 1500 hours. This matches well with the critical Cr content determined by other researchers for a similar temperature range [108, 182]. Using Equations (6.2) and (6.3), the mass of Cr consumed after time t can be derived from Equation (6.6):

$$\Delta m_{Cr}^2 = 4.70 * k_p * t + A \tag{6.6}$$

In the case where the parabolic integration constant is 0, Equation (6.6) can be re-arranged as Equation (6.7):

$$t = \frac{\Delta m_{Cr}^2}{4.70 * k_p} \tag{6.7}$$

By re-arranging Equations (6.4) and (6.7) reveals the time required to deplete the initial Cr content C_o to a lower Cr content C_t after time t. If the Cr concentration at the onset of the breakaway corrosion $C_{breakaway}$ is defined, the time to breakaway corrosion $t_{breakaway}$ can be defined using Equation (6.8):

$$t_{breakaway} = \left(\frac{C_o - C_{breakaway}}{100} * \rho * \frac{h}{2}\right)^2 * \frac{1}{4.70 * k_p} \tag{6.8}$$

The lifetime of the Ce/Co-coated steels calculated in Equation (6.8) are only valid when Cr evaporation is ignored. The $C_{breakaway}$ of Ce/Co-coated AISI 409 is used as the reference for Ce/Co-coated AISI 441 and Crofer 22 APU. The k_p values of Ce/Co-coated AISI 441 and Crofer 22 APU, which were calculated based on the mass gain data in Figure 6.18, and the time to failure at different thicknesses are shown in Figure 6.22b. Based on the time to breakaway revealed by Equation (6.8), it is clear that the time to breakaway corrosion is proportional to the square of the thickness of steel ($t_{breakaway} \propto h^2$). Figure 6.22a shows the $t_{breakaway}$ values of Ce/Co-coated steels with different Cr contents (wt%) in the steel as a function of thickness. Increasing the thickness or Cr content significantly improves the time to failure of a Ce/Co-coated steel. To use a low-cost, low-Cr steel such as AISI 441 to achieve the same lifetime as Crofer 22 APU, the thickness of the AISI 441 would have to be greater, as shown in Figure 6.22b.

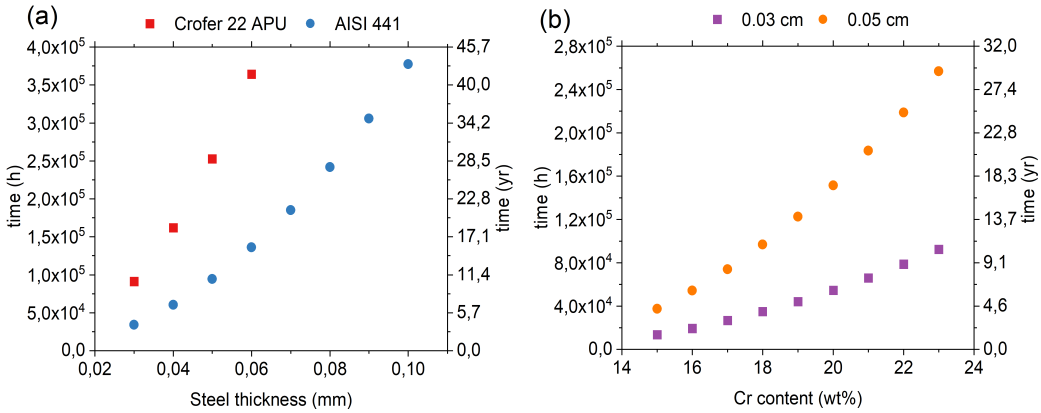

Figure 6.22: (a) Influence of steel thickness and steel composition and (b) influence of Cr wt% and thickness on time to failure of Ce/Co-coated steel at 850°C.

The predicted lifetime of a Ce/Co-coated, 0.03 mm thick Crofer 22 APU is about 10^5 hours at 850°C. This would translate to a mass gain of more than 7 mg.cm^{-2}, which corresponds $\approx$ 42 μm thick chromia scale. Such long lifetimes depicted in Figure 6.22 might not be achieved, as the oxide scales are prone to spallation above a certain thickness. Although the evaporation rate is extremely low for Ce/Co-coated steels, it can still be significant over a long period, reducing the lifetime. Cr diffusion in the steel is suggested to be influenced by hydrogen on the fuel side [143], which might also affect $C_{breakaway}$. Moreover, the present approach is applicable only when the Cr depletion profile in the steel is flat. However, this is not expected to be the case for chromia-forming FSS at intermediate temperatures [183].

At other temperatures, the critical chromium concentration, $C_{breakaway}$, changes with temperature. The second criterion derived from the Wagnerian depletion model can be used to calculate the critical chromium concentration required to maintain the chromia scale as shown in Equation (6.9):

$$N_{Cr}^{crit,2} > \frac{V_M}{V_{M_xO_y}} \left(\frac{\pi k_p}{2\tilde{D}_{Cr}} \right)^{\frac{1}{2}} \tag{6.9}$$

where V_M and $V_{M_xO_y}$ are the molar volumes of the alloy and oxide, respectively. k_p is the parabolic oxidation constant, $\tilde{D}_{Cr}$ is the diffusivity of Cr. Based on Equation (6.9), the $N_{Cr}^{crit,2}$ is dependent on $\frac{\pi k_p}{2\tilde{D}_{Cr}}$, which is dependent of temperature. Unfortunately, the reported values of $\tilde{D}_{Cr}$ vary significantly, and thus it is difficult to extract meaningful lifetime predictions at lower temperatures. Further work is needed to develop the lifetime model to be applicable at lower temperatures.

6.7 Coatings for SOEC

While MCO coatings offer good performance, cobalt is considered a critical raw material by the EU, so avoiding its use would provide significant cost and material handling benefits. A Ni-oxide cap layer has been shown to be effective in reducing chromium evaporation [117]. However, it has been reported that Ni coatings on FSS interconnects can transform the surface beneath the coating to austenite [184, 185], which can result in the loss of contact due to differences in TEC [48] or breakaway corrosion caused by slower Cr diffusion in the FCC structure [180]. The $(Fe,Ni)_3O_4$ spinel cap layer formed on Alloy 800H (Figure 6.32b) was very effective in reducing Cr evaporation. Hence, FeNi-based coatings appear to be interesting for interconnect applications. Ce/FeNi and Ce/Co coatings on AISI 441 were compared at 850°C in dry air and air + 3% H_2O.

6.7.1 Chromium evaporation

Figure 6.23 shows that the Cr evaporation for the uncoated AISI 441 in wet air (air + 3% H_2O) is an order of magnitude higher than in dry air (air + 0.1% H_2O). This is because the formation of $CrO_2(OH)_2$, as shown in Equation 3.9, is significantly reduced in dry air. This data further shows that Cr evaporation is not a significant concern in SOEC atmospheres. Figure 6.23b shows the Cr evaporation for Ce/Co- and Ce/FeNi-coated AISI 441 in wet air. The Cr evaporation for Ce/FeNi-coated AISI 441 in wet air is significantly higher than that for Ce/Co-coated AISI 441 but is still 4-5 times lower than that of the uncoated steel. The Cr evaporation data for Ce/FeNi-coated AISI 441 matches well with that for Alloy 800H (Figure 6.31a), which formed $(Fe,Ni)_3O_4$ spinel. The high Cr evaporation in wet atmospheres makes Ce/FeNi coatings unsuitable for SOFC air electrode atmospheres. Nevertheless, they can be used in SOEC atmospheres where Cr evaporation is not a significant issue due to low H_2O content.

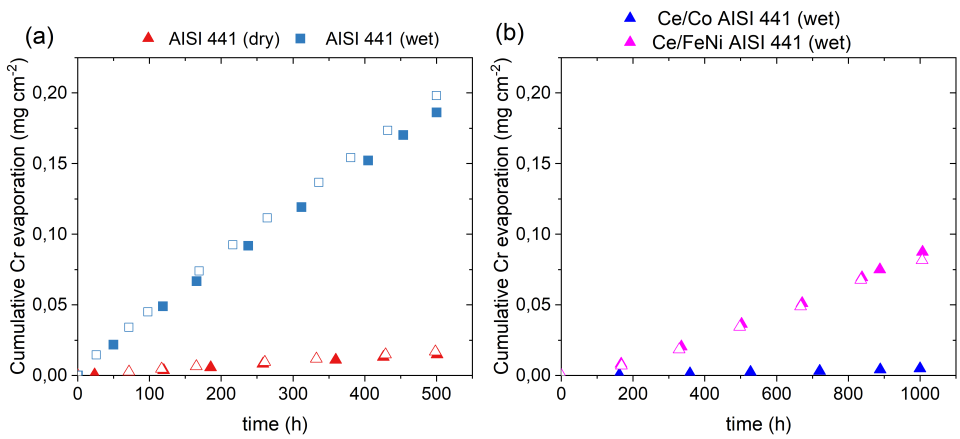

Figure 6.23: Cumulative Cr evaporation (a) uncoated AISI 441 in wet (air + 3% H_2O) and dry air (b) Ce/Co-coated and Ce/FeNi-coated AISI 441 in wet air at 850°C for up to 1,000 hours.

6.7.2 Oxidation kinetics

Figure 6.24 shows the mass gains of AISI 441 coated with 10 nm Ce, Ce/Co, and Ce/FeNi in dry air at 850°C. The mass gain after 0.5 hours, which represents the mass gain due to coating oxidation, is subtracted from subsequent data before plotting Figure 6.24 to make the data comparable. Extensive spallation is observed on the uncoated steel after only 168 hours, so the data are not plotted. The Ce-coated steel had the highest mass gain, followed by the Ce/Co- and Ce/FeNi-coated steels. The 10 nm Ce coating on the steel improved the adhesion of the oxide scale and reduced the growth of the oxide scale. However, the addition of Co or FeNi further improved the oxidation resistance. Additionally, there is a significant difference in the mass gains and oxidation rate constant (see Paper VI) between the Ce/Co- and Ce/FeNi-coated steels, indicating that the Ce/FeNi coating is very effective in improving oxidation resistance. However, the reason behind this improved behaviour is not understood.

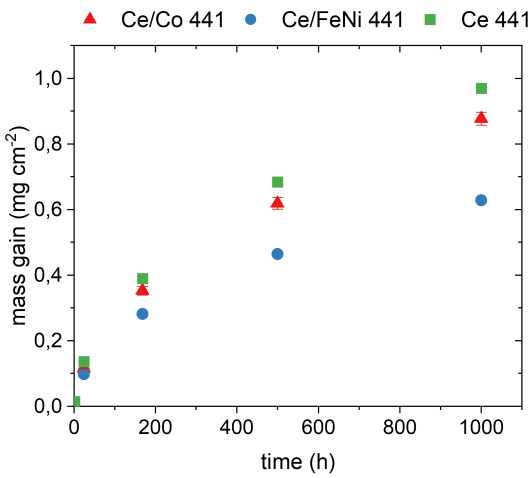

Figure 6.24: Mass gains of Ce-, Ce/Co- and Ce/FeNi-coated AISI 441 exposed in dry air at 850°C for 1,000 hours. The initial data point after 30 mins (mass gain due to coating oxidation for Ce/Co- and Ce/FeNi-coated AISI 441) is subtracted from subsequent data before plotting.

6.7.3 Microstructural Characterisation

Figure 6.25 shows SEM micrographs of the cross-section of AISI 441 coated with Ce/Co and Ce/FeNi, exposed to 850°C for 1,000 hours. Both coated steels exhibit a multilayered, continuous oxide scale with no signs of spallation. The cap layers on Ce/Co and Ce/FeNi coated steels are $(Co, Mn)_3O_4$ and $(Fe, Ni, Mn)_3O_4$, respectively. The chromia scale appears to be thinner on the Ce/FeNi coated steel, consistent with the observed mass gains. The EDX analysis shows up to 9 at% Cr and 5 at% Cr in the $(Co, Mn)_3O_4$ and $(Fe, Ni, Mn)_3O_4$, respectively. Froitzheim et al. [88] showed very low

Cr content in the $(Co, Mn)_3O_4$ spinel after 3,000 hours of exposure to air + 3% H_2O at 850°C using TEM. The high Cr content in spinel in the present case can be due to the absence of Cr evaporation or lower stability of $(Co, Mn)_3O_4$ spinel in dry air.

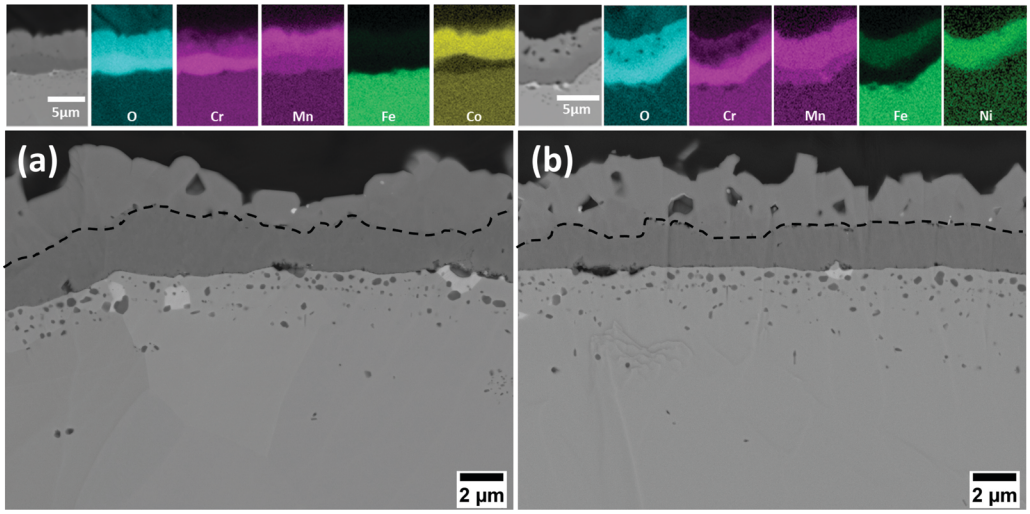

Figure 6.25: SEM micrographs in the cross-section of (a) Ce/Co- (b) Ce/FeNi-coated AISI 441 exposed in dry air at 850°C for 1,000 hours.

6.7.4 Area-specific resistance

Figure 6.26 shows the in-situ ASR measurements conducted on Ce/Co- and Ce/FeNi-coated AISI 441 at 850 °C in laboratory air for almost 3,200 h. The ASR measurements were carried out by a collaborator at the Technical University of Denmark. A load of 7 kg was applied, and a current density of 0.5 Acm^2 was used for the measurements. For more details on the in-situ ASR measurements, see Paper VI. The Ce/FeNi-coated AISI 441 showed consistently lower ASR than Ce/Co-coated AISI 441. Unplanned thermal cycles occurred after 1,200 h, 1,350 h, and 2,065 h of exposure, increased the degradation of Ce/Co 441. Furthermore, AISI 441 coated with Ce/FeNi exhibited improved robustness against contact loss during thermal cycling (see Paper VI).

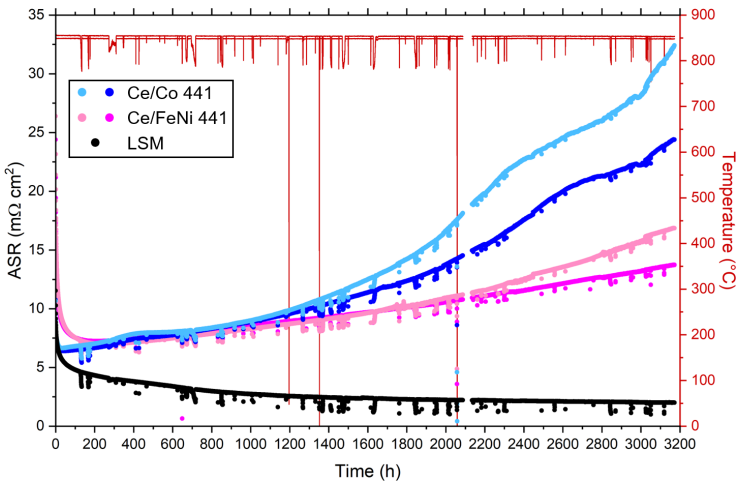

Figure 6.26: Isothermal in-situ ASR measurements conducted on Ce/Co- and Ce/FeNi-coated AISI 441 at 850 °C in laboratory air for almost 3,200 h.

6.8 BOP materials

To represent the multitude of metallic materials available for use in BOP components, four different groups of materials, chromia-forming FSS, alumina-forming FSS, Fe-base austenitic steel, and Ni-base alloy, were examined for their potential applications in BOP components. Table 5.2 lists five different alloys together with their compositions. The performances of these alloys were evaluated in a typical air side SOFC environment for 500 hours at 650°C and 850°C. In addition, to understand the effect of pre-oxidation, the coupons were pre-oxidised at 900°C for 24 hours and were then further exposed to 650°C for 500 hours. The mass gain due to pre-oxidation is reported in Paper VIII. The mass gain plots of the pre-oxidised alloys in the following sections represent the oxidation kinetics after pre-oxidation. Thus, they do not include the mass gain due to pre-oxidation.

6.8.1 AISI 441 and AISI 444

Figure 6.27 shows that the Cr evaporation of AISI 444 was slightly lower than that of AISI 441 at 650°C for the as-received coupons. This contrasts with the behaviours observed at 750°C (see Section 6.1) whereby AISI 444 had a higher Cr evaporation. However, the Cr evaporation of pre-oxidised AISI 441 and AISI 444 were similar and about 30% lower than those of the as-received materials. This is attributed to the formation of a continuous $(Cr, Mn)_3O_4$ spinel during pre-oxidation. At 850°C, the Cr evaporation of the as-received AISI 444 and AISI 441 were similar, as observed in Figure 6.1e.

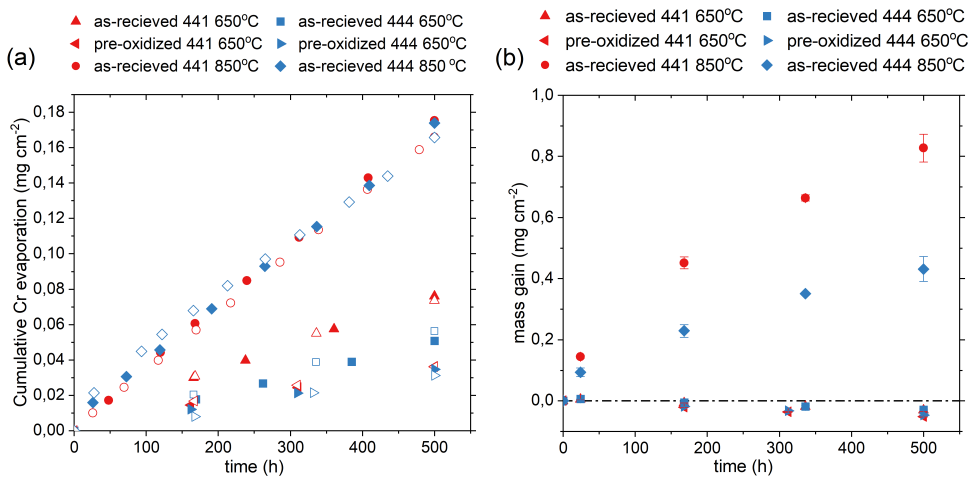

Figure 6.27: (a) Cr evaporation and (b) mass gain as a function of time for the as-received and pre-oxidised AISI 441, and AISI 444 exposed at 650°C and as-received AISI 441, and AISI 444 exposed at 850°C, for 500 h in air + 3% H_2O. The open and filled symbols represent two individual exposures.

Both steels showed similar mass losses after 500 hours at 650°C for the as-received and pre-oxidised coupons (Figure 6.27b). The mass gain behaviours of the as-received coupons at 650°C showed paralinear oxidation kinetics. As discussed in Section 3.4, Cr evaporation significantly affects the oxidation behaviour. For the corrected mass gains, which represent the true extent of oxidation, refer to Paper VII. The pre-oxidised AISI 441 and AISI 444 showed continuous mass loss due to slow oxidation kinetics. The corrected mass gain of the pre-oxidised coupons was lower than that of the as-received coupons (see Paper VII), indicating an improvement in the oxidation behaviour after pre-oxidation.

At 850°C, a considerable difference was observed between the net and corrected mass gains of the as-received coupons. AISI 441 showed a much higher mass gain than AISI 444 after 500 hours. Since the Cr evaporation was similar, the corrected mass gain of AISI 441 was also higher than that of AISI 444 (see Paper VII). Even after pre-oxidation for 24 hours at 900 °C, a significant difference in mass gain was observed between AISI 441 and AISI 444. The oxide scale structures of AISI 441 and AISI 444 at 850°C, (EDX maps in Figure 6.28), were similar, with an inner continuous Cr_2O_3 scale and a continuous $(Cr, Mn)_3O_4$ spinel on the top. The oxide scales at 850°C (Figure 6.28) were thinner on AISI 444 (2-3 μm) than on 441 (3-4 μm). The thickness of the oxide scale matches well with the observed mass gain (Figure 6.27b).

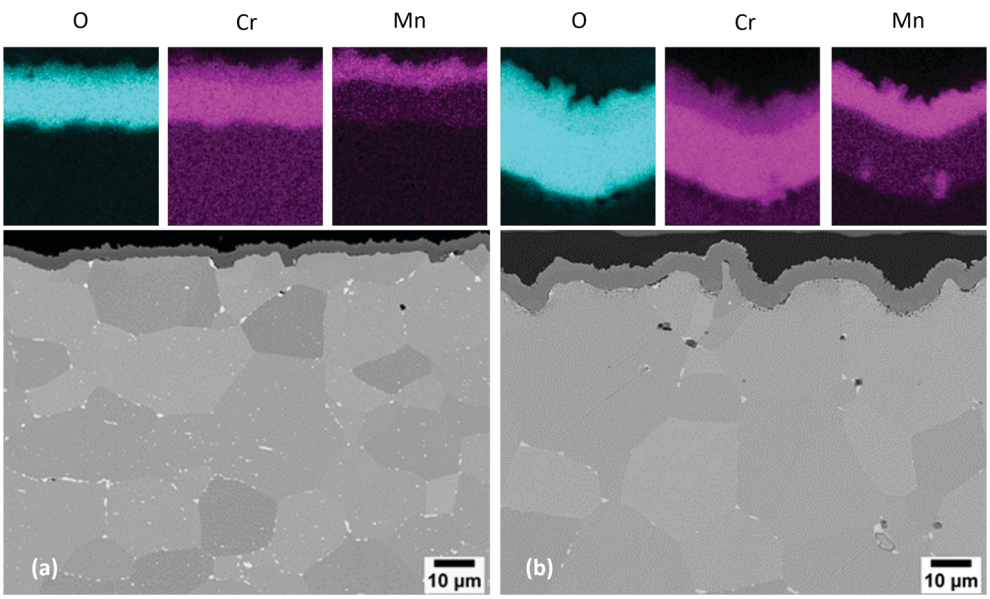

Figure 6.28: SEM cross-sectional micrographs of: (a) AISI 444; and (b) AISI 441 after exposure at 850°C for 500 h in air + 3% H_2O.

6.8.2 Alloy 600

The Cr evaporation of chromia forming Ni-base material, Alloy 600 is shown in Figure 6.29a. Cr evaporation is 2-3 times lower than that of AISI 441 or AISI 444 at the respective investigated temperatures. The Cr evaporation of the as-received Alloy 600 is 4 times lower at 650°C than at 850°C; however, a similar mass gain was observed at both temperatures. The pre-oxidised Alloy 600 showed a mass loss and about 50% lower Cr evaporation than the as-received Alloy 600 at 650°C.

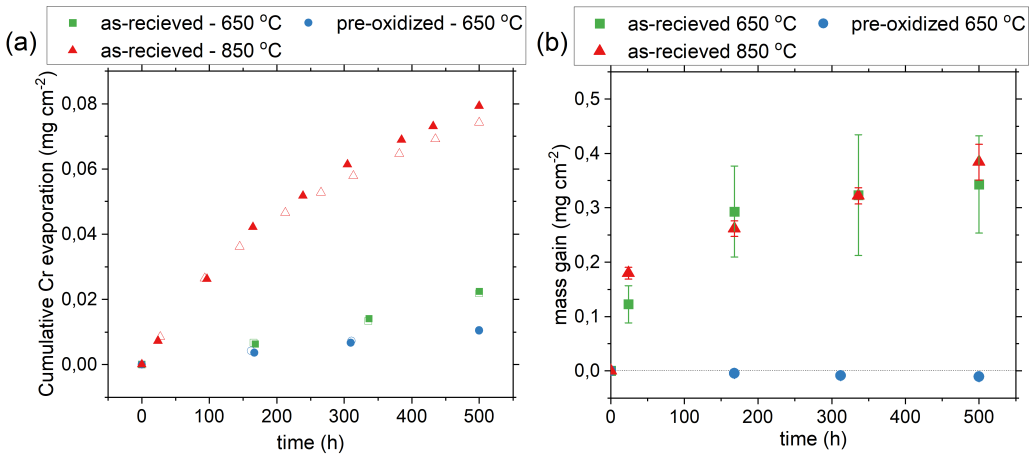

Figure 6.29: (a) Cr evaporation and (b) mass gain as a function of time for the as-received and pre-oxidised Alloy 600 exposed at 650°C and the as-received Alloy 600 exposed at 850°C for 500 h in air + 3% H_2O. The open and filled symbols represent two individual exposures.

The cross-sections of Alloy 600 at 650°C after 500 hours, as shown in Figure 6.30a, revealed a non-uniform oxide scale with thick, non-protective and thin, protective regions. In the regions with a thick non-protective oxide scale, the oxide scale grew both inwards (craters) and outwards (islands) faster than the surrounding area. The surface morphology (inset in Figure 6.30a) showed that the islands were distributed over the entire surface, with varied thicknesses in the range of 1-10 μm. The EDX maps in Figure 6.30 revealed that the craters and the islands have varying local enrichments. Chromium enrichment was observed at the metal-oxide interface, as the inward-growing oxide scale was healed by forming a protective Cr-rich scale. The regions with a thin oxide scale could not be resolved in the SEM. The lack of internal oxidation indicates the presence of a protective oxide scale, which was probably formed due to an enhanced chromium supply in this region. The lack of a continuous protective oxide scale resulted in the higher mass gain observed at 650°C, similar to that seen at 850°C.

The cross-section of Alloy 600 at 850°C after 500 hours, as shown in Figure 6.30b, reveals a non-uniform oxide scale with varying thickness. The oxide scale was thicker

above the alloy grains and thinner above the alloy grain boundaries. This difference in the oxide scale structure is due to the level of Cr diffusion being higher along the alloy grain boundaries than in the bulk in Ni-base alloys [186]. Moreover, the alloy grain boundaries act as preferential nucleation sites for the Cr-rich oxide scale [187]. This resulted in the chromia scale being formed more rapidly on the grain boundaries than in the surrounding area. The formation of the Ni-rich cap layer resulted in a lower Cr evaporation compared to AISI 441 and AISI 444, at the investigated temperatures.

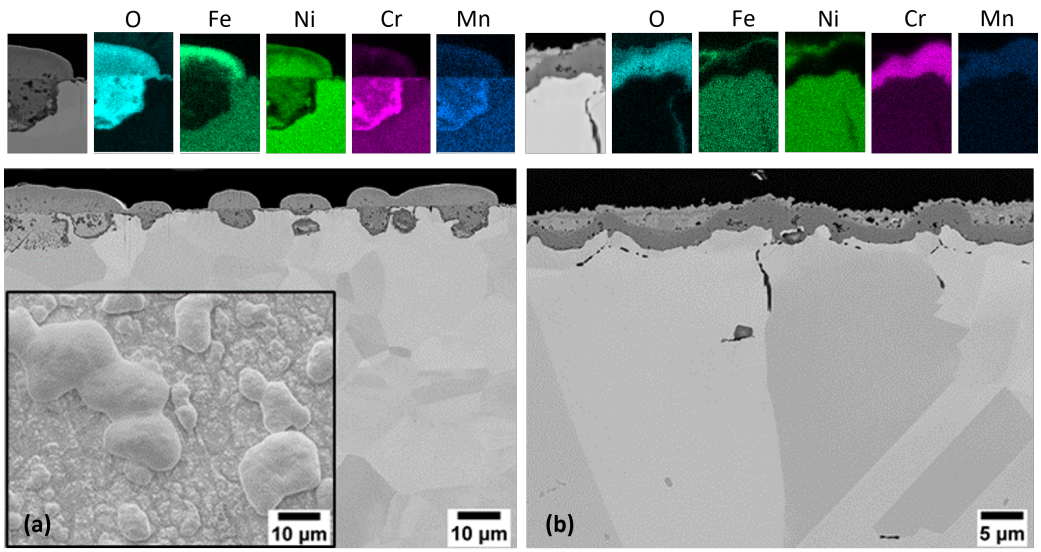

Figure 6.30: SEM cross-sectional micrographs and EDX maps of Alloy 600 exposed at (a) 650°C and (b) 850°C for 500 h in air + 3% H_2O.

After pre-oxidation, the performance of Alloy 600 was improved at 650°C. The pre-oxidised coupons had an oxide scale structure similar to those of the coupons exposed at 850°C. The low corrected mass gain (see Paper VII) on the pre-oxidised coupons was due to the presence of a continuous, protective, chromium-rich oxide scale. The Cr evaporation was lower on the pre-oxidised coupons than on the as-received coupons due to the Ni-rich cap layer formed on the chromia upon pre-oxidation.

6.8.3 Alloy 800H

The Cr evaporation of the chromia-forming austenitic steel, Alloy 800H, shown in Figure 6.31a, was 5-10 times lower than that of AISI 444 or AISI 441 at the respective investigated temperatures. The Cr evaporation at 650°C is 10 times lower than that at 850°C. The pre-oxidised coupons showed similar Cr evaporation as the as-received Alloy 800H at 650°C. Alloy 800H had the highest Cr content among the selected alloys; however, it exhibited the highest mass gains (Figure 6.31b) for the as-received coupons at

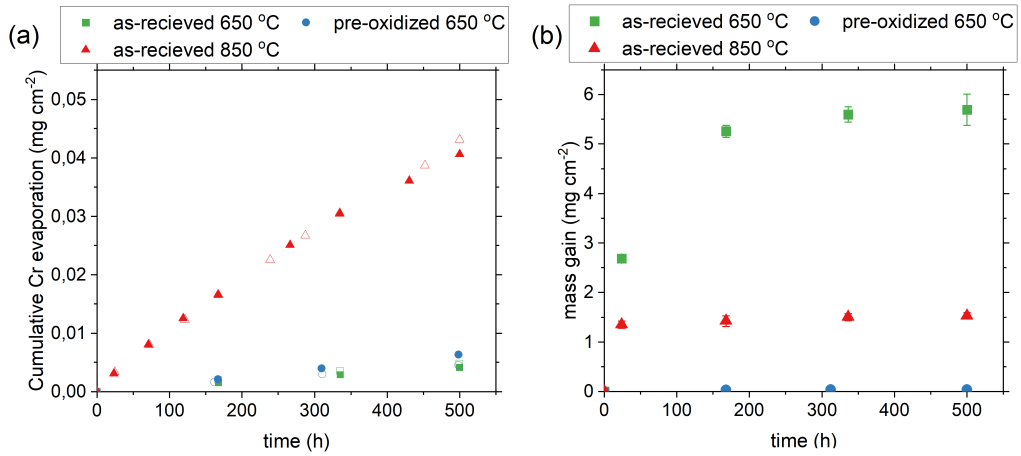

Figure 6.31: (a) Cr evaporation and (b) mass gain as a function of time for the as-received and pre-oxidised Alloy 800H exposed at 650°C and the as-received Alloy 800H exposed at 850°C for 500 h in air + 3% H_2O. The open and filled symbols represent two individual exposures.

both investigated temperatures on the as-received coupons. The as-received Alloy 800H exhibited an inverse temperature behaviour whereby lower mass gains were observed at higher temperatures. The mass gain at 650°C was 4-5 times higher than at 850°C after 500 hours. The higher mass gain indicates the low oxidation resistance at 650°C. However, the mass gain stabilised after 168 hours, revealing a decreased oxidation rate with time.

The cross-section of alloy 800H at 650°C after 500 hours, shown in Figure 6.32a revealed that the oxide scale was continuous and non-uniform, with the thickness varying from 15-70 μm. The oxide scale had both outward- and inward-growing parts with three distinct oxide scales. The protective Cr_2O_3 scale was not formed on Alloy 800H at 650°C during the initial stage, resulting in the formation of fast-growing oxides, explaining the high mass gain. The oxidation proceeded inwards, oxidising Fe, Cr, and Ni due to the lack of a protective scale. The oxide layer healed by forming a Cr-rich oxide layer, inhibiting further rapid inward oxidation. The formation of the protective layer resulted in slower oxidation, as observed in the mass gain after 168 hours in Figure 6.31b. The low Cr evaporation observed at 650°C was due to the thick Cr-free oxide scale, which further limited Cr oxide access to the environment.

The oxide scale structure (Figure 6.32b) at 850°C was similar to that at 650°C. However, it was thinner due to the faster formation of a protective Cr_2O_3 scale at higher temperatures. The oxide scale structures and thicknesses above the alloy grains and alloy grain boundaries were different. Despite having 20% Cr in the steel, the Cr-rich scale was not formed on the surface at 850°C during the initial oxidation. Instead, a $(Fe, Ni)_3O_4$ spinel formed on the surface. This is probably due to the slower Cr diffusion that occurs

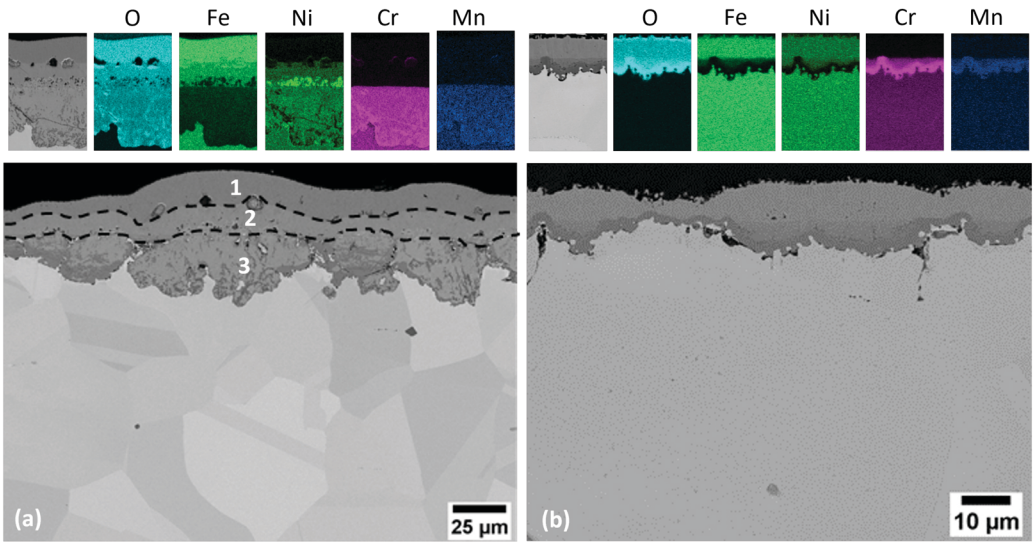

Figure 6.32: SEM cross-sectional micrographs and EDX maps of Alloy 800H exposed at (a) 650°C and (b) 850°C for 500 h in air + 3% H_2O.

in austenitic steels compared to ferritic steels [180]. The oxide scale is thinner above the alloy grain boundaries because Cr diffusion along the grain boundaries is faster than in the bulk [188]. Once a continuous protective Cr scale was formed at the metal-oxide interface, the oxidation rate slowed down, as reflected in the mass gain after 24 hours. The presence of the $(Fe, Ni)_3O_4$ spinel cap layer on the Cr-rich oxide resulted in the lower Cr evaporation observed in Figure 6.31a.

The oxide scale formed upon pre-oxidation resembled the structure of the oxide scale at 850°C; however, the outer spinel layer was thinner because the protective scale formed faster at higher temperatures. Despite the thinner cap layer on the pre-oxidised coupons compared to the as-received coupons, the Cr evaporation was similar at 650°C. This indicates the effectiveness of the $(Fe, Ni)_3O_4$ spinel cap layer at reducing Cr evaporation. The protective oxide scale formed during pre-oxidation resulted in a lower mass gain during subsequent exposure at 650°C.

6.8.4 A197/Kanthal® EF101

The Cr evaporation of the alumina-forming FSS, A197, is shown in Figure 6.33a. It was two orders of magnitude lower than that of AISI 441 or AISI 444, being the lowest of the selected alloys at both temperatures. These results are in agreement with previous studies on the Cr evaporation of alumina-forming alloys [38]. The Cr evaporation at 650°C was 4 times lower than the Cr evaporation at 850°C. The Cr evaporation was similar for the as-received coupons and pre-oxidised coupons. The mass gains of A197,

shown in Figure 6.33b, were extremely low at the investigated temperatures. A197 had the lowest corrected mass gain of the selected alloys at both temperatures, indicating superior oxidation resistance.

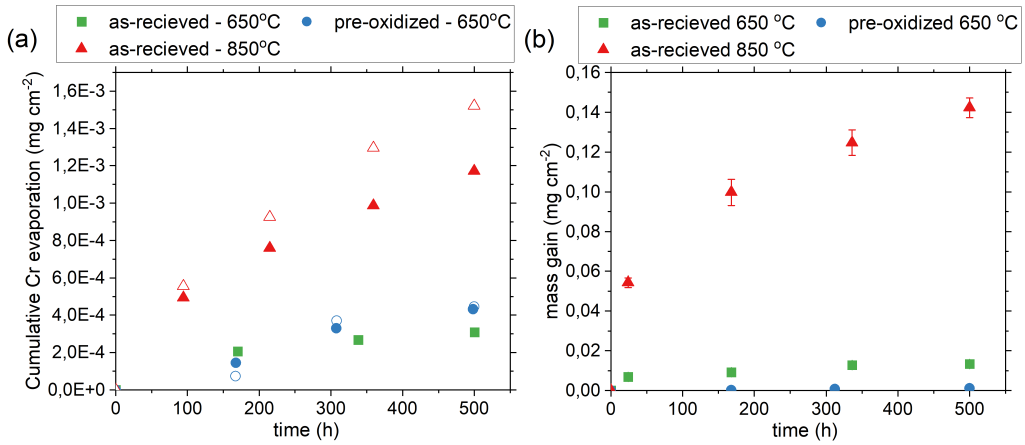

Figure 6.33: (a) Cr evaporation and (b) mass gain as a function of time for the as-received and pre-oxidised A197 exposed at 650°C and the as-received A197 exposed at 850°C for 500 h in air + 3% H_2O. The open and filled symbols represent two individual exposures.

The cross-section of A197 at 650°C after 500 hours, shown in Figure 6.34a, revealed the presence of a continuous protective oxide scale. The oxide scale had a thickness of 50 nm after 500 hours. The oxide scale was too thin for EDX analysis in SEM. However, based on the Cr evaporation and mass gain data, it can be assumed that the oxide scale is an alumina-rich scale. The cross-section of A197 at 850°C after 500 hours, shown in Figure 6.34b, revealed a multi-layered oxide with dense inner and porous outer scales. The oxide scale was mostly uniform, with a thickness of about 500 nm after 500 hours. Reactive element oxides were sporadically observed in the oxide scale, and the oxide scale was thicker in those regions. The EDX maps (Paper VII) showed the presence of an alumina-rich oxide at 850°C. Sand et al. [117] confirmed the presence of mullite ($Al_x(Al_{2+2x}Si_{2+2x})O_{10-x}$) and tridymite ($SiO_2$ polymorph), in addition to α- and γ-alumina scales when A197 was exposed at 800°C in 20% H_2O.

The pre-oxidised A197 showed almost no change in mass when further exposed at 650°C for 500 hours. The Cr evaporation of the as-received and pre-oxidised coupons was similar (Figure 6.33a). This indicates that the oxide scale formed at 650°C is extremely effective at reducing Cr evaporation, similar to the α- and γ-alumina scales. The extremely low Cr evaporation and mass gain make A197 particularly suitable for BOP application.

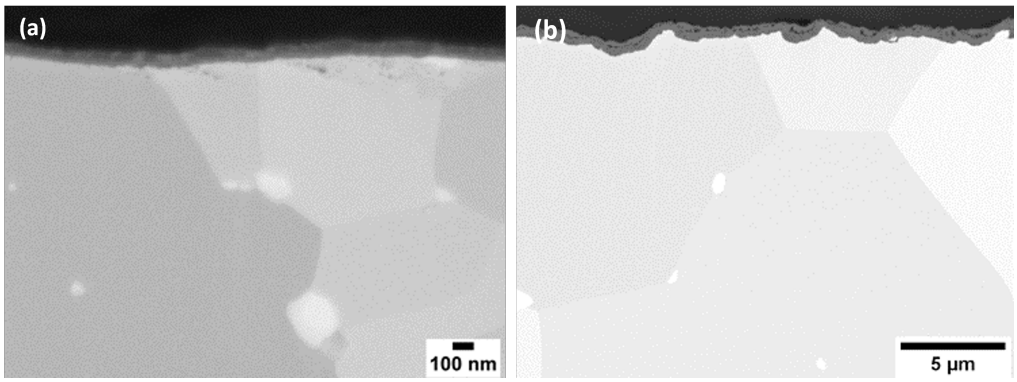

Figure 6.34: SEM cross-sectional micrographs of A197 exposed at (a) 650°C and (b) 850°C for 500 h in air + 3% H_2O.

6.8.5 Comparison of the selected steels

Of the as-received alloys exposed at 650°C, AISI 441 and AISI 444 exhibited the highest Cr evaporation and mass loss after 500 hours. Alloy 600 and Alloy 800H exhibited approximately 3 and 10 times lower Cr evaporation compared to AISI 441 or AISI 444. However, the mass gain of Alloy 800H was very high, indicating inferior oxidation resistance. Alloy 600 and Alloy 800H formed a cap layer on a Cr-rich scale due to inferior oxidation resistance. However, this cap layer helped to reduce Cr evaporation. A197 showed about 100 times lower Cr evaporation than AISI 441 or AISI 444. The mass gain of A197 was the lowest of the selected alloys, indicating superior oxidation resistance. With the exception of A197, all the alloys showed unsatisfactory behaviours in terms of Cr evaporation and oxidation resistance.

In general, the Cr evaporation of the selected alloys was higher at 850°C than at 650°C. Nevertheless, the ranking of the alloys according to Cr evaporation at 850°C was similar to that at 650°C. Of all the alloys that showed a positive mass gain, Alloy 800H had the highest, and A197 had the lowest mass gain. A Ni-rich cap layer was formed on the top of the protective chromia layer on Alloy 800H and Alloy 600. Due to the less effective cap layer on Alloy 600, the Cr evaporation was higher than for Alloy 800H. A197 formed an alumina scale and therefore, had lower Cr evaporation and mass gain.

Pre-oxidation significantly improved the performances of the alloys at 650°C. The Cr evaporation of the pre-oxidised alloys is 30-50% lower than those of the as-received materials, except for A197 and Alloy 800H, which showed similar Cr evaporation under both conditions. The ranking of the pre-oxidised materials with respect to Cr evaporation was similar to that of the as-received materials. Pre-oxidation resulted in significant improvements in the oxidation resistance of Alloy 600 and Alloy 800H. Cost is an important consideration in the selection of materials for BOP components. Alloy 600 is expected to be the most expensive, followed by Alloy 800H and the ferritic steels A197, AISI 441 and

AISI 444. Of the ferritic steels, A197 is expected to be expensive due to having lower production volumes than AISI 441 and AISI 444.

7 Conclusions

This thesis presents cost-effective materials and new coating systems to mitigate the degradation of metallic materials in solid oxide cells. The research focuses primarily on air side atmospheres and includes investigations of the chromium evaporation, oxidation kinetics, micro-structural evolution of the oxide scale, and the area-specific resistances of various steels and coating systems. Some experiments were also carried out under dual-atmosphere conditions. The main findings of these studies are summarised below.

The chromium evaporation and oxidation kinetics of uncoated steels (AISI 409, AISI 430, AISI 441, AISI 444, and Crofer 22 APU) were dissimilar. While the oxide scale thicknesses of these steels varied, the oxide scale structures were similar, with a $(Cr, Mn)_3O_4$ spinel on top and a Cr_2O_3 scale beneath. Once coated with Ce/Co, the Cr evaporation was 60–100 times lower than that for the uncoated steels at 800°C. In addition, all the coated steels showed highly similar oxidation kinetics. The oxide scale structures and thicknesses on the coated steels were similar, with a $(Co, Mn)_3O_4$ spinel on top and a Cr_2O_3 scale beneath. The ASR values of the coated steels were lower than those of the uncoated steels and similar to each other, with the exception of the Ce/Co-coated AISI 430. Moreover, the coated steels showed no dual-atmosphere effect at 800°C. The laboratory studies indicated that the low-cost alternatives performed as well as Crofer 22 APU once coated with Ce/Co, despite the small Cr reservoir.

The oxidation kinetics of Ce/Co-coated steels were highly similar for temperatures in the range of 750°–900°C, except for Ce/Co-coated AISI 430 and AISI 409, which experienced breakaway corrosion at different times above 850°C. The critical Cr concentration for breakaway corrosion, determined on Ce/Co-coated AISI 409, was found to be 10.06 wt%. The lifetimes of Ce/Co-coated AISI 441 and Crofer 22 APU were calculated using the oxidation kinetics and critical Cr content. Furthermore, the influences of the thickness and Cr concentration of the steel on lifetime were analysed.

Adding 10 nm Ce to the coating improved oxidation resistance. However, further increasing the concentration of Ce in the coating did not improve the oxidation performance any further at 800°C. To understand the mechanism behind the reactive element effect in Ce/Co coating, two sets of coating systems based on Ce/Co were fabricated on Crofer 22 APU. The presence of Ce in the coating, regardless of its position relative to the chromia scale, improved the oxidation resistance. The commonly accepted mechanism by which the reactive elements block the Cr^{3+} ions along the grain boundaries could not explain this behaviour. Instead, a new mechanism is proposed whereby Ce blocks oxygen ion diffusion in the $(Co, Mn)_3O_4$ spinel, thereby improving the oxidation resistance of the steel.

Ce/Co coating has been shown to be very effective in improving the oxidation behaviour of FSS. The Ce/Co (CeCoPVD) coating was compared to other MCO coatings deposited

using spray pyrolysis (MCOCeSP), APS (MCFAPS), and ultrasonic spray coating (MCOCeUSC) on Crofer 22 APU. Although the thicknesses of the coatings differed significantly (0.6-100 μm), the Cr evaporation behaviours of the coated steels were similar, and significantly lower than the uncoated steels. The chromia scales thicknesses were similar except for MCOCeUSC, which had a thinner chromia scale after 3,000 hours due to pre-oxidation. The coated steels showed lower ASR values than the uncoated steel, and this held true irrespective of the deposition method, thickness or composition of the coating.

To replace the Co in Ce/Co coatings, a new coating system that uses Ce/FeNi is developed. The Ce/FeNi-coated AISI 441 exhibited lower oxidation kinetics and lower ASR than the Ce/Co-coated AISI 441. However, the Ce/FeNi-coated AISI 441 showed higher Cr evaporation than the Ce/Co-coated AISI 441, but lower than the uncoated steel in air + 3%H_2O. Since the Cr evaporation is not a significant issue under SOEC conditions, Ce/FeNi coatings appear to be effective.

To identify potential BOP materials from a wide range of alloys, four different groups of materials were investigated at 650°C and 850°C. Their behaviours were related to the corresponding oxide scale microstructures. The alumina-forming alloy A197 showed the formation of a slow-growing protective scale with excellent chromium retention properties at 650°C and an alumina scale at 850°C. Due to its high oxidation resistance and low chromium evaporation, A197 is a highly recommended material for BOP components. Alloy 800H showed lower chromium evaporation than the other alloys under all exposure conditions, owing to the formation of a cap layer on top of the Cr-rich scale. At 650°C, its oxidation resistance was poor, however, pre-oxidation improved its performance. The chromia-forming Ni-base material, Alloy 600, showed intermediate performance among the selected alloys. The chromia-forming ferritic steels, 441 and 444, showed similar chromium evaporation at both temperatures and higher levels than those of the other selected alloys, making them particularly unsuitable for specific BOP components.

8 Outlook

Future research on interconnect materials should be focussed on the following:

- Ce/Co-coated steels exhibit thicker Cr-rich scales on the fuel side than on the air side. Hence, coatings must be developed that reduce Cr consumption on the fuel side. This is especially important for SOEC, where high steam concentrations are expected on the fuel side.
- The lifetime model should be adjusted for lower temperatures and cases with a Cr-depletion profile in the steel.
- Pre-oxidation significantly influenced the oxidation kinetics of MCOCeUSC-coated Crofer 22 APU. Since stacks are typically conditioned at high temperatures, usually 100° - 250°C above the operating temperatures, it is crucial to understand the influence of pre-oxidation on the oxidation behaviour and lifetime of the coated steels.
- Further research is needed to distinguish between the classical explanation for the reactive element effect and that observed for Ce/Co coatings.
- The Ce/FeNi coating system seems promising. However, further investigations are needed to understand the effect of coating thickness, the ability of the coating to heal after stamping inside the stack, and its long-term stability and performances.

Future research on BOP materials should focus on understanding the oxidation behaviour of the alloys under fuel and dual-atmosphere conditions. Other factors relevant to the material selection for BOP components, such as durability, long-term deformation, and ease of welding, should be investigated.

Bibliography

[1] Hannah Ritchie, Max Roser, and Pablo Rosado. "CO and Greenhouse Gas Emissions". In: *Our World in Data* (2020).

[2] David I Armstrong McKay et al. "Exceeding 1.5°C global warming could trigger multiple climate tipping points". In: *Science* 377.6611 (Mar. 2023), eabn7950. DOI: 10.1126/science.abn7950. URL: https://doi.org/10.1126/science.abn7950.

[3] P Friedlingstein et al. "Global Carbon Budget 2022". In: *Earth Syst. Sci. Data* 14.11 (Nov. 2022), pp. 4811–4900. ISSN: 1866-3516. DOI: 10.5194/essd-14-4811-2022. URL: https://essd.copernicus.org/articles/14/4811/2022/https://essd.copernicus.org/articles/14/4811/2022/essd-14-4811-2022.pdf.

[4] Hannah Ritchie, Max Roser, and Pablo Rosado. "Energy". In: *Our World in Data* (2022).

[5] Tianmei Chen et al. "Applications of Lithium-Ion Batteries in Grid-Scale Energy Storage Systems". In: *Transactions of Tianjin University* 26.3 (June 2020), pp. 208–217. ISSN: 1006-4982. DOI: 10.1007/s12209-020-00236-w. URL: https://doi.org/10.1007/s12209-020-00236-whttp://link.springer.com/10.1007/s12209-020-00236-w.

[6] Xi Yang et al. "Breaking the hard-to-abate bottleneck in China's path to carbon neutrality with clean hydrogen". In: *Nature Energy* 7.10 (2022), pp. 955–965. ISSN: 2058-7546. DOI: 10.1038/s41560-022-01114-6. URL: https://doi.org/10.1038/s41560-022-01114-6.

[7] *IEA (2022), Hydrogen.* 2022. URL: https://www.iea.org/reports/hydrogen.

[8] Günther G Scherer. "Fuel Cell Types and Their Electrochemistry". In: *Fuel Cells and Hydrogen Production*. Ed. by Timothy E Lipman and Adam Z Weber. New York, NY: Springer New York, 2019, pp. 83–98. ISBN: 978-1-4939-7789-5. DOI: 10.1007/978-1-4939-7789-5{_}132. URL: https://doi.org/10.1007/978-1-4939-7789-5_132http://link.springer.com/10.1007/978-1-4939-7789-5_132.

[9] Arnab Choudhury, H. Chandra, and A. Arora. *Application of solid oxide fuel cell technology for power generation - A review.* Apr. 2013. DOI: 10.1016/j.rser.2012.11.031.

[10] *Manufacturing Cost Analysis of 100 and 250 kW Fuel Cell Systems for Primary Power and Combined Heat and Power Applications.* Tech. rep. Battelle Memorial Institute, 2016, pp. 1–289. URL: https://www.energy.gov/sites/prod/files/2016/07/f33/fcto_battelle_mfg_cost_analysis_pp_chp_fc_systems.pdf.

[11] *Manufacturing Cost Analysis of 1, 5, 10 and 25 kW Fuel Cell Systems for Primary Power and Combined Heat and Power Applications.* Tech. rep. Battelle Memorial Institute, 2017, p. 293. URL: https://www.energy.gov/sites/prod/files/

2018/02/f49/fcto_battelle_mfg_cost_analysis_1_to_25kw_pp_chp_fc_systems_jan2017_0.pdf.

[12] Robert Steinberger-Wilckens. "Introduction to Fuel Cell Basics". In: *Advances in Medium and High Temperature Solid Oxide Fuel Cell Technology*. Ed. by Marta Boaro and Aricò Antonino Salvatore. Springer International Publishing, 2017, pp. 1–29. ISBN: 978-3-319-46145-8. DOI: https://doi.org/10.1007/978-3-319-46146-5.

[13] Timothy E. Lipman and Adam Z. Weber, eds. *Fuel cells and hydrogen production*. Springer-Verlag New York, 2019, pp. 1–1179. ISBN: 978-1-4939-7790-1.

[14] John Bøgild Hansen. "Solid Oxide Fuel Cells - Marketing Issues". In: *Fuel Cells*. Ed. by Klaus-Dieter Kreuer. New York, NY: Springer New York, 2013, pp. 1–7. ISBN: 978-1-4614-5784-8. DOI: 10.1007/978-1-4614-5785-5. URL: http://link.springer.com/10.1007/978-1-4614-5785-5.

[15] A. Boudghene Stambouli and E. Traversa. "Solid oxide fuel cells (SOFCs): a review of an environmentally clean and efficient source of energy". In: *Renewable and Sustainable Energy Reviews* 6.5 (Oct. 2002), pp. 433–455. ISSN: 1364-0321. DOI: 10.1016/S1364-0321(02)00014-X.

[16] Subhash C. Singhal. "Solid Oxide Fuel Cells: Past, Present and Future". In: *Green Energy and Technology*. Ed. by John T.S. Irvine and Paul Connor. Vol. 55. Springer Verlag, 2013, pp. 1–23. ISBN: 978-1-4471-4456-4. DOI: 10.1007/978-1-4471-4456-4{_}1.

[17] Keith Scott. "Introduction to Electrolysis, Electrolysers and Hydrogen Production". In: *Electrochemical Methods for Hydrogen Production*. Ed. by Keith Scott. The Royal Society of Chemistry, Nov. 2019, p. 0. ISBN: 978-1-78801-378-9. DOI: 10.1039/9781788016049-00001. URL: https://doi.org/10.1039/9781788016049-00001.

[18] S Y Gómez and D Hotza. "Chapter 5 Solid Oxide Electrolysers". In: *Electrochemical Methods for Hydrogen Production*. The Royal Society of Chemistry, 2020, pp. 136–179. ISBN: 978-1-78801-378-9. DOI: 10.1039/9781788016049-00136. URL: http://dx.doi.org/10.1039/9781788016049-00136.

[19] R Mark Ormerod. "Solid oxide fuel cells". In: *Chemical Society Reviews* 32.1 (2003), pp. 17–28. ISSN: 0306-0012. DOI: 10.1039/B105764M.

[20] Aziz Nechache and Stéphane Hody. "Alternative and innovative solid oxide electrolysis cell materials: A short review". In: *Renewable and Sustainable Energy Reviews* 149 (Oct. 2021), p. 111322. ISSN: 1364-0321. DOI: https://doi.org/10.1016/j.rser.2021.111322. URL: https://www.sciencedirect.com/science/article/pii/S1364032121006080https://linkinghub.elsevier.com/retrieve/pii/S1364032121006080.

[21] Nguyen Q Minh. "Ceramic Fuel Cells". In: *Journal of the American Ceramic Society* 76.3 (Mar. 1993), pp. 563–588. ISSN: 0002-7820. DOI: https://doi.org/10.1111/j.1151-2916.1993.tb03645.x.

[22] A. Tsoga et al. "Gadolinia-doped ceria and yttria stabilized zirconia interfaces: regarding their application for SOFC technology". In: *Acta Materialia* 48.18-19 (Dec. 2000), pp. 4709–4714. ISSN: 1359-6454. DOI: 10.1016/S1359-6454(00)00261-5.

[23] Kevin Kendall and Michaela Kendall. *High-temperature Solid Oxide Fuel Cells for the 21st Century*. Elsevier, 2016. ISBN: 9780124104532.

[24] S Badwal et al. "Review of Progress in High Temperature Solid Oxide Fuel Cells". In: *ChemInform* 46 (2014).

[25] M. Cassidy et al. "Anodes". In: *High-Temperature Solid Oxide Fuel Cells for the 21st Century: Fundamentals, Design and Applications: Second Edition*. Academic Press, Jan. 2016, pp. 133–160. ISBN: 978-0-12-410453-2. DOI: 10.1016/B978-0-12-410453-2.00005-1.

[26] Quanrong Fu et al. "Performance degradation prediction of direct internal reforming solid oxide fuel cell due to Ni-particle coarsening in composite anode". In: *Energy Conversion and Management* 233 (2021), p. 113902. ISSN: 0196-8904. DOI: https://doi.org/10.1016/j.enconman.2021.113902. URL: https://www.sciencedirect.com/science/article/pii/S0196890421000790.

[27] Y. Ji, J. A. Kilner, and M. F. Carolan. "Electrical properties and oxygen diffusion in yttria-stabilised zirconia (YSZ)–La0.8Sr0.2MnO3±δ (LSM) composites". In: *Solid State Ionics* 176.9-10 (Mar. 2005), pp. 937–943. ISSN: 0167-2738. DOI: 10.1016/J.SSI.2004.11.019.

[28] L. Niewolak, F. Tietz, and W. J. Quadakkers. "Interconnects". In: *High-Temperature Solid Oxide Fuel Cells for the 21st Century: Fundamentals, Design and Applications: Second Edition*. Academic Press, Jan. 2016, pp. 195–254. ISBN: 978-0-12-410453-2. DOI: 10.1016/B978-0-12-410453-2.00007-5.

[29] Minoru Suzuki. *Development status and future prospects for residential and commercial use of SOFC systems*. Tech. rep. URL: https://www.gas.or.jp/en/newsletter/images/22/dl/pdf01.pdf.

[30] Jeffrey W. Fergus. "Lanthanum chromite-based materials for solid oxide fuel cell interconnects". In: *Solid State Ionics* 171.1-2 (June 2004), pp. 1–15. ISSN: 01672738. DOI: 10.1016/j.ssi.2004.04.010.

[31] José Luis Córdova and Hooshang Heshmat. *Development of a Ceramic Heat Exchanger for Application as Solid Oxide Fuel Cell Cathode Air Preheater*. June 2016. DOI: 10.1115/POWER2016-59333.

[32] David J. Young. "Enabling Theory". In: *High Temperature Oxidation and Corrosion of Metals* (Jan. 2016), pp. 31–84. DOI: 10.1016/B978-0-08-100101-1.00002-9.

[33] P. Kofstad. *High Temperature Corrosion*. 1st ed. Elsevier Applied Science Publishers Ltd., 1988. ISBN: 1-85166-154-9.

[34] Neil Birks, Gerald H Meier, and Frederick S Pettit. *Introduction to the High Temperature Oxidation of Metals*. 2nd ed. Cambridge: Cambridge University Press, 2006. ISBN: 9780521480420. DOI: DOI:10.1017/CBO9781139163903.

[35] Carl Wagner. "Beitrag zur Theorie des Anlaufvorgangs". In: *Zeitschrift für Physikalische Chemie* 21B.1 (Feb. 1933), pp. 25–41. ISSN: 2196-7156. DOI: 10.1515/ZPCH-1933-2105.

[36] David J. Young. *High temperature oxidation and corrosion of metals*. 2nd ed. Elsevier Ltd., 2016, p. 733. ISBN: 978-0-08-100101-1. DOI: https://doi.org/10.1016/C2014-0-00259-6.

[37] Paul E Blackburn, Michael Hoch, and Herrick L Johnston. "The Vaporization of Molybdenum and Tungsten Oxides". In: *The Journal of Physical Chemistry* 62.7 (July 1958), pp. 769–773. ISSN: 0022-3654. DOI: 10.1021/j150565a001.

[38] M. Stanislowski et al. "Reduction of chromium vaporization from SOFC interconnectors by highly effective coatings". In: *Journal of Power Sources* 164.2 (Feb. 2007), pp. 578–589. ISSN: 03787753. DOI: 10.1016/j.jpowsour.2006.08.013.

[39] L. Mikkelsen, S. Linderoth, and J. B. Bilde-Sørensen. "The effect of silicon addition on the high temperature oxidation of a Fe-Cr alloy". In: *Materials Science Forum*. Vol. 461-464. I. Trans Tech Publications Ltd, 2004, pp. 117–122. DOI: 10.4028/www.scientific.net/msf.461-464.117.

[40] D. Caplan and M. Cohen. "The Volatilization of Chromium Oxide". In: *Journal of The Electrochemical Society* 108.5 (1961), p. 438. DOI: 10.1149/1.2428106.

[41] Elizabeth J. Opila et al. "Theoretical and Experimental Investigation of the Thermochemistry of CrO 2 (OH) 2 (g)". In: *The Journal of Physical Chemistry A* 111.10 (Mar. 2007), pp. 1971–1980. ISSN: 1089-5639. DOI: 10.1021/jp0647380. URL: https://pubs.acs.org/doi/10.1021/jp0647380.

[42] Bartley B. Ebbinghaus. "Thermodynamics of gas phase chromium species: The chromium oxides, the chromium oxyhydroxides, and volatility calculations in waste incineration processes". In: *Combustion and Flame* 93.1-2 (Apr. 1993), pp. 119–137. ISSN: 0010-2180. DOI: 10.1016/0010-2180(93)90087-J.

[43] C S Tedmon. "The Effect of Oxide Volatilization on the Oxidation Kinetics of Cr and Fe-Cr Alloys". In: *Journal of The Electrochemical Society* 113.8 (1966), p. 766. ISSN: 0013-4651. DOI: 10.1149/1.2424115.

[44] Bagas Pujilaksono et al. "Paralinear oxidation of chromium in O 2 + H 2O environment at 600-700 °c". In: *Oxidation of Metals* 70.3-4 (Oct. 2008), pp. 163–188. ISSN: 0030770X. DOI: 10.1007/s11085-008-9114-1.

[45] Hai V Pham, Masaki Kurata, and Martin Steinbrueck. *Steam Oxidation of Silicon Carbide at High Temperatures for the Application as Accident Tolerant Fuel Cladding, an Overview*. 2021. DOI: 10.3390/thermo1020011.

[46] Roger C. Reed. *The Superalloys*. Cambridge: Cambridge University Press, 2006. ISBN: 9780511541285. DOI: 10.1017/CBO9780511541285.

[47] W. Z. Zhu and S. C. Deevi. "Opportunity of metallic interconnects for solid oxide fuel cells: A status on contact resistance". In: *Materials Research Bulletin* 38.6 (May 2003), pp. 957–972. ISSN: 00255408. DOI: 10.1016/S0025-5408(03)00076-X.

[48] Jeffrey Fergus et al. "Interconnects". In: *Solid Oxide Fuel Cells - Materials Properties and Performance*. CRC Press, Apr. 2016, pp. 195–228. ISBN: 9780429143649. DOI: 10.1201/9781420088847-8.

[49] Angeliki Brouzgou, Anatoly Demin, and Panagiotis Tsiakaras. "Interconnects for Solid Oxide Fuel Cells". In: *Advances in Medium and High Temperature Solid Oxide Fuel Cell Technology*. Ed. by Marta Boaro and Aricò Antonino Salvatore. Cham: Springer International Publishing, 2017, pp. 119–153. ISBN: 978-3-319-46146-5. DOI: 10.1007/978-3-319-46146-5.

[50] San Ping Jiang and Xinbing Chen. "Chromium deposition and poisoning of cathodes of solid oxide fuel cells - A review". In: *International Journal of Hydrogen Energy*

39.1 (Jan. 2014), pp. 505–531. ISSN: 03603199. DOI: 10.1016/j.ijhydene.2013.10.042.

[51] E. Konysheva et al. “Chromium vaporization of the ferritic steel Crofer22APU and ODS Cr5Fe1Y2O3 alloy”. In: *Journal of Materials Science* 42.14 (July 2007), pp. 5778–5784. ISSN: 00222461. DOI: 10.1007/s10853-006-1194-1.

[52] G. V. Samsonov. “Electrical and Magnetic Properties”. In: *The Oxide Handbook*. Boston, MA: Springer US, 1973, pp. 263–319. DOI: 10.1007/978-1-4615-9597-7{_}5.

[53] Keqin Huang, Peggy Y. Hou, and John B. Goodenough. “Reduced area specific resistance for iron-based metallic interconnects by surface oxide coatings”. In: *Materials Research Bulletin* 36.1-2 (Jan. 2001), pp. 81–95. ISSN: 00255408. DOI: 10.1016/S0025-5408(01)00506-2.

[54] Lauri Holappa. “Secondary Steelmaking”. In: *Treatise on Process Metallurgy*. Vol. 3. Elsevier, Jan. 2014, pp. 301–345. ISBN: 978-0-08-096988-6. DOI: 10.1016/B978-0-08-096988-6.00012-2.

[55] Paul D. Jablonski, Christopher J. Cowen, and John S. Sears. “Exploration of alloy 441 chemistry for solid oxide fuel cell interconnect application”. In: *Journal of Power Sources* 195.3 (Feb. 2010), pp. 813–820. ISSN: 03787753. DOI: 10.1016/j.jpowsour.2009.08.023.

[56] J. Froitzheim et al. “Development of high strength ferritic steel for interconnect application in SOFCs”. In: *Journal of Power Sources* 178.1 (Mar. 2008), pp. 163–173. ISSN: 03787753. DOI: 10.1016/j.jpowsour.2007.12.028.

[57] W.J. Quadakkers et al. “Metallic interconnectors for solid oxide fuel cells – a review”. In: 20.2 (), pp. 115–127. ISSN: 0960-3409.

[58] D. L. Douglass and J. S. Armijo. “The influence of manganese and silicon on the oxidation behavior of Co-20Cr”. In: *Oxidation of Metals* 3.2 (Mar. 1971), pp. 185–202. ISSN: 0030770X. DOI: 10.1007/BF00603486.

[59] Jan Froitzheim. “Ferritic steel interconnectors and their interactions with Ni base anodes in solid oxide fuel cells (SOFC)”. PhD thesis. RWTH Aachen, 2009.

[60] Arve Holt and Per Kofstad. “Electrical conductivity of Cr2O3 doped with TiO2”. In: *Solid State Ionics* 117.1-2 (Feb. 1999), pp. 21–25.

[61] Hyung Suk Seo, Dae Won Yun, and Kyoo Young Kim. “Effect of Ti addition on the electric and ionic property of the oxide scale formed on the ferritic stainless steel for SOFC interconnect”. In: *International Journal of Hydrogen Energy* 37.21 (Nov. 2012), pp. 16151–16160. ISSN: 03603199. DOI: 10.1016/j.ijhydene.2012.08.073.

[62] L. B. Pfeil. *Improvements in heat resistant alloys U.K. Patent no 459848*. 1937.

[63] D P Whittlef and J. Stringer. “Improvements in high temperature oxidation resistance by additions of reactive elements or oxide dispersions”. In: *Philosophical Transactions of the Royal Society of London. Series A, Mathematical and Physical Sciences* 295.1413 (Feb. 1980), pp. 309–329. ISSN: 0080-4614. DOI: 10.1098/rsta.1980.0124.

[64] Bruce A. Pint. *Progress in Understanding the Reactive Element Effect Since the Whittle and Stringer Literature Review*. Tech. rep.

[65] B. A. Pint. "Experimental observations in support of the dynamic-segregation theory to explain the reactive-element effect". In: *Oxidation of Metals* 45.1-2 (1996), pp. 1–37. ISSN: 0030770X. DOI: 10.1007/BF01046818.

[66] P. Y. Hou and J. Stringer. "The effect of reactive element additions on the selective oxidation, growth and adhesion of chromia scales". In: *Materials Science and Engineering: A* 202.1 (Nov. 1995), pp. 1–10. ISSN: 0921-5093. DOI: https://doi.org/10.1016/0921-5093(95)09798-8.

[67] R. Prescott and M. J. Graham. "The formation of aluminum oxide scales on high-temperature alloys". In: *Oxidation of Metals* 38.3-4 (Oct. 1992), pp. 233–254. ISSN: 0030770X. DOI: 10.1007/BF00666913.

[68] John Stringer. "The reactive element effect in high-temperature corrosion". In: *Materials Science and Engineering A* 120-121.PART 1 (Nov. 1989), pp. 129–137. ISSN: 09215093. DOI: 10.1016/0921-5093(89)90730-2.

[69] K. Przybylski, A. J. Garratt-Reed, and G. J. Yurek. "Grain Boundary Segregation of Yttrium in Chromia Scales". In: *Journal of The Electrochemical Society* 135.2 (Feb. 1988), pp. 509–517. ISSN: 0013-4651. DOI: 10.1149/1.2095646.

[70] W. J. Quadakkers et al. "Differences in growth mechanisms of oxide scales formed on ODS and conventional wrought alloys". In: *Oxidation of Metals* 32.1-2 (Aug. 1989), pp. 67–88. ISSN: 0030-770X. DOI: 10.1007/BF00665269. URL: http://link.springer.com/10.1007/BF00665269.

[71] W J Quadakkers et al. "The Effect of Yttria Dispersions on the Growth Mechanisms and Morphology of Chromia and Alumina Scales". In: *The Role of Active Elements in the Oxidation Behaviour of High Temperature Metals and Alloys* (1989), pp. 155–173. DOI: 10.1007/978-94-009-1147-5{_}11. URL: https://link.springer.com/chapter/10.1007/978-94-009-1147-5_11.

[72] Bernard Pieraggi, Robert A Rapp, and John P Hirth. "Role of interface structure and interfacial defects in oxide scale growth". In: *Oxidation of Metals* 44.1 (1995), pp. 63–79. ISSN: 1573-4889. DOI: 10.1007/BF01046723. URL: https://doi.org/10.1007/BF01046723.

[73] A W Funkenbusch, J G Smeggil, and N S Bornstein. "Reactive element-sulfur interaction and oxide scale adherence". In: *Metallurgical Transactions A* 16.6 (1985), pp. 1164–1166. ISSN: 1543-1940. DOI: 10.1007/BF02811687. URL: https://doi.org/10.1007/BF02811687.

[74] D. Wiemer, H. J. Grabke, and H. Viefhaus. "Investigation on the influence of sulfur segregation on the adherence of protective oxide layers on high temperature materials". In: *Fresenius' Journal of Analytical Chemistry 1991 341:5* 341.5 (May 1991), pp. 402–405. ISSN: 1432-1130. DOI: 10.1007/BF00321944. URL: https://link.springer.com/article/10.1007/BF00321944.

[75] D. Naumenko, B. A. Pint, and W. J. Quadakkers. *Current Thoughts on Reactive Element Effects in Alumina-Forming Systems: In Memory of John Stringer*. Aug. 2016. DOI: 10.1007/s11085-016-9625-0.

[76] S. Chevalier. "What did we learn on the reactive element effect in chromia scale since Pfeil's patent?" In: *Materials and Corrosion* 65.2 (Feb. 2014), pp. 109–115. ISSN: 09475117. DOI: 10.1002/maco.201307310.

[77] D. P. Moon. "Role of reactive elements in alloy protection". In: *Materials Science and Technology* 5.8 (Aug. 1989), pp. 754–764. ISSN: 0267-0836. DOI: 10.1179/mst.1989.5.8.754. URL: https://www.tandfonline.com/doi/abs/10.1179/mst.1989.5.8.754http://www.tandfonline.com/doi/full/10.1179/mst.1989.5.8.754.

[78] S. Fontana, S. Chevalier, and G. Caboche. "Metallic interconnects for solid oxide fuel cell: Performance of reactive element oxide coating during 10, 20 and 30 months exposure". In: *Oxidation of Metals* 78.5-6 (Dec. 2012), pp. 307–328. ISSN: 0030770X. DOI: 10.1007/s11085-012-9308-4. URL: https://link.springer.com/article/10.1007/s11085-012-9308-4.

[79] J. G. Grolig, J. Froitzheim, and J. E. Svensson. "Coated stainless steel 441 as interconnect material for solid oxide fuel cells: Oxidation performance and chromium evaporation". In: *Journal of Power Sources* 248 (Feb. 2014), pp. 1007–1013. ISSN: 03787753. DOI: 10.1016/j.jpowsour.2013.08.089.

[80] *High-Temperature Fuel Cell Achieves Lifetime of More Than 11 Years*. Tech. rep. Forschungszentrum Jülich, Feb. 2019. URL: http://www.hpsc-terrsys.de/SharedDocs/Pressemitteilungen/UK/EN/2019/2019-02-07-sofc-en.html.

[81] Nima Shaigan et al. "A review of recent progress in coatings, surface modifications and alloy developments for solid oxide fuel cell ferritic stainless steel interconnects". In: *Journal of Power Sources* 195.6 (Mar. 2010), pp. 1529–1542. ISSN: 03787753. DOI: 10.1016/j.jpowsour.2009.09.069.

[82] Joelle C.W. Mah et al. "Metallic interconnects for solid oxide fuel cell: A review on protective coating and deposition techniques". In: *International Journal of Hydrogen Energy* 42.14 (Apr. 2017), pp. 9219–9229. ISSN: 03603199. DOI: 10.1016/j.ijhydene.2016.03.195. URL: https://linkinghub.elsevier.com/retrieve/pii/S0360319915314610.

[83] K H Tan, H A Rahman, and H Taib. "Coating layer and influence of transition metal for ferritic stainless steel interconnector solid oxide fuel cell: A review". In: *International Journal of Hydrogen Energy* 44.58 (2019), pp. 30591–30605. ISSN: 0360-3199. DOI: https://doi.org/10.1016/j.ijhydene.2019.06.155.

[84] Zhenguo Yang et al. "Conductive protection layers on oxidation resistant alloys for SOFC interconnect applications". In: *Surface and Coatings Technology* 201.7 (Dec. 2006), pp. 4476–4483. ISSN: 0257-8972. DOI: 10.1016/J.SURFCOAT.2006.08.082.

[85] Anthony Petric and Hang Ling. "Electrical conductivity and thermal expansion of spinels at elevated temperatures". In: *Journal of the American Ceramic Society* 90.5 (May 2007), pp. 1515–1520. ISSN: 00027820. DOI: 10.1111/j.1551-2916.2007.01522.x.

[86] Yngve Larring and Truls Norby. "Spinel and Perovskite Functional Layers Between Plansee Metallic Interconnect (Cr-5 wt % Fe-1 wt % Y[sub 2]O[sub 3]) and Ceramic (La[sub 0.85]Sr[sub 0.15])[sub 0.91]MnO[sub 3] Cathode Materials for Solid Oxide Fuel Cells". In: *Journal of The Electrochemical Society* 147.9 (2000), p. 3251. ISSN: 00134651. DOI: 10.1149/1.1393891.

[87] Zhenguo Yang et al. "(Mn,Co)3O4 spinel coatings on ferritic stainless steels for SOFC interconnect applications". In: *International Journal of Hydrogen Energy*

32.16 (Nov. 2007), pp. 3648–3654. ISSN: 0360-3199. DOI: 10.1016/J.IJHYDENE.2006.08.048.

[88] J. Froitzheim et al. "Long term study of Cr evaporation and high temperature corrosion behaviour of Co coated ferritic steel for solid oxide fuel cell interconnects". In: *Journal of Power Sources* 220 (Dec. 2012), pp. 217–227. ISSN: 03787753. DOI: 10.1016/j.jpowsour.2012.06.092.

[89] Belma Talic et al. "Comparison of iron and copper doped manganese cobalt spinel oxides as protective coatings for solid oxide fuel cell interconnects". In: *Journal of Power Sources* 372 (Dec. 2017), pp. 145–156. ISSN: 03787753. DOI: 10.1016/j.jpowsour.2017.10.060.

[90] Carlos Bernuy-Lopez et al. "The Time for Industrialization Has Come: A Pre-Coated Solution for the GW Scale". In: *ECS Transactions* 103.1 (July 2021), pp. 1803–1808. ISSN: 1938-5862. DOI: 10.1149/10301.1803ecst. URL: https://iopscience.iop.org/article/10.1149/10301.1803ecst.

[91] S. Fontana et al. "Metallic interconnects for SOFC: Characterisation of corrosion resistance and conductivity evaluation at operating temperature of differently coated alloys". In: *Journal of Power Sources* 171.2 (Sept. 2007), pp. 652–662. ISSN: 03787753. DOI: 10.1016/j.jpowsour.2007.06.255.

[92] D. E. Alman and P. D. Jablonski. "Effect of minor elements and a Ce surface treatment on the oxidation behavior of an Fe-22Cr-0.5Mn (Crofer 22 APU) ferritic stainless steel". In: *International Journal of Hydrogen Energy* 32.16 (Nov. 2007), pp. 3743–3753. ISSN: 03603199. DOI: 10.1016/j.ijhydene.2006.08.032.

[93] S. Chevalier et al. "The reactive element effect on thermally grown chromia scale residual stress". In: *Materials Science and Engineering A* 343.1-2 (Feb. 2003), pp. 257–264. ISSN: 09215093. DOI: 10.1016/S0921-5093(02)00359-3.

[94] Jan Gustav Grolig, Jan Froitzheim, and Jan Erik Svensson. "Effect of Cerium on the Electrical Properties of a Cobalt Conversion Coating for Solid Oxide Fuel Cell Interconnects - A Study Using Impedance Spectroscopy". In: *Electrochimica Acta* 184 (Dec. 2015), pp. 301–307. ISSN: 00134686. DOI: 10.1016/j.electacta.2015.10.111.

[95] S. Canovic et al. "Oxidation of Co- and Ce-nanocoated FeCr steels: A microstructural investigation". In: *Surface and Coatings Technology* 215 (Jan. 2013), pp. 62–74. ISSN: 02578972. DOI: 10.1016/j.surfcoat.2012.08.096.

[96] T. Brylewski et al. "Influence of Gd deposition on the oxidation behavior and electrical properties of a layered system consisting of Crofer 22 APU and MnCo2O4 spinel". In: *International Journal of Hydrogen Energy* 46.9 (Feb. 2021), pp. 6775–6791. ISSN: 03603199. DOI: 10.1016/j.ijhydene.2020.11.169. URL: https://linkinghub.elsevier.com/retrieve/pii/S0360319920344153.

[97] Jan Froitzheim and Jan-Erik Svensson. *Multifunctional Nano-Coatings for SOFC Interconnects*. Apr. 2011. DOI: 10.1149/1.3570248.

[98] Wei Qu et al. "Yttrium, cobalt and yttrium/cobalt oxide coatings on ferritic stainless steels for SOFC interconnects". In: *Journal of Power Sources* 157.1 (June 2006), pp. 335–350. ISSN: 03787753. DOI: 10.1016/j.jpowsour.2005.07.052.

[99] Anders Harthøj, Tobias Holt, and Per Møller. "Oxidation behaviour and electrical properties of cobalt/cerium oxide composite coatings for solid oxide fuel cell

interconnects". In: *Journal of Power Sources* 281 (May 2015), pp. 227–237. ISSN: 03787753. DOI: 10.1016/j.jpowsour.2015.01.128.

[100] Mareddy Reddy and Jan Froitzheim. *Report on chemical stability of the coated interconnects*. Tech. rep. 06. 2020, pp. 1–17. URL: https://ec.europa.eu/research/participants/documents/downloadPublic?documentIds=080166e5d67d5ca9&appId=PPGMS.

[101] Jan Gustav Grolig, Jan Froitzheim, and Jan Erik Svensson. "Coated stainless steel 441 as interconnect material for solid oxide fuel cells: Evolution of electrical properties". In: *Journal of Power Sources* 284 (June 2015), pp. 321–327. ISSN: 03787753. DOI: 10.1016/j.jpowsour.2015.03.029.

[102] Claudia Goebel et al. "Long-term (4 year) degradation behavior of coated stainless steel 441 used for solid oxide fuel cell interconnect applications". In: *Journal of Power Sources* 449 (Feb. 2020). ISSN: 03787753. DOI: 10.1016/j.jpowsour.2019.227480.

[103] Hannes Falk-Windisch et al. "Chromium vaporization from mechanically deformed pre-coated interconnects in Solid Oxide Fuel Cells". In: *Journal of Power Sources* 297 (Aug. 2015), pp. 217–223. ISSN: 03787753. DOI: 10.1016/j.jpowsour.2015.07.085.

[104] H. E. Evans, A. T. Donaldson, and T. C. Gilmour. "Mechanisms of Breakaway Oxidation and Application to a Chromia-Forming Steel". In: *Oxidation of Metals 1999 52:5* 52.5 (1999), pp. 379–402. ISSN: 1573-4889. DOI: 10.1023/A:1018855914737. URL: https://link.springer.com/article/10.1023/A:1018855914737.

[105] I Gurrappa et al. "Factors governing breakaway oxidation of FeCrAl-based alloys". In: *Materials and Corrosion* 51.4 (Apr. 2000), pp. 224–235. ISSN: 0947-5117. DOI: 10.1002/(SICI)1521-4176(200004)51:4<224::AID-MACO224>3.0.CO;2-B. URL: https://doi.org/10.1002/(SICI)1521-4176(200004)51:4%3C224::AID-MACO224%3E3.0.COhttp://2-bhttps://onlinelibrary.wiley.com/doi/10.1002/(SICI)1521-4176(200004)51:4%3C224::AID-MACO224%3E3.0.CO;2-B.

[106] P. Huczkowski et al. "Effect of component thickness on lifetime and oxidation rate of chromia forming ferritic steels in low and high pO 2 environments". In: *Materials at High Temperatures* 22.3-4 (Jan. 2005), pp. 253–262. ISSN: 0960-3409. DOI: 10.1179/mht.2005.029. URL: https://doi.org/10.1179/mht.2005.029http://www.tandfonline.com/doi/full/10.1179/mht.2005.029.

[107] Anton Chyrkin et al. "Oxidation Limited Lifetime of Ni-Base Metal Foams in the Temperature Range 700–900°C". In: *Advanced Engineering Materials* 12.9 (Sept. 2010), pp. 873–883. ISSN: 1438-1656. DOI: https://doi.org/10.1002/adem.201000139. URL: https://doi.org/10.1002/adem.201000139.

[108] D. Koszelow et al. "High temperature corrosion evaluation and lifetime prediction of porous Fe22Cr stainless steel in air in temperature range 700–900 °C". In: *Corrosion Science* 189 (Aug. 2021), p. 109589. ISSN: 0010-938X. DOI: 10.1016/J.CORSCI.2021.109589.

[109] Michael C. Tucker. "Progress in metal-supported solid oxide electrolysis cells: A review". In: *International Journal of Hydrogen Energy* 45.46 (Sept. 2020), pp. 24203–24218. ISSN: 0360-3199. DOI: 10.1016/J.IJHYDENE.2020.06.300.

[110] P Huczkowski et al. “Oxidation Induced Lifetime Limits of Chromia Forming Ferritic Interconnector Steels”. In: *Journal of Fuel Cell Science and Technology* 1.1 (Nov. 2004), pp. 30–34. ISSN: 1550-624X. DOI: 10.1115/1.1782925. URL: https://doi.org/10.1115/1.1782925https://asmedigitalcollection.asme.org/electrochemical/article/1/1/30/463119/Oxidation-Induced-Lifetime-Limits-of-Chromia.

[111] M. Schütze, D. Renusch, and M. Schorr. “Chemical-mechanical failure of oxide scales on 9% Cr steels in air with H2O”. In: *http://dx.doi.org/10.1179/mht.2005.013* 22.1-2 (2014), pp. 113–120. DOI: 10.1179/MHT.2005.013. URL: https://www.tandfonline.com/doi/abs/10.1179/mht.2005.013.

[112] D J Young, A Chyrkin, and W J Quadakkers. “A Simple Expression for Predicting the Oxidation Limited Life of Thin Components Manufactured from FCC High Temperature Alloys”. In: *Oxidation of Metals* 77.5 (2012), pp. 253–264. ISSN: 1573-4889. DOI: 10.1007/s11085-012-9283-9. URL: https://doi.org/10.1007/s11085-012-9283-9.

[113] M J Bennett et al. “The Oxidation Behaviour of the Commercial FeCrAlRE Alloys Aluchrom YHf and Kanthal AF Foils in Air at 800°-950°C”. In: *Materials Science Forum* 461-464 (2004), pp. 463–472. ISSN: 1662-9752. DOI: 10.4028/www.scientific.net/MSF.461-464.463. URL: https://www.scientific.net/MSF.461-464.463.

[114] W J Quadakkers et al. “Growth Rates of Alumina Scales on Fe–Cr–Al Alloys”. In: *Oxidation of Metals* 61.1 (2004), pp. 17–37. ISSN: 1573-4889. DOI: 10.1023/B:OXID.0000016274.78642.ae. URL: https://doi.org/10.1023/B:OXID.0000016274.78642.ae.

[115] W J Quadakkers and K Bongartz. “The prediction of breakaway oxidation for alumina forming ODS alloys using oxidation diagrams”. In: *Materials and Corrosion* 45.4 (Apr. 1994), pp. 232–241. ISSN: 0947-5117. DOI: https://doi.org/10.1002/maco.19940450404. URL: https://doi.org/10.1002/maco.19940450404.

[116] Brian Gleeson. “High-Temperature Corrosion of Metallic Alloys and Coatings”. In: *Materials Science and Technology: A Comprehensive Treatment*. Mar. 2000, pp. 173–228. ISBN: 9783527619306. DOI: https://doi.org/10.1002/9783527619306.ch14. URL: https://doi.org/10.1002/9783527619306.ch14.

[117] T. Sand et al. “Effective Reduction of Chromium-oxy-hydroxide Evaporation from Ni-Base Alloy 690”. In: *Oxidation of Metals* 92.3-4 (Oct. 2019), pp. 259–279. ISSN: 15734889. DOI: 10.1007/s11085-019-09935-9.

[118] R. Sachitanand et al. “Coatings for SOFC Interconnects in Fuel Side Environments”. In: *ECS Transactions* 68.1 (July 2015), pp. 1575–1580. ISSN: 1938-6737. DOI: 10.1149/06801.1575ecst.

[119] Hannes Falk-Windisch, Jan Erik Svensson, and Jan Froitzheim. “The effect of temperature on chromium vaporization and oxide scale growth on interconnect steels for Solid Oxide Fuel Cells”. In: *Journal of Power Sources* 287 (Aug. 2015), pp. 25–35. ISSN: 03787753. DOI: 10.1016/j.jpowsour.2015.04.040.

[120] Brian Gleeson and Bing Tao Li. “Cyclic Oxidation of Chromia-Scale Forming Alloys: Lifetime Prediction and Accounting for the Effects of Major and Minor Alloying Additions”. In: *Materials Science Forum* 461-464 (2004), pp. 427–438.

ISSN: 1662-9752. DOI: 10.4028/www.scientific.net/MSF.461-464.427. URL: https://www.scientific.net/MSF.461-464.427.

[121] W.Joe Quadakkers et al. "Why the Growth Rates of Alumina and Chromia Scales on Thin Specimens Differ from those on Thick Specimens". In: *Materials Science Forum* 595-598 (2008), pp. 1111–1118. ISSN: 1662-9752. DOI: 10.4028/www.scientific.net/MSF.595-598.1111. URL: https://www.scientific.net/MSF.595-598.1111.

[122] Rakshith Sachitanand et al. "Evaluation of the oxidation and Cr evaporation properties of selected FeCr alloys used as SOFC interconnects". In: *International Journal of Hydrogen Energy* 38.35 (Nov. 2013), pp. 15328–15334. ISSN: 03603199. DOI: 10.1016/j.ijhydene.2013.09.044.

[123] Arve Holt and Per Kofstad. "Electrical conductivity and defect structure of Cr2O3. I. High temperatures (>1000°C)". In: *Solid State Ionics* 69.2 (1994), pp. 127–136. ISSN: 0167-2738. DOI: https://doi.org/10.1016/0167-2738(94)90401-4.

[124] Arve Holt and Per Kofstad. "Electrical conductivity and defect structure of Cr2O3. II. Reduced temperatures (<1000°C)". In: *Solid State Ionics* 69.2 (1994), pp. 137–143. ISSN: 0167-2738. DOI: https://doi.org/10.1016/0167-2738(94)90402-2.

[125] L. Latu-Romain et al. "Duplex n- and p-Type Chromia Grown on Pure Chromium: A Photoelectrochemical and Microscopic Study". In: *Oxidation of Metals* 86.5 (Sept. 2016), pp. 497–509. ISSN: 1573-4889. DOI: 10.1007/s11085-016-9648-6.

[126] L. Latu-Romain et al. "The Role of Oxygen Partial Pressure on the Nature of the Oxide Scale on a NiCr Model Alloy". In: *Oxidation of Metals* 88.3 (Nov. 2017), pp. 481–493. ISSN: 1573-4889. DOI: 10.1007/s11085-016-9670-8.

[127] H. Nagai, T. Fujikawa, and K. Shoji. "Electrical Conductivity of Cr2O3 Doped with La2O3, Y2O3 and NiO". In: *Transactions of the Japan Institute of Metals* 24.8 (1983), pp. 581–588.

[128] Arve Holt and Per Kofstad. "Electrical conductivity and defect structure of Mg-doped Cr2O3". In: *Solid State Ionics* 100.3-4 (Oct. 1997), pp. 201–209. ISSN: 0167-2738. DOI: 10.1016/S0167-2738(97)00352-4.

[129] P. Huczkowski et al. "Growth mechanisms and electrical conductivity of oxide scales on ferritic steels proposed as interconnect materials for SOFC's". In: *Fuel Cells* 6.2 (Apr. 2006), pp. 93–99. ISSN: 16156846. DOI: 10.1002/fuce.200500110.

[130] Julian A. Crawford and Robert W. Vest. "Electrical Conductivity of Single-Crystal Cr2O3". In: *Journal of Applied Physics* 35.8 (Aug. 1964), pp. 2413–2418. ISSN: 0021-8979. DOI: 10.1063/1.1702871.

[131] J. H. Park and K. Natesan. "Electronic transport in thermally grown Cr2O3". In: *Oxidation of Metals 1990 33:1* 33.1 (Feb. 1990), pp. 31–54. ISSN: 1573-4889. DOI: 10.1007/BF00665668.

[132] B. Gillot et al. "Electrical conductivity of copper and nickel manganites in relation with the simultaneous presence of Mn3+ and Mn4+ ions on octahedral sites of the spinel structure". In: *Solid State Ionics* 51.1-2 (Mar. 1992), pp. 7–9. ISSN: 0167-2738. DOI: 10.1016/0167-2738(92)90337-O.

[133] K. H. Tan, H. A. Rahman, and H. Taib. "Ba0.5Sr0.5Co0.8Fe0.2O3-δ-Sm0.2Ce0.8O1.9 carbonate perovskite coating on ferritic stainless steel interconnect for low temper-

ature solid oxide fuel cells". In: *Materials Chemistry and Physics* 254 (Nov. 2020), p. 123433. ISSN: 02540584. DOI: 10.1016/j.matchemphys.2020.123433.

[134] Manuel Bianco, Jan Pieter Ouweltjes, and Jan Van herle. "Degradation analysis of commercial interconnect materials for solid oxide fuel cells in stacks operated up to 18000 hours". In: *International Journal of Hydrogen Energy* 44.59 (Nov. 2019), pp. 31406–31422.

[135] A. Navrotsky and O. J. Kleppa. "The thermodynamics of cation distributions in simple spinels". In: *Journal of Inorganic and Nuclear Chemistry* 29.11 (Nov. 1967), pp. 2701–2714. ISSN: 0022-1902. DOI: 10.1016/0022-1902(67)80008-3.

[136] Claudia Goebel et al. "Does the conductivity of interconnect coatings matter for solid oxide fuel cell applications?" In: *Journal of Power Sources* 383 (Apr. 2018), pp. 110–114. ISSN: 03787753. DOI: 10.1016/j.jpowsour.2018.02.060.

[137] Zhenguo Yang et al. "Oxidation Behavior of Ferritic Stainless Steels under SOFC Interconnect Exposure Conditions". In: *Journal of The Electrochemical Society* 151.12 (Nov. 2004), B669. ISSN: 00134651. DOI: 10.1149/1.1810393/XML. URL: https://iopscience.iop.org/article/10.1149/1.1810393https://iopscience.iop.org/article/10.1149/1.1810393/metahttps://dx.doi.org/10.1149/1.1810393.

[138] Zhenguo Yang et al. "Anomalous corrosion behavior of stainless steels under SOFC interconnect exposure conditions". In: *Electrochemical and Solid-State Letters* 6.10 (Oct. 2003), B35. ISSN: 10990062. DOI: 10.1149/1.1603012/XML. URL: https://iopscience.iop.org/article/10.1149/1.1603012https://iopscience.iop.org/article/10.1149/1.1603012/meta.

[139] Paul Gannon and Roberta Amendola. "High-Temperature, Dual-Atmosphere Corrosion of Solid-Oxide Fuel Cell Interconnects". In: *JOM* 64.12 (2012), pp. 1470–1476. ISSN: 1543-1851. DOI: 10.1007/s11837-012-0473-3. URL: https://doi.org/10.1007/s11837-012-0473-3.

[140] Claudia Goebel et al. "The effect of pre-oxidation parameters on the corrosion behavior of AISI 441 in dual atmosphere". In: *International Journal of Hydrogen Energy* 43.31 (Aug. 2018), pp. 14665–14674. ISSN: 03603199. DOI: 10.1016/j.ijhydene.2018.05.165. URL: https://linkinghub.elsevier.com/retrieve/pii/S0360319918317695.

[141] Patrik Alnegren et al. "Temperature dependence of corrosion of ferritic stainless steel in dual atmosphere at 600–800 °C". In: *Journal of Power Sources* 392 (July 2018), pp. 129–138. ISSN: 0378-7753. DOI: 10.1016/J.JPOWSOUR.2018.04.088.

[142] M Tomas et al. "Novel coatings for protecting solid oxide fuel cell interconnects against the dual-atmosphere effect". In: *International Journal of Hydrogen Energy* (2023). ISSN: 0360-3199. DOI: https://doi.org/10.1016/j.ijhydene.2023.01.313. URL: https://www.sciencedirect.com/science/article/pii/S0360319923005736.

[143] Kerem O. Gunduz et al. "The effect of hydrogen on the breakdown of the protective oxide scale in solid oxide fuel cell interconnects". In: *Corrosion Science* 179 (Feb. 2021), p. 109112. ISSN: 0010-938X. DOI: 10.1016/J.CORSCI.2020.109112.

[144] Anders Werner Bredvei Skilbred and Reidar Haugsrud. "The effect of dual atmosphere conditions on the corrosion of Sandvik Sanergy HT". In: *International*

Journal of Hydrogen Energy 37.9 (May 2012), pp. 8095–8101. ISSN: 03603199. DOI: 10.1016/j.ijhydene.2011.10.096. URL: https://linkinghub.elsevier.com/retrieve/pii/S0360319911024700.

[145] J. Rufner et al. "Oxidation behavior of stainless steel 430 and 441 at 800 °C in single (air/air) and dual atmosphere (air/hydrogen) exposures". In: *International Journal of Hydrogen Energy* 33.4 (Feb. 2008), pp. 1392–1398. ISSN: 0360-3199. DOI: 10.1016/J.IJHYDENE.2007.12.067.

[146] Y. Zhao and J. W. Fergus. "Oxidation of Alloys 430 and 441 in SOFC Dual Atmospheres: Effects of Flow Rate and Humidity". In: *Journal of The Electrochemical Society* 159.3 (Dec. 2012), pp. C109–C113. ISSN: 0013-4651. DOI: 10.1149/2.013203JES/XML. URL: https://iopscience.iop.org/article/10.1149/2.013203jeshttps://iopscience.iop.org/article/10.1149/2.013203jes/meta.

[147] Hideto Kurokawa et al. "Hydrogen Permeation Through Fe-16Cr Alloy Interconnect in Atmosphere Simulating SOFC at 1073 K". In: *Journal of The Electrochemical Society* 151.8 (July 2004), A1264. ISSN: 00134651. DOI: 10.1149/1.1767349/XML. URL: https://iopscience.iop.org/article/10.1149/1.1767349https://iopscience.iop.org/article/10.1149/1.1767349/meta.

[148] Gordon R. Holcomb et al. "Dual-environment effects on the oxidation of metallic interconnects". In: *Journal of Materials Engineering and Performance 2006 15:4* 15.4 (Aug. 2006), pp. 404–409. ISSN: 1544-1024. DOI: 10.1361/105994906X117198. URL: https://link.springer.com/article/10.1361/105994906X117198.

[149] J Andreas Schuler et al. "Cr-poisoning in (La,Sr)(Co,Fe)O3 cathodes after 10,000h SOFC stack testing". In: *Journal of Power Sources* 211 (2012), pp. 177–183. ISSN: 0378-7753. DOI: https://doi.org/10.1016/j.jpowsour.2012.03.045.

[150] J. Froitzheim et al. "Investigation of Chromium Volatilization from FeCr Interconnects by a Denuder Technique". In: *Journal of The Electrochemical Society* 157.9 (2010), B1295. ISSN: 00134651. DOI: 10.1149/1.3462987.

[151] J. Michael Hollas. *Modern Spectroscopy*. 4th ed. 2013, pp. 1–482. ISBN: 978-1-118-68160-2.

[152] Marie-Christine Fournier-Salaün and Philippe Salaün. "Quantitative determination of hexavalent chromium in aqueous solutions by UV-Vis spectrophotometer". In: *Central European Journal of Chemistry 2007 5:4* 5.4 (Dec. 2007), pp. 1084–1093. ISSN: 1644-3624. DOI: 10.2478/S11532-007-0038-4.

[153] Weilie Zhou et al. "Fundamentals of Scanning Electron Microscopy (SEM)". In: *Scanning Microscopy for Nanotechnology: Techniques and Applications*. Ed. by Weilie Zhou and Zhong Lin Wang. Springer, New York, NY, 2006, pp. 1–40. ISBN: 978-0-387-39620-0. DOI: 10.1007/978-0-387-39620-0{_}1.

[154] R. F. Egerton. *Physical principles of electron microscopy: An introduction to TEM, SEM, and AEM, second edition*. 2nd ed. Springer International Publishing, Jan. 2016, pp. 1–196. ISBN: 978-3-319-39877-8. DOI: 10.1007/978-3-319-39877-8.

[155] Jan Gustav Grolig. "Coated Ferritic Stainless Steels as Interconnects in Solid Oxide Fuel Cells - Material Development and Electrical Properties". PhD thesis. Chalmers University of Technology, Jan. 2015. ISBN: 978-91-7597-234-3. URL: https://research.chalmers.se/en/publication/220089.

[156] Harri Ali-Löytty et al. “The role of (FeCrSi)2(MoNb)-type Laves phase on the formation of Mn-rich protective oxide scale on ferritic stainless steel”. In: *Corrosion Science* 132 (2018), pp. 214–222. ISSN: 0010-938X. DOI: https://doi.org/10.1016/j.corsci.2017.12.026. URL: https://www.sciencedirect.com/science/article/pii/S0010938X17305346.

[157] Teruhisa Horita et al. “Evaluation of Laves-phase forming Fe–Cr alloy for SOFC interconnects in reducing atmosphere”. In: *Journal of Power Sources* 176.1 (Jan. 2008), pp. 54–61. ISSN: 0378-7753. DOI: 10.1016/J.JPOWSOUR.2007.10.041.

[158] Zhenguo Yang et al. “Investigation of iron-chromium-niobium-titanium ferritic stainless steel for solid oxide fuel cell interconnect applications”. In: *Journal of Power Sources* 183.2 (Sept. 2008), pp. 660–667. ISSN: 03787753. DOI: 10.1016/j.jpowsour.2008.05.037.

[159] Itai Panas et al. “Chromic acid evaporation upon exposure of Cr2O3(s) to H2O(g) and O2(g) – mechanism from first principles”. In: *Chemical Physics Letters* 383.5 (2004), pp. 549–554. ISSN: 0009-2614. DOI: https://doi.org/10.1016/j.cplett.2003.11.079. URL: https://www.sciencedirect.com/science/article/pii/S0009261403020670.

[160] Jun Shu et al. “The effects of molybdenum addition on high temperature oxidation behavior at 1,000 °c of type 444 ferritic stainless steel”. In: *Oxidation of Metals* 78.3-4 (Oct. 2012), pp. 253–267. ISSN: 0030770X. DOI: 10.1007/s11085-012-9304-8.

[161] Claudia Goebel et al. “Self-healing properties of Ce/Co-coated stainless steel under simulated intermediate temperature solid oxide fuel cell conditions”. In: *Surface and Coatings Technology* 428 (Dec. 2021), p. 127894. ISSN: 0257-8972. DOI: 10.1016/J.SURFCOAT.2021.127894.

[162] Anna Magrasó et al. “Reduced long term electrical resistance in Ce/Co-coated ferritic stainless steel for solid oxide fuel cell metallic interconnects”. In: *International Journal of Hydrogen Energy* 40.27 (July 2015), pp. 8579–8585. ISSN: 03603199. DOI: 10.1016/j.ijhydene.2015.04.147. URL: https://linkinghub.elsevier.com/retrieve/pii/S036031991501085X.

[163] Hannes Falk-Windisch et al. “Co- and Ce/Co-coated ferritic stainless steel as interconnect material for Intermediate Temperature Solid Oxide Fuel Cells”. In: *Journal of Power Sources* 343 (2017), pp. 1–10. ISSN: 03787753. DOI: 10.1016/j.jpowsour.2017.01.045.

[164] Matthieu Tomas et al. “Cu-Based Coatings for IT-SOFC Applications”. In: *ECS Transactions* 91.1 (July 2019), pp. 2291–2298. ISSN: 1938-6737. DOI: 10.1149/09101.2291ecst.

[165] W. David Kingery, H. K. Bowen, and Donald R. Uhlmann. *Introduction to Ceramics, 2nd Edition*. 1976, p. 1056. ISBN: 978-0-471-47860-7.

[166] Mirosław Stygar et al. “Oxidation properties of ferritic stainless steel in dual Ar–H2–H2O/air atmosphere exposure with regard to SOFC interconnect application”. In: *Solid State Ionics* 262 (Sept. 2014), pp. 449–453. ISSN: 0167-2738. DOI: 10.1016/J.SSI.2014.03.029.

[167] M.J. Reddy et al. “11–23% Cr steels for solid oxide fuel cell interconnect applications at 800 °C – How the coating determines oxidation kinetics”. In: *International Journal of Hydrogen Energy* 48.34 (Apr. 2023), pp. 12893–12904. ISSN: 03603199. DOI:

10.1016/j.ijhydene.2022.11.326. URL: https://www.sciencedirect.com/science/article/pii/S0360319922056646https://linkinghub.elsevier.com/retrieve/pii/S0360319922056646.

[168] Belma Talic et al. "Comparison of MnCo2O4 coated Crofer 22 H, 441, 430 as interconnects for intermediate-temperature solid oxide fuel cell stacks". In: *Journal of Alloys and Compounds* 821 (Apr. 2020), p. 153229. ISSN: 09258388. DOI: 10.1016/j.jallcom.2019.153229.

[169] M. Tomas et al. "Efficiencies of cobalt- and copper-based coatings applied by different deposition processes for applications in intermediate-temperature solid oxide fuel cells". In: *International Journal of Hydrogen Energy* 47.76 (Sept. 2022), pp. 32628–32640. ISSN: 0360-3199. DOI: 10.1016/J.IJHYDENE.2022.07.168.

[170] Qingqing Zhao et al. "Comparison of electroplating and sputtering Ni for Ni/NiFe2 dual layer coating on ferritic stainless steel interconnect". In: *Corrosion Science* 192 (Nov. 2021), p. 109837. URL: https://linkinghub.elsevier.com/retrieve/pii/S0010938X2100603X.

[171] Belma Talic et al. "Effect of coating density on oxidation resistance and Cr vaporization from solid oxide fuel cell interconnects". In: *Journal of Power Sources* 354 (2017), pp. 57–67. ISSN: 03787753. DOI: 10.1016/j.jpowsour.2017.04.023.

[172] Bartosz Kamecki et al. "Deposition and Electrical and Structural Properties of La0.6Sr0.4CoO3 Thin Films for Application in High-Temperature Electrochemical Cells". In: *Journal of Electronic Materials 2019 48:9* 48.9 (June 2019), pp. 5428–5441. ISSN: 1543-186X. DOI: 10.1007/S11664-019-07372-7. URL: https://link.springer.com/article/10.1007/s11664-019-07372-7.

[173] B. Kamecki et al. "Low temperature deposition of dense MnCo2O4 protective coatings for steel interconnects of solid oxide cells". In: *Journal of the European Ceramic Society* 38.13 (Oct. 2018), pp. 4576–4579. ISSN: 0955-2219. DOI: 10.1016/J.JEURCERAMSOC.2018.05.042.

[174] Jung Pyung Choi and Jeffry W Stevenson. "Electrically Conductive and Protective Coating for Planar SOFC Stacks". In: *ECS Transactions* 78.1 (May 2017), pp. 1633–1640. ISSN: 1938-6737. DOI: 10.1149/07801.1633ECST/XML. URL: https://iopscience.iop.org/article/10.1149/07801.1633ecsthttps://iopscience.iop.org/article/10.1149/07801.1633ecst/meta.

[175] Nikolas Grünwald et al. "Microstructure and phase evolution of atmospheric plasma sprayed Mn-Co-Fe oxide protection layers for solid oxide fuel cells". In: *Journal of the European Ceramic Society* 39.2-3 (Feb. 2019), pp. 449–460.

[176] Nikolas Grünwald et al. "Self-healing atmospheric plasma sprayed Mn1.0Co1.9Fe0.1O4 protective interconnector coatings for solid oxide fuel cells". In: *Journal of Power Sources* 363 (Sept. 2017), pp. 185–192. ISSN: 0378-7753. DOI: 10.1016/J.JPOWSOUR.2017.07.072.

[177] Nikolas Grünwald et al. "In situ investigation of atmospheric plasma-sprayed Mn–Co–Fe–O by synchrotron X-ray nano-tomography". In: *Journal of Materials Science* 55.27 (Sept. 2020), pp. 12725–12736. ISSN: 15734803. DOI: 10.1007/S10853-020-04916-9/FIGURES/5. URL: https://link.springer.com/article/10.1007/s10853-020-04916-9.

[178] Neal J. Magdefrau et al. “Formation of spinel reaction layers in manganese cobaltite-coated Crofer22 APU for solid oxide fuel cell interconnects”. In: *Journal of Power Sources* 227 (2013), pp. 318–326. ISSN: 03787753. DOI: 10.1016/j.jpowsour.2012.07.091.

[179] E. Zanchi et al. “Iron doped manganese cobaltite spinel coatings produced by electrophoretic co-deposition on interconnects for solid oxide cells: Microstructural and electrical characterization”. In: *Journal of Power Sources* 455 (Apr. 2020). ISSN: 03787753. DOI: 10.1016/j.jpowsour.2020.227910.

[180] T M Devine. “Kinetics of sensitization and de-sensitization of duplex 308 stainless steel”. In: *Acta Metallurgica* 36.6 (1988), pp. 1491–1501. ISSN: 0001-6160. DOI: https://doi.org/10.1016/0001-6160(88)90216-7.

[181] Ali Aghajani. *JmatPro phase analysis - personal communication*. 2021.

[182] R Duan et al. “Predicting Oxidation-Limited Lifetime of Thin-Walled Components of NiCrW Alloy 230”. In: *Oxidation of Metals* 87.1 (2017), pp. 11–38. ISSN: 1573-4889. DOI: 10.1007/s11085-016-9653-9. URL: https://doi.org/10.1007/s11085-016-9653-9.

[183] J P T Vossen et al. “Limits of the oxidation resistance of several heat-resistant steels under isothermal and cyclic oxidation as well as under creep in air at 650°C”. In: *Materials at High Temperatures* 14.4 (Jan. 1997), pp. 387–401. ISSN: 0960-3409. DOI: 10.1080/09603409.1997.11689565. URL: https://doi.org/10.1080/09603409.1997.11689565.

[184] Louis Sadowski Cavichiolo et al. “Effects of interdiffusion in nickel coated AISI 441 steel”. In: *Materials Characterization* 194 (2022), p. 112413. ISSN: 1044-5803. DOI: https://doi.org/10.1016/j.matchar.2022.112413. URL: https://www.sciencedirect.com/science/article/pii/S1044580322006957.

[185] K. A. Nielsen et al. “Testing of Ni-Plated Ferritic Steel Interconnect in SOFC Stacks”. In: *Fuel Cells* 6.2 (Apr. 2006), pp. 100–106. ISSN: 1615-6854. DOI: 10.1002/FUCE.200500114. URL: https://onlinelibrary.wiley.com/doi/full/10.1002/fuce.200500114https://onlinelibrary.wiley.com/doi/abs/10.1002/fuce.200500114https://onlinelibrary.wiley.com/doi/10.1002/fuce.200500114.

[186] Tien-Fu Chen et al. “Volume and Grain Boundary Diffusion of Chromium in Ni-Base Ni-Cr-Fe Alloys”. In: *MATERIALS TRANSACTIONS* 44.1 (2003), pp. 40–46. DOI: 10.2320/matertrans.44.40.

[187] G. Calvarin, R. Molins, and A. M. Huntz. “Oxidation Mechanism of Ni-20Cr Foils and Its Relation to the Oxide-Scale Microstructure”. In: *Oxidation of Metals* 53.1-2 (2000), pp. 25–48. ISSN: 0030770X. DOI: 10.1023/A:1004578513020.

[188] Xu Wang and Jerzy A Szpunar. “Effects of grain sizes on the oxidation behavior of Ni-based alloy 230 and N”. In: *Journal of Alloys and Compounds* 752 (2018), pp. 40–52. ISSN: 0925-8388. DOI: https://doi.org/10.1016/j.jallcom.2018.04.173.

List of Figures